UNIVERSIDADE DE LISBOA

Faculdade de Medicina

Force transmission and endothelial cell rearrangements during vascular remodeling

Joana Cristina Reino Carvalho

Orientador:
Doutor Cláudio Areias Franco

Tese especialmente elaborada para obtenção do grau de Doutor em Ciências Biomédicas, especialidade de Biologia Celular e Molecular

2019

UNIVERSIDADE DE LISBOA

Faculdade de Medicina

Force transmission and endothelial cell rearrangements during vascular remodeling

Joana Cristina Reino Carvalho

Orientador: Doutor Cláudio Areias Franco

Tese especialmente elaborada para obtenção do grau de Doutor em Ciências Biomédicas, especialidade de Biologia Celular e Molecular

Júri:
Presidente: Doutor João Eurico Cortez Cabral da Fonseca, Professor Catedrático e Vice Presidente do Conselho Científico da Faculdade de Medicina da Universidade de Lisboa
Vogais:

- Doutor Stephan Huvenneers, Investigador Principal da Academic Medical Center, University of Amsterdam;
- Doutora Ana Costa Xavier de Carvalho, Investigadora Principal do Instituto de Biologia Molecular e Celular da Universidade do Porto;
- Doutor Cláudio Areias Franco, Investigador Principal do Instituto de Medicina Molecular – João Lobo Antunes, unidade de investigação associada à Faculdade de Medicina da Universidade de Lisboa (Orientador);
- Doutora Maria Leonor Tavares Saúde, Professora Associada Convidada da Faculdade de Medicina da Universidade de Lisboa;
- Doutor Edgar Rodrigues Almeida Gomes, Professor Associado Convidado da Faculdade de Medicina da Universidade de Lisboa;
- Doutor Domingos Manuel Pinto Henrique, Investigador Auxiliar da Faculdade de Medicina da Universidade de Lisboa.

Instituições financiadoras: Fundação da Ciência e Tecnologia SFRH/BD/52224/2013

2019

A impressão desta tese foi aprovada pelo Conselho Científico da Faculdade de Medicina de Lisboa em reunião de 20 de Março de 2018.

As opiniões expressas nesta publicação são da exclusiva responsabilidade do seu autor.

Acknowledgements

First I would like to thank to all the people in the lab, especially Cláudio, my supervisor, for his guidance and support throughput my PhD, and of course to all my lab mates, whom I closely work with during these four years. I would like to leave a special thanks to Catarina Fonseca and to Isabela Fortunato for their precious help in some of these experiments and also for their amazing companionship.

To Filomena Carvalho, who accepted to collaborate with us in this project and was always available for discussion. To Anna Pezzarossa, who was the driving force behind all the mathematical and image analysis and constantly managed to come up with helpful suggestions and solutions whenever I had a problem. To Francisca Vasconcelos, who contributed with her expertise in Molecular Biology and also for improving and facilitating organization in the lab, making work life more enjoyable to everyone.

To Domingos Henrique, Edgar Gomes and Florence Janody, who gladly accepted to become members of my PhD thesis committee for their unbiased suggestions and healthy discussions throughout the project.

To everyone involved in the LisbonBioMed PhD Program, especially Filipa Nunes from the Career Development unit who was always ready to help whenever I had a doubt about administrative procedures. To all the facilities at iMM, especially the Bioimaging facility for all the support provided during this project.

And finally a special thanks to all my family and friends for their unconditional support throughout this whole journey. Without you, I wouldn't have made it this far. I love you all very much!

This is for all of you!

Table of Contents

List of Figures

List of Tables

List of abbreviations

Acronym	Expanded text
AFM	Atomic force microscopy
APC	Adenomatous polyposis coli
BSA	Bovine serum albumin
CAMKII	Ca^{2+}/Calmodulin-dependent protein kinase II
CDC42	Cell division control protein 42
CIL	Contact inhibition of locomotion
CXCL12	C-X-C motif chemokine 12
DAPI	4',6-diamidino-2-phenylindole
DLL	Delta-like ligand
DMEM	Dulbecco's Modified Eagle Medium
DTT	Dithiothreitol
EC/ECs	Endothelial cell(s)
ECM	Extracellular matrix
EDTA	Ethylenediaminetetraacetic acid
F-actin	Filamentous actin
FBS	Fetal bovine serum
FRET	Förster resonance energy transfer
FZD	Frizzled
GAPs	GTPase-activating proteins
GDP	Guanosine diphosphate
GEFs	Guanine-nucleotide exchange factors
GTP	Guanosine triphosphate
HBSS	Hank's Balanced Salt Solution
HUVEC/HUVECs	Human umbilical vein endothelial cell(s)
JAG	Jagged
JNK	JUN-N-terminal kinase
KD	Knockdown
LRP	Lipoprotein receptor-related protein
MLC	Myosin light chain
NFAT	Nuclear factor of activated T cells
NRP1	Neuropilin-1
PBS	Phosphate-buffered saline
PCP	Planar cell polarity
PFA	Paraformaldehyde
PKC	Protein kinase C
RAC1	Ras-related C3 botulinum toxin substrate 1
RHOA	Ras homolog gene family, member A
RIPA	Radioimmunoprecipitation assay
RNA	Ribonucleic acid
ROCK	Rho-associated protein kinase

ROR	Retinoid-related orphan receptor
RT	Room temperature
RT-qPCR	Real-time quantitative polymerase chain reaction
RYK	Receptor-like tyrosine kinase
SDS-PAGE	Sodium dodecyl sulphate-polyacrylamide gel electrophoresis
siRNA	Small-interference RNA
TBS	Tris-buffered saline
VEGF	Vascular endothelial growth factor
VEGFR	Vascular endothelial growth factor receptor
WNT	Wingless-related integration site

Summary

Collective cell migration is a widespread biologic process that is crucial not only during homeostasis, but also in the context of disease. Mechanistically, it is based on the establishment of a front-rear polarity axis, and on the maintenance and dynamic regulation of cell-cell adhesions, which are crucial for traction force generation and oriented cell movements. Sprouting angiogenesis, a biologic process that enables the expansion of the vascular network, relies on the collective migration of specialized strands of endothelial cells composed by tip and stalk cells. Wnt5a, a non-canonical Wnt ligand, has been described as a pro-angiogenic factor that promotes cell proliferation, migration and network formation. More recently, it was shown to be crucial during sprouting angiogenesis. Indeed, genetic deletion of Wnt5a in endothelial cells reduces the expansion of the vascular plexus in the mouse retina. However, it is still unclear how Wnt5a exerts these functions in the endothelium and which specific molecular components could be involved. Therefore, to investigate these questions, we used the *in vitro* wound-healing assay to study endothelial collective cell behavior. With this system we uncovered that loss of Wnt5a leads to randomized follower cell polarity and migration, dramatically impairing coordination of collective cell behavior. Moreover, we also showed that cells lacking Wnt5a had a significant decrease in cell-cell force transmission and displayed a specific downregulation of vinculin co-localization to VE-cadherin at cell junctions. Then, we showed that randomized cell polarity in Wnt5a-depleted cells could be rescued by forcing the association of vinculin to cell junctions by overexpressing the αCat-Vinc fusion protein, or a constitutive active form of vinculin (Vinc-T12). Mechanistically, we identified ROR2/Cdc42 as the most relevant transducers in the signaling cascade triggered by Wnt5a. Altogether, we propose a model where Wnt5a, via ROR2/Cdc42, promotes vinculin and Arp2/3 association to adherens junctions, enhancing actin polymerization and junction stabilization. These strengthened adherens junctions would then act as a platform to enable stable force transmission between adjacent cells and coordination of endothelial cell behaviors during collective migration. Given its implications in evolutionarily conserved morphogenetic processes that require cell-cell mechanocoupling, we believe the mechanotransduction function of Wnt5a we

described here may be applicable to other tissues and contexts. In the context of vascular biology, our findings may be relevant to understand the mechanical and molecular mechanisms involved in the collective migration of vessel sprouts driven by tip cells *in vivo*. Moreover, as Wnt5a has been described as a potential key regulator of cancer, our results might be relevant to understand disease onset and progression and even contribute to the development of potential therapies.

Keywords:

Angiogenesis; Collective cell migration; Adherens junctions; Mechanotransduction; Non-canonical Wnt signaling

Resumo

A migração colectiva de células é um processo biológico que é crucial não só em condições de homeostasia (por exemplo durante a morfogénese de tecidos), mas também no contexto patológico (por exemplo durante a invasão cancerígena e formação de metástases). Em termos mecanísticos é baseada na formação de um eixo de polaridade anterior-posterior, que por sua vez é gerado através de uma distribuição polarizada de diversos componentes de várias vias de sinalização envolvidas na regulação de rearranjos do citoesqueleto e reciclagem de proteínas. Além de rearranjos do citoesqueleto, a manutenção e regulação dinâmica das junções celulares é essencial para evitar migração celular disruptiva e promover o movimento coordenado do agregado celular. Nesse sentido, a adesão célula-célula é a fundação que permite o acoplamento mecânico entre células líder (localizadas à frente no grupo e responsáveis por guiarem a migração do agregado) e células seguidoras (localizadas atrás no grupo e dependentes das anteriores para polarizarem e migrarem de forma orientada), o que por sua vez é crucial para a geração de forças de tracção e para o movimento direccional das células.

A formação de uma rede de vasos sanguíneos é maioritariamente mediada através de um fenómeno biológico denominado angiogénese, que é um programa multifacetado que inclui uma série de processos que promovem a invasão de vasos sanguíneos em tecidos não vascularizados, levando assim à expansão da rede vascular pré-existente. Durante a fase inicial de angiogénese por brotação, o plexo vascular imaturo expande através da migração colectiva de células endoteliais especializadas inseridas em brotos compostos por células de ponta (ou líderes) e células de base (seguidoras). Apesar das vias de sinalização envolvidas na selecção de células de ponta e de base terem sido estudadas extensivamente no passado, os mecanismos moleculares que estão envolvidos no processo de migração colectiva subjacente a este processo ainda não estão bem descritos.

A sinalização não-canónica do Wnt desempenha um papel central na regulação da polaridade de tecidos, rearranjos do citoesqueleto celular, determinação do destino celular e migração, e como tal, é crucial para diversos processos envolvidos na migração colectiva de células. Contudo, a sua função no contexto de angiogénese é muito menos clara e só recentemente é que começou a ser investigada. O Wnt5a, um

ligando da via não-canónica do Wnt, foi descrito como sendo um factor pro-angiogénico que promove a proliferação de células endoteliais, migração e formação da rede vascular. Mais recentemente foi mostrado ser essencial durante a angiogénese por brotação para promover a migração direccional dos brotos vasculares e a subsequente expansão do plexo vascular da retina de ratinhos com seis dias pós-natais. Contudo, ainda não é claro como é que a sinalização não-canónica do Wnt exerce estas funções, nem quais são os componentes moleculares que estão envolvidos na transdução de sinal a jusante da sinalização inicial mediada pelo acoplamento do ligando ao receptor.

Uma vez que a sinalização não-canónica do Wnt foi associada à regulação da polaridade de tecidos e já foi demonstrado que retinas de ratinhos com deleção de Wnt5a em células endoteliais apresentam expansão radial reduzida, perguntámo-nos se a ausência de Wnt5a poderia afectar a capacidade das células endoteliais de quebrar a simetria e polarizar correctamente, e consequentemente, ter um impacto negativo na sua capacidade de migração direccional. Assim, para clarificar esta questão, propusemo-nos investigar neste estudo os mecanismos moleculares específicos através dos quais a sinalização mediada pelo Wnt5a exerce estas funções em células endoteliais utilizando um ensaio *in vitro* mais simples, fácil de manipular e bem estabelecido – o ensaio de cicatrização. Além disso, desenvolvemos também um método quantitativo altamente reprodutível que nos permitiu quantificar a polaridade colectiva de células neste ensaio, o índice de polaridade. Através deste sistema descobrimos que a perda de Wnt5a tem como consequência a randomização da polaridade e migração das células seguidoras, afectando dramaticamente a coordenação do comportamento colectivo das células endoteliais. Experiências de microscopia de força atómica e de transferência de energia por ressonância de Förster permitiram-nos concluir que a ausência de Wnt5a provoca uma diminuição significativa na transmissão de forças célula-célula que é dependente das interacções homofílicas de VE-caderina. Além disso, também demonstrámos que células silenciadas para Wnt5a apresentam uma diminuição na co-localização de vinculina e VE-caderina nas junções aderentes causada por uma instabilidade na associação a longo-prazo da vinculina ao complexo caderina-catenina. De seguida, provámos que a randomização de polaridade de células silenciadas para Wnt5a poderia ser restaurada ao forçar a associação permanente de vinculina às junções celulares através da sobre-

expressão de uma proteína de fusão α-catenina-vinculina, ou então da sobre-expressão de uma versão constitutivamente activa de vinculina (vinculina-T12). Curiosamente, a mesma proteína de fusão α-catenina-vinculina com uma mutação pontual no local de ligação do complexo Arp2/3 à vinculina foi incapaz de restaurar a polaridade em células silenciadas para Wnt5a. Assim, uma vez que a vinculina por si só é suficiente para restaurar a polaridade randomizada observada na ausência de Wnt5a, concluímos primeiro que a redução dos níveis de vinculina associada às junções aderentes em células silenciadas para Wnt5a parecem induzir instabilidade/ruptura das junções, afectando assim a transmissão de forças e a coordenação celular durante a migração colectiva. E segundo, não só a vinculina, mas também o complexo Arp2/3 necessita de estar associado às junções aderentes para que as células endoteliais apresentem coordenação colectiva.

Em termos mecanísticos, demonstrámos que o ROR2 foi o único receptor da via Wnt cujo silenciamento reproduziu na totalidade o fenótipo de randomização de polaridade celular e de diminuição de vinculina nas junções aderentes presente na ausência de Wnt5a. Além disso, também mostrámos que o Cdc42 é essencial para a polaridade de células endoteliais, já que o silenciamento ou inibição desta Rho GTPase induz randomização da polaridade celular. De seguida verificámos também que na ausência de Cdc42, os níveis de vinculina nas junções celulares diminuem significativamente, de forma idêntica àquilo que já tinha sido descrito em células silenciadas para Wnt5a e ROR2. Com base nos resultados apresentados, propomos um modelo onde a ligação do Wnt5a ao receptor ROR2 desencadeia a activação do Cdc42. Por sua vez, o Wnt5a através da via de sinalização ROR2/Cdc42 leva à associação da vinculina e do complexo Arp2/3 às junções aderentes, promovendo a polimerização local de actina e estabilizando o complexo caderina-catenina. Estas junções celulares fortalecidas irão depois actuar como a plataforma que possibilita a geração e transmissão de forças de tensão entre células adjacentes, promovendo assim a coordenação celular durante a migração colectiva. Na ausência de Wnt5a, as junções aderentes com níveis reduzidos de vinculina e Arp2/3 tornam-se instáveis, o que faz com que a transmissão de forças das células líder para as células seguidoras seja menos eficiente, levando assim à randomização da polaridade das células seguidoras e à migração colectiva descoordenada. Uma vez que a via de sinalização do Wnt é evolutivamente conservada e está implicada em processos morfogenéticos que requerem o acoplamento mecânico

entre células vizinhas, acreditamos que a função mecanotransdutora do Wnt5a que descrevemos neste estudo possa ser aplicável a outros tecidos e a outros contextos. No contexto da biologia vascular, os nossos resultados poderão contribuir para a compreensão dos mecanismos moleculares e mecânicos envolvidos na migração colectiva de células endoteliais durante a angiogénese por brotação na retina. Além disso, diversos estudos têm apontado o Wnt5a como um potencial regulador do cancro, actuando tanto como um supressor tumoral e como um factor pro-oncogénico, dependendo do tipo de tumor. Assim, seria interessante investigar se os mecanismos descritos neste estudo poderiam ser relevantes para a compreensão do aparecimento e progressão da doença, bem como para o eventual desenvolvimento de potenciais medidas terapêuticas.

Palavras-chave:

Angiogénese; Migração colectiva de células; Junções aderentes; Mecanotransdução; Sinalização não-canónica do Wnt

Chapter I. Introduction

I.1. The biology of collective cell migration

Cell migration is a widespread biologic process that is crucial not only for homeostasis (*e.g.* tissue morphogenesis), but also in the context of disease (*e.g.* wound healing, cancer invasion and metastasis) (Friedl and Weigelin, 2008; Ridley *et al.*, 2003). The migration of single cells has been thoroughly studied over the past years (Bear and Haugh, 2014; Petrie *et al.*, 2009; Ridley *et al.*, 2003), leading to the discovery of the major molecular mechanisms controlling cell movement. Experimental evidences have pointed out that in a native state single cells polarize randomly and are only able to migrate across short distances due to their lack of migration persistence. However, in situations where cells are required to migrate persistently over long distances (*e.g.* leukocytes migrating towards an inflammation site), a symmetry breaking event has to

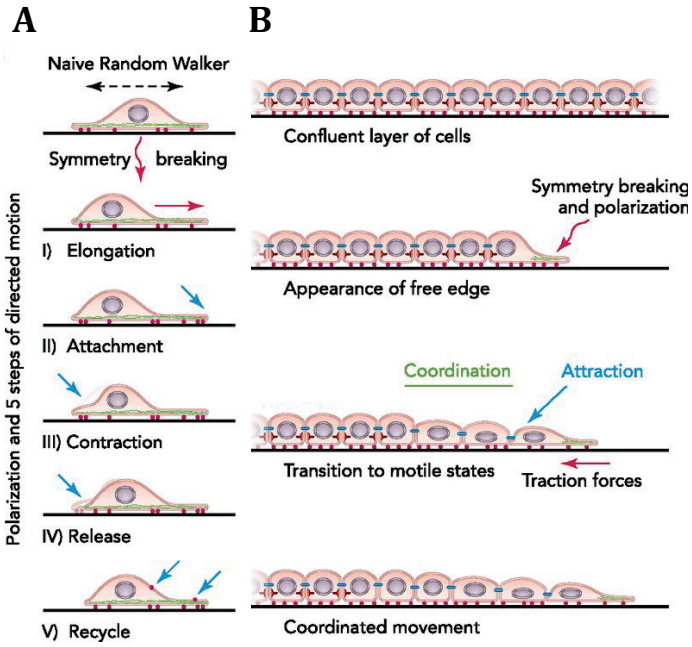

Figure 1. Single and collective cell migration. (A) Single cell migration – Symmetry-breaking events lead to cell polarization and to leading edge elongation **(I)** through the formation of actin-rich protrusions (lamellipodia, filopodia). The newly-formed cell protrusions attach to the substrate **(II)**, while acto-myosin contraction induces the retraction of the cell rear **(III)**. The cell rear is then released from the substratum **(IV)**, enabling movement towards the front. This cycle of attachment – contraction – release repeats itself as soon as the migration machinery is recycled **(V)**. (**B) Collective cell migration** – When cells are on a confluent monolayer, they are symmetrically inhibited, resulting in little migration. Availability of free space to migrate breaks the symmetry and polarizes the cells at the edge towards the free space. This overcomes the inhibitory signals and promotes cell motility. Motile cells at the front exert attractive forces on their neighbors, which, in turn, coordinate their movement.

Adapted from Vedula *et al.*, 2013

occur to prompt cells to become biased towards a particular direction to migrate. Such symmetry breaking events can be caused by the presence of rigidity (durotaxis) or chemical gradients from soluble (chemotaxis) and substrate-bound (haptotaxis) ligands (Duchek and Rorth, 2001; Duchek *et al.*, 2001; Huang *et al.*, 2005) or even from physical restraints present in the cell microenvironment that prevent cells from moving in all directions (le Digabel et al., 2010; Thery, 2010). Immediately after the initial symmetry breaking event, cells produce and emit actin-rich protrusions (filopodia, lamellipodia), elongating the leading edge, which results in the establishment of a typical front-rear polarized morphology. The next steps comprise successive cycles of attachment – contraction – release. During these cycles the newly-formed cell protrusions at the leading edge attach to the substrate, while acto-myosin contraction at the back of the cell induce the retraction of the cell rear and its progression towards the leading edge. Adhesive proteins anchoring the cell rear to the substratum are subsequently disassembled, enabling movement towards the front (Figure 1A) (Vedula *et al.*, 2013).

More recently, collective cell migration has been gaining increasing relevance, since in various biological processes cells do not migrate individually, but rather collectively, as clusters, chains or sheets (Vedula *et al.*, 2013). Besides driving the formation of complex tissues and organs during embryogenesis (Weijer, 2009), collective migration also occurs in the adult during wound healing, tissue renewal and angiogenesis and has been associated with tumor spreading (Friedl and Gilmour, 2009).

This alternative migration mode, as the name suggests, differs mainly from single cell migration in the sense that cells remain attached to each other as they migrate. For this to happen, several conditions must be met: 1) Cells must be subjected to a common symmetry breaking event and polarize simultaneously towards the same direction; 2) Cells within the cluster must migrate in the same direction at a similar speed to avoid disruptive movement; 3) Cells must be able to communicate with each other and coordinate their response with the microenvironment; 4) And finally, cells must maintain their cell-cell contacts throughout the process, not only to ensure the integrity of the group, but also to enable biochemical and mechanical coupling between adjacent cells (Figure 1B) (Mayor and Etienne-Manneville, 2016). One of the main advantages of cells migrating collectively, as opposed to individually, is that cells within these cohesive groups migrate much more efficiently than they would if they

were isolated. Although cells within groups may have a lower instant velocity, their migration is more persistent, which enables the cell aggregate to cover longer distances more efficiently when compared to single cells (Mayor and Etienne-Manneville, 2016).

I.2. The concept of leader and follower cells

Even though the same polarization events taking place during single cell migration occur within each individual cell forming the cluster, the relative position each occupies within the group adds a new layer of complexity that needs to be taken into account. In this sense, cells have been categorized according to their relative spatial position inside the cell aggregate: 1) The leader or pioneer cells, which are at the migration front of the group and are responsible for sensing the microenvironment and driving the overall migration behavior of the cell aggregate; 2) The follower cells, which are behind the leader cells and rely on the cues provided by the leaders to polarize and migrate in a coordinated manner, while maintaining the cohesion of the group (Figure 2) (Mayor and Etienne-Manneville, 2016).

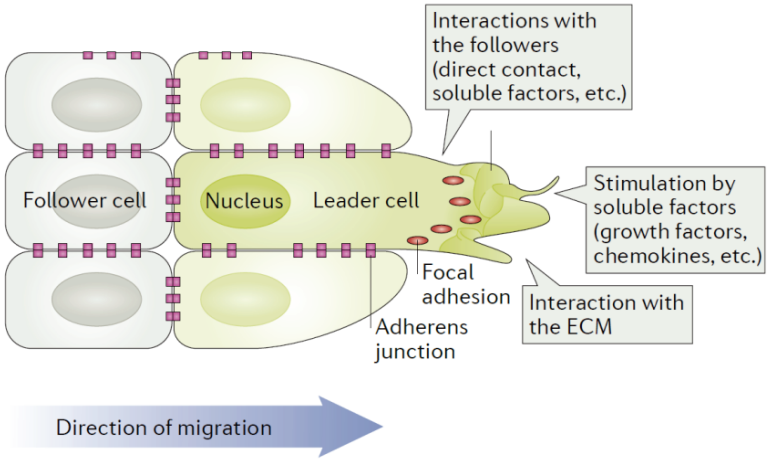

Figure 2. Leader and follower cells. In a cluster, the leader cells (green) at the front of the group are subjected to polarized environmental cues and are responsible for controlling the direction and speed of migration of the cell aggregate. On the other hand, follower cells (gray) at the back of the group are responsible for maintaining the cohesion of the aggregate via adherens junctions and rely on the information provided by the leaders to polarize correctly.

Adapted from Mayor and Etienne-Manneville, 2016

Generally, leaders and followers can be found at the front and at the back of the cell cluster, respectively, however they are also able to adopt distinct sub-organizations, depending on the context and, in particular, on the geometry of the migrating group. For instance, the number of leader cells necessary to drive the migration of the group can vary enormously depending on the size and shape of the cell aggregate. On aggregates without a defined rear (*e.g.* fibroblast wound healing), there is a first row of leaders that can span up to hundreds of cells driving the movement of the cell monolayer. On the other hand, only one or two leader cells, also called tip cells, are sufficient to guide the collective migration of strands of cells (*e.g.* endothelial cells during sprouting angiogenesis), or the small cluster of *D. melanogaster* border cells (Figure 3) (Caussinus *et al*., 2008).

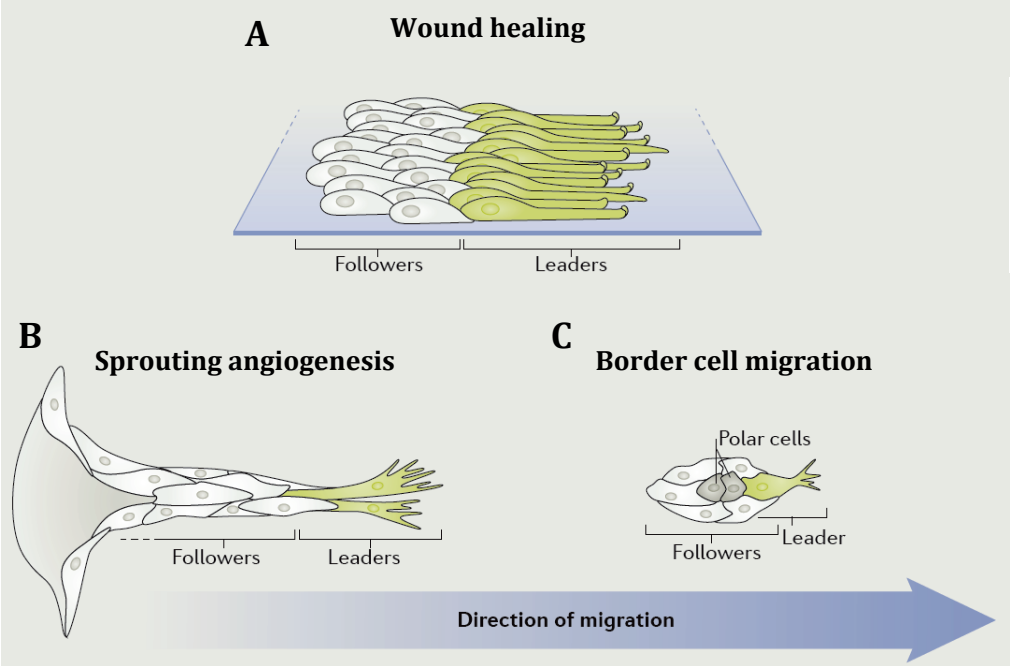

Figure 3. Spatial sub-organizations of leader and follower cells in the migrating group. (A) The movement of the cell monolayer during wound healing is driven by a first row of leader cells; **(B)** During sprouting angiogenesis two leader cells (tip cells) are able to guide the migration of endothelial sprouts; **(C)** The small cluster of *D. melanogaster* border cells is controlled by a single leader cell. Leader cells (green), follower cells (gray).
Adapted from Mayor and Etienne-Manneville, 2016

Leaders and followers can also be clearly distinguished in terms of cell morphology and gene expression. While leader cells usually have a prominent leading edge and a more mesenchyme-like appearance, follower cells tend to form more epithelial-like

packaged cell aggregates (Friedl and Gilmour, 2009). Moreover, it was also shown they possess distinct genetic signatures, as leader cells have higher expression of surface receptors (*e.g.* chemokine receptors CXCr4 and CXCr7) (Aman and Piotrowski, 2008), enabling them to sense external signals (*e.g.* chemoattractants) and guide follower cells more efficiently. Functionally, leader cells are also capable to secrete metalloproteinases that degrade the extracellular matrix (ECM), which has a direct impact in the migratory behavior of the follower cells, increasing the polarized organization of the group and facilitating cluster movement (Gabrial and Krasnow, 2006; Peng *et al*., 2013; Nguyen *et al*., 2000; Wang *et al*., 2010).

I.3. The molecular mechanisms of cell migration

Mechanistically, the basic molecular events driving single cell migration also apply to cells migrating collectively. As mentioned before, single cell migration depends on the establishment of a front-rear polarity axis, which ultimately dictates the migratory behavior of each cell. Underlying this front-rear polarization is a polarized distribution of signaling pathways controlling cytoskeleton remodeling and protein recycling (Mayor and Etienne-Manneville, 2016).

In particular, the small GTPase proteins of the Rho family, which are known as cytoskeleton regulators, have been extensively studied in the context of cell migration. The Rho family comprises more than 20 members, including Rac1, RhoA and Cdc42 (Jaffe and Hall, 2005). As other small GTPases, these Rho proteins are able to cycle between active (GTP-bound) and inactive (GDP-bound) states, which are catalysed by guanine-nucleotide exchange factors (GEFs) and GTPase-activating proteins (GAPs), respectively. Furthermore, they are also able to cross-regulate each other's activity (Iden and Collared, 2008). While Cdc42 is able to activate Rac1 (Nobes and Hall, 1995), Rac1 and RhoA antagonize each other's activity (Rottner *et al*., 1999).

At the leading edge, Rac1 and Cdc42 are able to induce rapid actin polymerization, promoting the formation of membrane protrusions such as lamellipodia (Jaffe and Hall, 2005) and filopodia (Gupton and Gertler, 2007), respectively. On the other hand, at the cell rear, a distinct signaling pathway involving RhoA and Rho-kinases (ROCKSs) induce the formation of stress fibers that promote acto-myosin contraction (Figure 4) (Wheeler and Ridley, 2004). This leads to the formation and establishment of a front-

rear gradient of active Rac1 and RhoA that mutually inhibit each other, ensuring the maintenance of these spatial domains throughout the process of cell migration.

In addition to be regulated spatially, the activation of Rho GTPases has also been shown to be controlled temporally. For instance, RhoA which is mostly active at the back of the cell during cell migration, can also be found at the leading edge during the initial protrusion events before Rac1 and Cdc42 take over to reinforce and expand the newly-formed protrusions (Machacek *et al.*, 2009; Pertz *et al.*, 2006). Ultimately, it is the temporal and spatial balance between the activities of Rac1, RhoA and Cdc42 that enables the tight control of cytoskeleton remodeling necessary for directional cell migration.

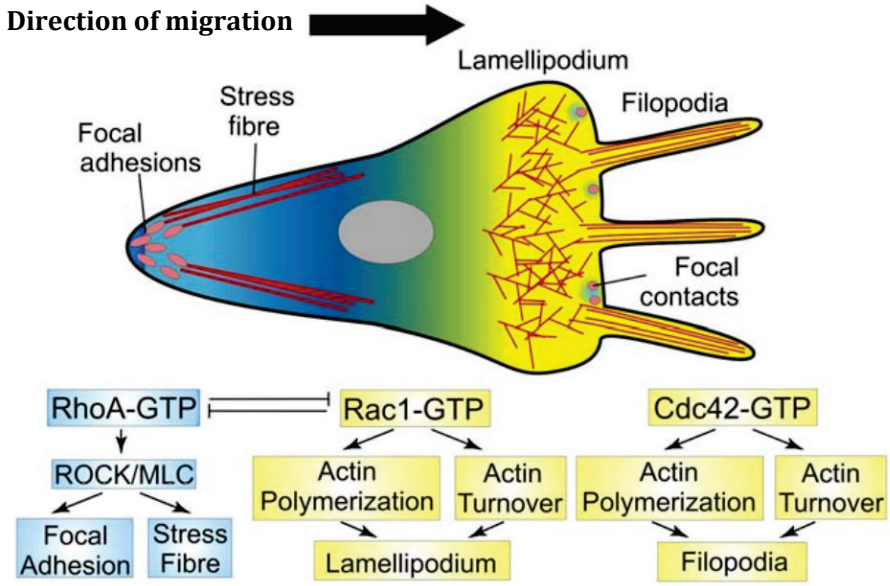

Figure 4. Spatial distribution of Rho GTPases. During cell migration, a front-rear gradient of active Rac1/Cdc42 (yellow) and RhoA (blue) is established. While CDC42 and RAC1 promote filopodia and lamellipodia formation at the leading edge, RhoA and Rho-kinases (ROCKs) at the rear of the cell induce the formation of stress fibers that promote cell contraction.

Adapted from Mayor and Carmona-Fontaine, 2010

I.4. Adherens junctions: a foundation for collective behavior

In cells migrating collectively cell-cell junctions provide mechanical and chemical coupling between adjacent cells. Indeed, it is the coordination of molecular components involved in front-rear polarization and mechanical forces within the cell

aggregate that promote collective behavior and coordinated movement of the cell cluster (Das *et al.*, 2015). Cell-cell adhesion is mediated by adherens junctions' proteins that associate to form a protein complex linking the transmembranar cadherins to the actin cytoskeleton. This complex is composed by classical cadherins, α-catenin (CTNNA1), β-catenin (CTNNB1) and p120-catenin (CTNND1). In addition to the proteins of the core complex, other F-actin-associated proteins such as vinculin, zyxin and formins may also be recruited to the adherens junctions to participate in the regulation of adhesion strength and stability (Figure 5). Adherens junctions are able to assume distinct morphologies depending on various intrinsic and extrinsic factors. For instance, linear junctions are generally considered stable, whereas punctate junctions, also known as focal adhesion junctions, are more associated with remodeling events where cells form transient connections.

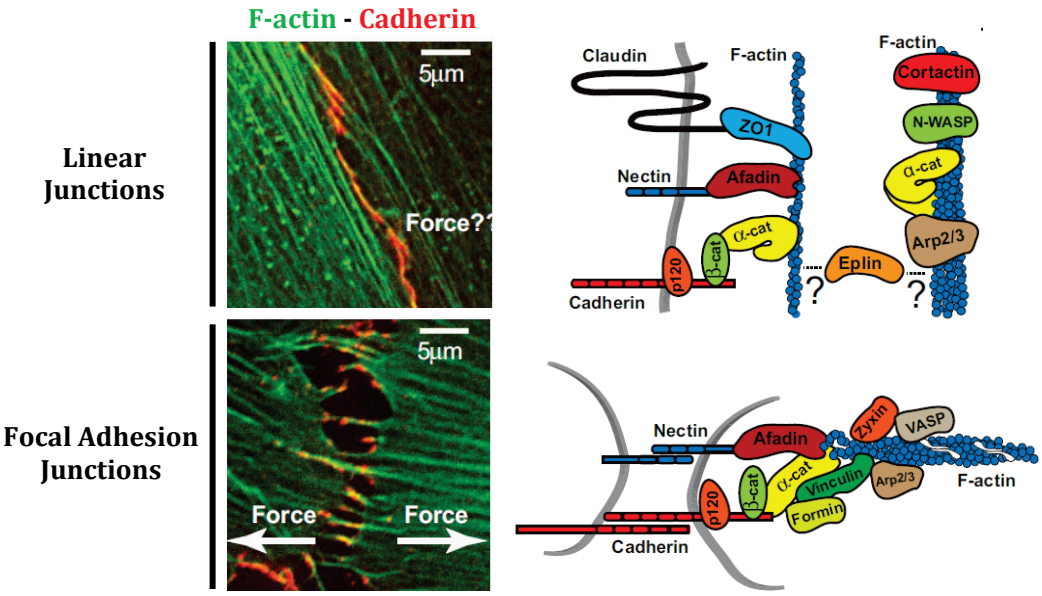

Figure 5. Adherens junction structure and organization. Cell-cell junctions are composed by a core complex of classical cadherins, catenins and F-actin associated proteins, that ensure the maintenance and regulation of cell adhesion between neighbor cells. These highly dynamic structures are capable of shifting morphology and internal organization, according to several factors, such as tension forces, cell contraction, junction maturity and remodeling. Linear junctions (top panel) are stable structures that arise predominantly in low-tension regions. They are usually associated with parallel thick actin bundles and contain low amounts of vinculin. On the other hand, focal adhesion junctions (bottom panel) are transient structures associated with remodeling events and form mostly in high-tension regions. They are generally found together with perpendicular actin bundles that exert pulling forces in opposite directions and contain high levels of vinculin.

Adapted from Huveneers and Rooij, 2013

The distribution and organization of actin bundles and vinculin is also different in these two types of junctions. While in linear junctions the actin cables run parallel to the junctions and contain very low vinculin levels, in focal adhesion junctions the actin bundles are perpendicular to the junctions, exerting pulling forces in opposite directions and vinculin levels are high (Figure 5) (Huveneers and Rooij, 2013).

In spite of providing adhesion stability, these junctions are highly dynamic structures, re-organizing and changing their morphology and composition to constantly adapt to changes in cell contractility and external stimuli. During collective cell migration, adherens junctions are constantly shifting in response to tension forces and cell contractility, as they are one of the main platforms for force transmission between neighbor cells, which will be further discussed in the next section.

In order to preserve the integrity of adherens junctions throughout cell migration while providing a degree of flexibility to cell-cell contacts, the molecular components constituting the cell junctions must be constantly relocated and recycled. This process known as treadmilling, involves the retrograde flow of adherens junctions components along lateral contact sides driven by transverse acto-myosin cables positioned perpendicularly to the front-rear axis of the migrating cells (Figure 6). This movement terminates with the dissociation of cadherins at the cell rear and subsequent internalization and recycling towards the leading edge, enabling the formation of new cell-cell junctions. When this polarized trafficking of junctional components is perturbed, adherens junctions become unstable, which negatively affects the migration speed and the ability of leader cells to polarize during collective cell migration (Peglion *et al.*, 2014).

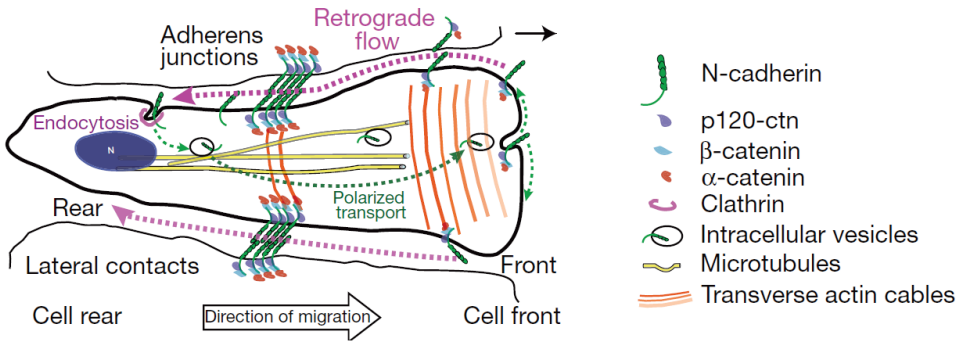

Figure 6. Adherens junctions retrograde transport during cell migration. Lateral adherens junctions are linked to transverse acto-myosin cables that move together in a retrograde flow (purple dashed line), which is essential to the maintenance and flexibility of cell-cell contacts during migration.

Adapted from Peglion *et al.*, 2014

I.5. Mechanotransduction in the context of collective migration

Mechanotransduction is the process by which cells are able to sense and translate the mechanical stimuli they receive into intracellular biochemical signals, which enables cells to develop an adaptive response to the physical microenvironment (Figure 7) (Haase and Pelling, 2015; Jaalouk and Lammerding, 2009). This response is complex and depends mostly on the type, magnitude and rate of the physical forces exerted (Guolla *et al*., 2012; Pravincumar *et al*., 2012). External forces, such as shear stress and tension/compression, are sensed by membrane surface receptors and transmitted through the plasma membrane and focal adhesions to the cell cytoskeleton, affecting transcription and gene expression (Booth-Gautier *et al*., 2012; Dahl and Kalinowski,

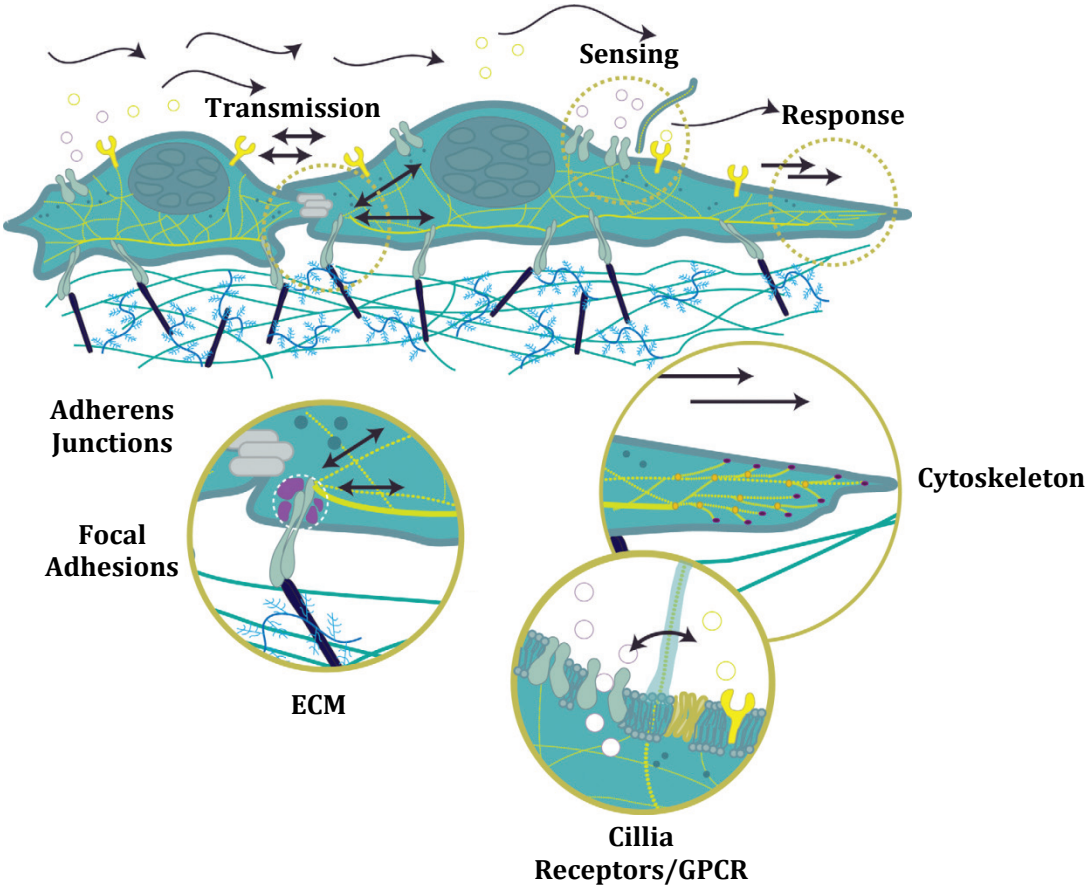

Figure 7. Overview of mechanotransduction. During mechanotransduction cells must be able to sense the mechanical stimuli, produce a biochemical response and also transmit the signal to neighbor cells. External forces can be sensed by membrane surface receptors (primary cilia, stretch-activated ion channels, GPCRs) or by focal adhesions when forces are from the extracellular matrix (ECM) and transmitted to the cell cytoskeleton to produce a response. The mechanical stimuli can also be transmitted to adjacent cells through adherens junctions to generate a multicellular response.

Adapted from Haase and Pelling, 2015

2011). On the other hand, internal forces generated within the cell cytoplasm by actin polymerization or through the action of motor proteins (Ji *et al*., 2008) are conveyed to the surrounding substrate and have a role in cell migration (Ananthakrishnan and Ehrlicher, 2007), mitosis (Moore and Cooper, 2010) and cell-cell communication (Reinhart-King et al., 2008).

Collective cell migration relies on the mechanocoupling between cells to coordinate spatial positioning and traction force generation required for oriented cell movement. In cohesive cell groups, leader cells are able to generate sufficient traction forces to drag and coordinate the migration persistence of followers up to ten cells behind the leading edge (Vitorino and Meyer, 2008). Combined analysis of traction force distribution and Rho GTPases activity demonstrated that traction forces are higher in leader cells and that correlates with increased RhoA activity (Reffay *et al*., 2014). These mechanical forces are then transmitted through acto-myosin stress fibers from the leaders to several rows of follower cells trailing behind. The precise mechanisms enabling mechanotransduction propagation vary according to the context in which cells are migrating. In 2D sheets the leaders (and in some cases the followers as well) develop polarized lamellipodia driving the migration of the group forward (Farooqui and Fenteany, 2005; Nobes and Hall, 1999). During wound healing, an example of migration in a 2D environment, leader cells develop mature focal adhesions that recruit a series of adaptor proteins, such as cortactin, paxilin, talin and vinculin, and connect integrins to the acto-myosin cables of the cell cytoskeleton. This promotes cell contraction which is then transmitted to the followers via adherens junctions (Nobes and Hall, 1999; Zaidel-Bar *et al*., 2007). In 3D collective cell migration, such as sprouting angiogenesis or cancer invasion, tip cells sense the microenvironment and make use of filopodia or pseudopodia to drive the migration of cell strands, respectively (le Noble *et al*., 2008; Wolf *et al*., 2007).

Although leaders have been more commonly referred as the main contributors for force generation in the context of collective cell migration, followers are also capable of generating pulling forces. Previous studies have demonstrated that stress tension builds up far away from the leading edge in migrating monolayers, implying that forces cannot be generated solely by leader cells. Therefore, follower cells must also participate in this process to enable the long-range propagation of traction forces across the monolayer through cell-cell adhesions, creating a “tug-of-war” scenario

involving leaders and followers (Tambe *et al*., 2011; Trepat *et al*., 2009). However, the specific contributions of leaders and followers to force generation and transmission are still controversial in the mechanobiology field.

Besides force generation and mechanical coupling, cells within the group must also be able to sense and respond to the physical forces exerted onto them. This is driven by specific mechanotransducer proteins present at focal adhesions and adherens junctions that are able to alter their conformation in response to mechanical forces. These proteins, such as talin in focal adhesions and α-catenin in adherens junctions, couple integrins and cadherins to the acto-myosin cytoskeleton, respectively (Figure 8). When mechanical forces are at play, these mechanotransducers undergo conformational changes, leading to the activation of specific signaling pathways, which enables a tight control over the strength and stability of cell adhesions (Mayor and Etienne-Manneville, 2016). For instance, upon tension, α-catenin switches from a closed to an open conformation, exposing a vinculin-binding domain. This promotes

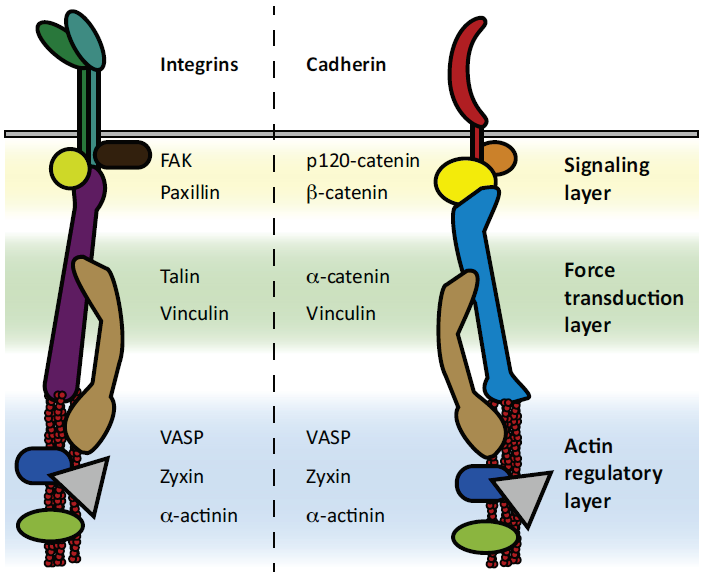

Figure 8. Overview of mechanotransduction in focal adhesions and adherens junctions. Focal adhesions (left) and adherens junctions (right) share the same general organization, comprising a signaling layer (yellow) responsible for sensing external stimuli, a force transduction layer (green) that transmits the mechanical signals received and an actin regulatory layer (blue) that controls cell contractility and cytoskeleton remodeling. A key conserved feature between integrin and cadherin complexes is the presence of mechanotransducer proteins – talin (purple) and α-catenin (light blue) – which are able to switch to an open conformation when tensions forces are applied and recruit vinculin (light brown), promoting the strengthening of adhesion complexes.

Adapted from Han and Rooij, 2016

vinculin recruitment, and presumably results in a reinforcement of the junctions, preventing them from breaking (Huveneers and Rooij, 2013; Yonemura *et al*., 2010). During this process tension forces also seem to stabilize the connection between α-catenin and actin, therefore ensuring the long-term coupling of external mechanical forces to the cell cytoskeleton (Buckley *et al*., 2014).

I.6. Angiogenesis: a collective cell migration-driven process

The vertebrate body contains a broad hierarchical blood vessel network lined by a monolayer of endothelial cells (ECs) devised to allow the transport and distribution of nutrients and oxygen to all tissue types present in the body. In the early embryo, following an initial stage of vasculogenesis, the formation of the blood vessel network is mostly mediated by angiogenesis. This biologic process is a complex multi-step program that ultimately allows blood vessels to invade avascular tissues and expand the pre-existing network (Ehling *et al*., 2013; Herbert and Stainier, 2011).

Sprouting angiogenesis is the process that allows the formation and expansion of the vascular network driven by the collective migration of strands of ECs. Initially, quiescent ECs receive pro-angiogenic signals provided by growth factors and chemokines (*e.g.* VEGF-A and CXCL12) that promote their detachment from the basement membrane. Activated ECs become motile and highly invasive, which results on the onset of vessel sprouting (Adams and Alitalo, 2007; Carmeliet and Jain, 2011). However, from all the ECs exposed to pro-angiogenic stimuli, only a small fraction will be selected to become the leaders of the newly-formed blood vessel sprouts. These leaders, also known as endothelial tip cells, are specialized ECs that are able to extend numerous filopodia that sense attractive or repulsive cues from the microenvironment and are responsible for guiding the migration of the vessel sprouts (De Smet *et al*., 2009; Gerhardt *et al*., 2003). The ECs trailing behind the tip cells are called stalk cells. These cells are proliferative and support the extension of the new vessel segments, while ensuring their connectivity to the parental vessel. Moreover, at later stages these stalk cells are also responsible for lumen formation on the growing blood vessel branches (Iruela-Arispe and Davis, 2009; Kamei *et al*., 2006). EC sprouting usually culminates with the fusion of tip cells from adjacent vessel segments through a process called anastomosis. Once tip cells establish a connection, they lose mobility, assemble

cell-cell junctions and incorporate into the recipient vessel segment to give rise to a continuous lumenized blood vessel. These blood vessels will further extend and mature to allow blood flow circulation (Figure 9) (Herbert and Stainier, 2011).

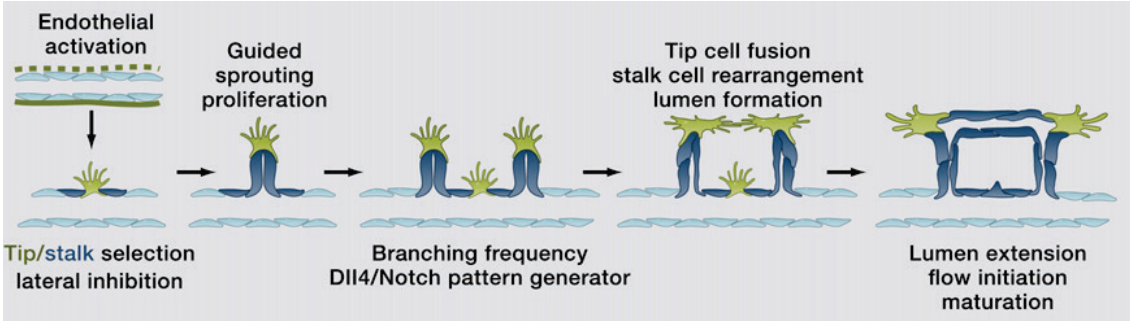

Figure 9. Sprouting angiogenesis. Sprouting angiogenesis comprises 5 essential steps: **(I)** Endothelial cell activation and tip/stalk selection through lateral inhibition mediated by Notch signaling; **(II)** Tip cell guided migration and stalk cell proliferation; **(III)** Branching patterning; **(IV)** Tip cell anastomosis and lumen formation; **(V)** Perfusion and vessel maturation.
Adapted from Potente *et al.*, 2011

This phenotypic distinction between tip and stalk cells at the sprouting front is mainly controlled by the Notch/VEGF signaling pathway (Eilken and Adams, 2010; Phng and Gerhardt, 2009). ECs express several Notch receptors (NOTCH1 and NOTCH4) and ligands (DLL1, DLL4, JAG1 and JAG2) that are differentially expressed in tip and stalk cells. Studies in mouse and zebrafish have revealed that tip cells express high levels of the Notch ligand DLL4, which will promote Notch activation in adjacent stalk cells, resulting in the lateral inhibition of the tip cell phenotype (Fig.I.6-2). In addition, VEGF-A/VEGFR2 signaling cooperates with Notch to induce the upregulation of DLL4 and promote tip cell specification. Conversely, in stalk cells lateral inhibition mediated by Notch signaling prevents tip cell behavior by downregulating VEGFR2, VEGFR3 and NRP1 while upregulating VEGFR1, rendering these cells less responsive to VEGF stimulation. As a result, during the initial steps of endothelium activation, the ECs exposed to the highest levels of VEGF signaling will be selected to become tip cells, whereas, in the neighboring stalk cells, the tip cell fate will be repressed by lateral inhibition. Unlike DLL4, the Notch ligand JAG1 is expressed mainly by stalk cells. However, unlike DLL4, its ability to induce Notch activation is much reduced. Hence, instead of acting to induce Notch activation, JAG1 participates mostly on the regulation of the Notch/DLL4 feedback loop that signals back to tip cells by antagonizing DLL4 and reducing Notch activation in these cells (Figure 10) (Potente *et al.*, 2011).

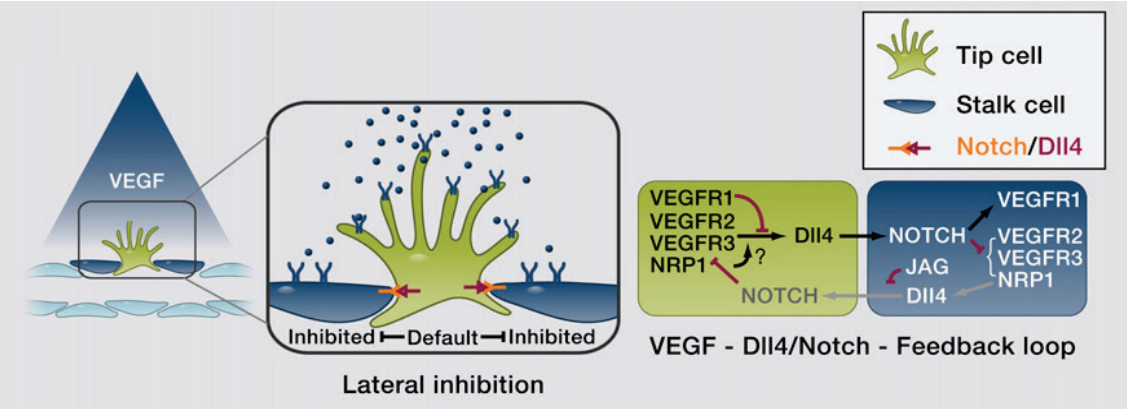

Figure 10. VEGF/Notch signaling control tip/stalk cell fate determination through lateral inhibition. Endothelial cells exposed to higher levels of VEGF are selected to become tip cells and start expressing higher levels of the Notch ligand DLL4, which will induce Notch activation in neighbor stalk cells, resulting in the lateral inhibition of the tip cell fate.

Adapted from Potente *et al.*, 2011

Despite the tight control of tip/stalk fate determination by VEGF/Notch signaling, studies indicated that ECs are able to actively switch from one developmental program to the other during sprouting angiogenesis *in vitro* and *in vivo* (Jakobsson *et al.*, 2010). This degree of plasticity becomes evident upon analyzing EC behavior at the sprouting front, where cells actively compete for the tip cell position. Although all ECs are able to respond to VEGF stimulation, those that express DLL4 more quickly and/or at higher levels acquire a competitive advantage over others to become tip cells and activate Notch signaling in adjacent cells more efficiently (Potente *et al.*, 2011).

As previously mentioned, the net outcome of this dynamic process is the generation of a highly dense but immature vascular plexus. Yet, in order to evolve into a functional hierarchically branched network, blood vessels must mature while preserving continuous blood flow, a process that involves extensive vascular remodeling (Potente *et al.*, 2011). One of the key aspects of vascular remodeling is blood vessel regression, a process during which the connection between previously formed immature blood vessels is lost (Figure 11). Previous studies performed in the zebrafish brain (Chen *et al.*, 2012; Kocchan *et al.*, 2013; Murphy *et al.*, 2012) and in the mouse retina (Franco *et al.*, 2015) have highlighted the importance of EC polarization and coordinated migration away from the regressing vessel branches. Even though a growing body of literature supports the fact that reduced or fluctuating blood flow is the main inducer of branch regression (Chen *et al.*, 2012), the specific molecular and cellular

mechanisms that collectively regulate vascular remodeling remain largely unknown. However, a recent study by Franco *et al* (Franco *et al.*, 2016) has already identified non-canonical Wnt signaling as one of the key pathways controlling cell junction stability and promoting EC collective behavior in the course of angiogenesis, which will be further explored in the next section.

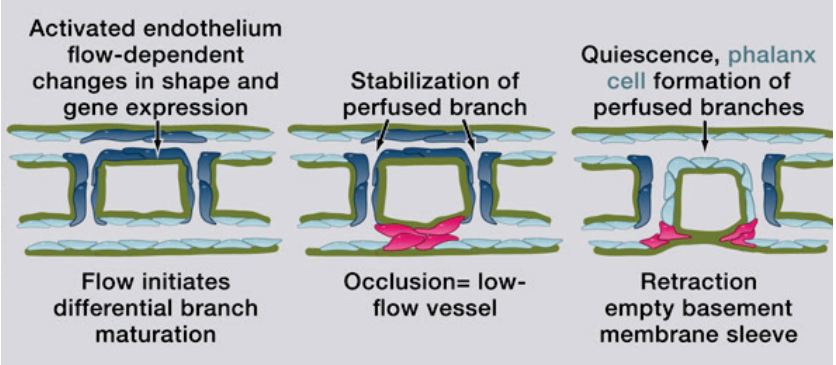

Figure 11. Vascular remodeling and vessel regression. Vascular remodeling is the process that allows the transition from a highly dense immature plexus to a functional hierarchical blood vessel network and includes a series of sequential steps: **(I)** Flow onset and blood vessel maturation; **(II)** Vessel regression initiation driven by the lack of flow and stabilization of perfused vessel segments; (III) Vessel retraction conclusion and quiescence establishment.
Adapted from Potente *et al.*, 2011

I.7. Canonical and non-canonical Wnt signaling

Wnt ligands are secreted signaling molecules known to control several cellular processes, such as proliferation, differentiation, asymmetric division, patterning and cell fate determination through modulation of gene expression, cell behavior, adhesion and polarity (Huelsken and Birchmeier, 2001; Moon *et al.*, 1997; Moon *et al.*, 2002). During development, these ligands act as morphogens and regulate the patterning of the embryo by triggering concentration-dependent autocrine and paracrine responses (Neumann and Cohen, 1997; Zecca, 1996). To date, 19 evolutionarily conserved Wnt glycoproteins have been identified in mice, which signal through distinct signaling branches including a canonical or Wnt/β-catenin-dependent pathway and the non-canonical or β-catenin-independent pathway. The latter can be further subdivided into the Planar Cell Polarity (PCP) and the Wnt/Ca^{2+} pathways. There are more than 15 distinct Wnt receptors and co-receptors that share

some degree of redundancy. Thus, the selection of the downstream pathway is determined by the specific combination of Wnt ligands with receptors and co-receptors. And, as a consequence, Wnt ligands cannot be rigorously assigned to a unique specific signaling branch. However, in general terms, Wnt1, Wnt3a and Wnt8 have been often associated with canonical signaling, whereas Wnt5a and Wnt11 are mostly involved in non-canonical Wnt signaling (Kikuchi *et al*., 2011). Moreover, although Frizzled proteins act as receptors for both signaling branches, the co-receptors LRP5 and LRP6 or ROR1 and ROR2 determine the specificity of the canonic or non-canonic pathways, respectively (Niehrs, 2012).

During canonical Wnt signaling, the binding of Wnt ligands to their Frizzled/LRP receptor complexes causes a stabilization of cytoplasmic β-catenin, which is normally targeted to proteolytic degradation through phosphorylation by the GSK-3/APC complex. Unphosphorylated, stabilized β-catenin is then translocated into the nucleus and by associating with Lef1/TCF transcription factors, modulates the expression of specific target-genes. This pathway is mostly involved in the control of cell differentiation and proliferation (Niehrs, 2010; Reya and Clevers, 2005; Wray and Hartmann, 2012). On the other hand, the less-characterized non-canonical Wnt pathways are independent of β-catenin and transduce Wnt signals through either JNK/PCP or PKC/CamKII pathways (Kohn and Moon, 2005; Minami *et al*., 2010). The PCP pathway induces the activation of distinct Rho GTPases, RhoA, Rac1 and Cdc42 responsible for cytoskeleton remodeling. RhoA and Rac1 are able to trigger the activation of ROCK and JUN-N-terminal kinase (JNK), respectively, resulting in microtubule stabilization and actin polymerization. This pathway is also characterized by the asymmetric distribution of signaling components, such as Frizzled receptors, Ceslr1, Vangl2 and Prickle. It is essential for the regulation of tissue polarity, asymmetric cell division, cell motility and morphogenetic movements. The Wnt/Ca^{2+} pathway leads to an increase of intracellular calcium, resulting in the activation of Calmodulin-dependent kinase II (CAMKII), protein kinase C (PKC) and Calcineurin. Calcineurin will then activate nuclear factor of activated T cells (NFAT), which controls the transcription of genes involved in cell fate determination and migration (Figure 12) (Franco *et al*., 2009; Niehrs, 2012).

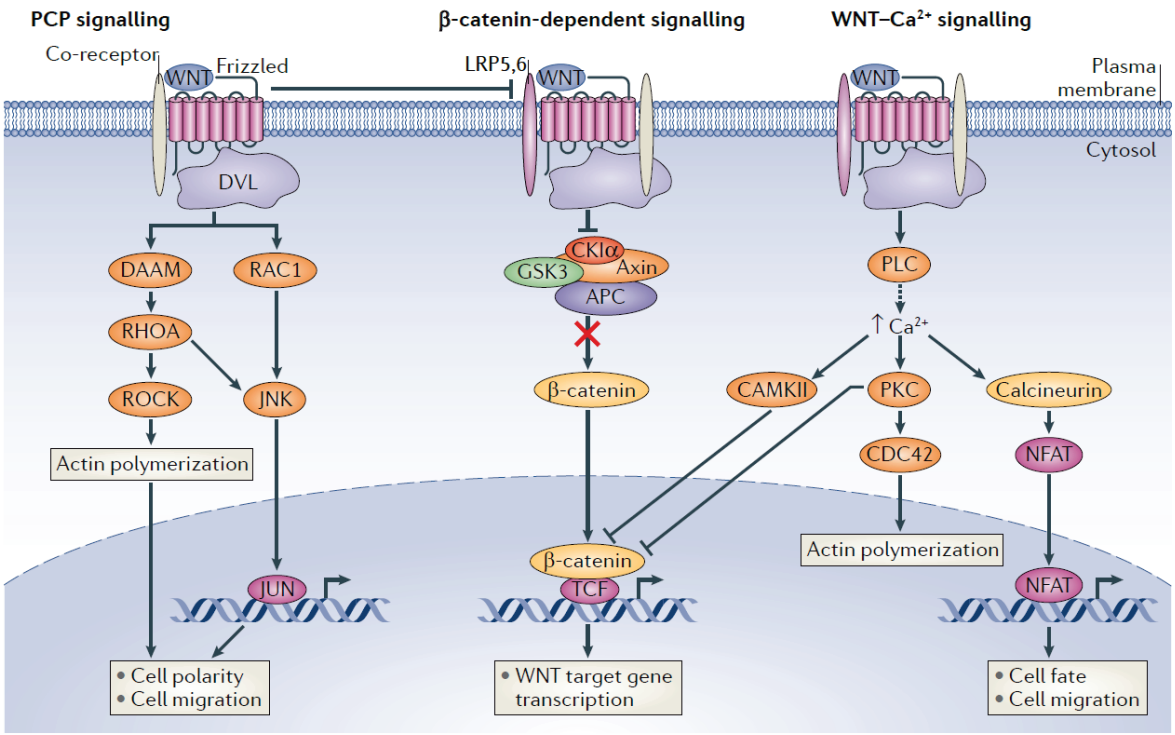

Figure 12. Wnt signaling pathways overview. There are 3 main Wnt signaling branches described to date: **(I)** PCP signaling (left) that triggers the activation of Rho GTPases and their effectors, leading to cytoskeleton rearrangements and actin polymerization. This pathway is mainly involved in the control of tissue polarity, cell mobility and morphogenetic movements; **(II)** β-catenin-dependent signaling, where the binding of Wnt ligands prevents β-catenin degradation by the GSK-3/APC complex, enabling its translocation into the nucleus and target-gene transcription. This pathway is important for cell differentiation and proliferation; **(III)** Wnt/Ca^{2+} signaling induces an increase in intracellular calcium levels, which leads to the activation of CAMKII, PKC and the transcription factor NFAT. It is mostly important in the regulation of cell fate determination and cell migration.
Adapted from Niehrs, 2012

I.8. Wnt signaling in collective cell migration

One of the most well described functions of Wnt signaling is its role in controlling cell movements during the process of vertebrate gastrulation. For instance, the non-canonical Wnt PCP pathway was shown to regulate both cell polarity and movements (mediolateral narrowing and anteroposterior elongation) of mesodermal and ectodermal cells during convergent extension and neural tube closure (Keller *et al.*, 2003; Veeman *et al.*, 2003). In Xenopus, maternal Wnt11 activates the canonical Wnt signaling branch, participating in the establishment of the dorsal Spemann-Mangold Organizer (Tao *et al.*, 2005). Blocking the Wnt/β-catenin pathway in the Xenopus embryo leads to inhibition of convergent extension movements, while ectopic

activation in the vegetal pole induces the formation of a secondary dorsal-ventral axis (De Robertis *et al*., 2000; Kühl *et al*., 2001). Besides axis formation, canonical Wnt signaling also plays a major role during neural patterning and tail formation at later developmental stages (Komiya and Habas, 2008). While canonical Wnt signaling is required for convergent extension and dorsal axis formation, the Wnt/Ca^{2+} pathway is able to block convergent extension movements, acting as a negative regulator of axis formation (Komiya and Habas, 2008). On the contrary, in zebrafish it has been demonstrated that activation of the non-canonical branch by Wnt11 is necessary for correct convergent extension during gastrulation and its absence leads to abnormal extension of axial tissues and other midline defects (Heisenberg, C.P. *et al*., 2000).

Besides gastrulation, Wnt signaling is also implicated in the control of other cell movements occurring in distinct cell types. For instance, non-canonical Wnt PCP signaling is crucial for collective migration of neural crest cells, participating in contact inhibition of locomotion (CIL), a process where cells repolarize and start migrating in the opposite direction upon contact with another cell (Carmona-Fontaine *et al*., 2008). Adenomatous polyposis coli (APC), a tumor suppressor regulating cell differentiation via the Wnt pathway (Näthke, 2004; Segditsas and Tomlinson, 2006), was also shown to regulate microtubule rearrangements required for astrocyte migration (Etienne-Manneville, 2009). In *Drosophila*, Wnt signaling is involved in the control of myocyte and tracheal cells migration (Chihara and Hayashi, 2000; Kozopas and Nusse, 2002). These examples clearly highlight the importance of Wnt signaling in the control of collective cell motility in various developmental settings, which certainly contributed for its conservation throughout metazoan evolution.

I.9. Wnt signaling in angiogenesis

In the context of angiogenesis, canonical Wnt signaling plays an important role during the early steps of ECs differentiation (Wang *et al*., 2006), remodeling of the embryonic vessels (Cattelino *et al*., 2003; Corada *et al*., 2010) and establishment of organ-specific vasculatures (Liebner *et al*., 2008; Stenman *et al*., 2008; Daneman *et al*., 2009). It also participates in the regulation of hyaloid vessel regression in the developing eye (Lobov *et al*., 2005) and can be activated by Norrin (Norrie Disease Protein), a cystine-knot like growth factor important for the control of retinal vasculature development (Wang

et al., 2012). Moreover, it is known to counterbalance vessel regression by stimulating EC proliferation during postnatal retinal angiogenesis (Phng *et al*., 2009).

On the contrary, the contribution of non-canonical Wnt signaling during angiogenesis is less clear and has only started to emerge recently. Wnt5a, a non-canonical Wnt signaling ligand, has been described as a pro-angiogenic factor that promotes EC proliferation, migration and vascular network formation (Masckauchan *et al*., 2006; Cirone *et al*., 2008; Descamps *et al*., 2012). More recently, Franco *et al* has shown that combined loss of non-canonical Wnt ligands – Wnt5a and Wnt11 – in retinal endothelial cells resulted in decreased radial expansion and vessel density in the mouse retina, accompanied by a higher number of regressing blood vessel segments (Franco *et al*., 2016). Interestingly, apoptosis and EC numbers remained unaffected, contrary to what had been reported in other studies (Korn *et al*., 2014), suggesting that non-canonical Wnt signaling does not affect cell survival. Instead, it seems to prevent excessive and premature vessel disconnection by stabilizing vessel connections. This is essential during the initial phase of sprouting angiogenesis to enable oriented migration of vessel sprouts and the subsequent expansion of the vascular plexus, and also later on during vessel remodeling to allow the formation of a functional hierarchical blood vessel network. Although subsequent work from our group led us to conclude that Wnt5a was the most important ligand operating in the system (Franco *et al*., 2016), it is still unclear how non-canonical Wnt signaling exerts these functions and which specific molecular components could be activated downstream the initial ligand/receptor coupling.

Chapter II. Objectives

Previous studies have demonstrated that non-canonical Wnt signaling is important for the expansion of the vascular plexus and vessel stabilization *in vivo* (Franco *et al*., 2015; Franco *et al*., 2016). However, the mechanisms that mediate the effects of non-canonical Wnt ligands on vascular biology, in particular during sprouting angiogenesis, remain elusive. Non-canonical Wnt signaling has been associated with tissue polarity regulation, cytoskeleton remodeling and blood vessel stabilization (Franco *et al*., 2015; Niehrs, 2012). We hypothesized that non-canonical Wnt signaling may affect EC ability to polarize correctly, thus impairing their directed migration capability. Therefore, to test this working hypothesis we propose to:

I. Analyze the effect of non-canonical Wnt signaling in EC polarity and collective migration *in vitro*;

II. Measure the effect of non-canonical Wnt signaling in endothelial cell-to-cell force transmission;

III. Investigate the influence of non-canonical Wnt signaling on EC junctions;

IV. Identify the signaling mechanism downstream Wnt5a that regulates cell polarity and collective cell migration.

Chapter III. Materials and Methods

III.1. Culture of HUVECs

Human umbilical vein endothelial cells (HUVECs) were routinely cultured following the manufacturer's guidelines, in filter-cap T75 flasks Nunclon Δ surface treatment (VWR international, LLC) and cultured at 37ºC and 5% CO_2 to ensure a stable environment for optimal cell growth. HUVECs (C2519A, Lonza) were cultured with complete medium EGM-2 Bulletkit (CC-3162, Lonza) supplemented with 1% penicillin/streptomycin (#15140122, Gibco). When passaging cells for experiments, cells were washed twice in sterile PBS (137mM NaCl, 2.7mM KCl, 4.3mM Na_2HPO_4, 1.47mM KH_2PO_4, pH7.4). Then, cells were incubated for 3-5min in trypsin/EDTA (#15400054, Gibco) or in TrypLE™ Express (#12605-028, Gibco) at 37ºC, 5% CO_2. When 95% of the cells detached, complete medium was added to each flask to inhibit the activity of the trypsin/EDTA or TrypLE™ Express and the cell suspension was transferred to a falcon tube. To maximize the amount of cells collected, all flasks were washed again with complete medium, which was added to the cell suspension gathered previously. HUVECs were then centrifuged at 115g for 5min at room temperature. The pellet was re-suspended in fresh complete medium. The cell concentration present in the suspension was determined using a Neubauer Chamber Cell Counting (Hirschmann EM Techcolor). All cells were then seeded on the desired culture vessels at 200.000–300.000 cells/mL and placed in the incubator. All experiments with HUVECs were performed between passages 3 and 6.

III.2. siRNA transfection

In order to silence the expression of genes of interest, a set of ON-TARGET human siRNAs were purchased from Dharmacon (see Table 1). Briefly, HUVECs were seeded the day before the transfection to reach 70-80% confluence and were then transfected with 25nM of siRNA using the DharmaFECT 1 reagent (Dharmacon, GE Healthcare) following the Dharmacon siRNA Transfection Protocol. 24h after transfection the culture medium was replaced by fresh complete medium and cells were kept under culture conditions up until 72h post-transfection and then processed for immunofluorescence, protein or RNA extraction.

Table 1. List of siRNAs used.

Name	Vendor	Sequence	Cat No
Control siRNA	Dharmacon	UGGUUUACAUGUCGACUAA	D-001810-01
siACTR3	Dharmacon	GGAAUUGAGUGGUGGUAGA	J-012077-08
siARHGEF7	Dharmacon	GGACGAGCUUUCCUUCUCA	J-009616-07
siCDC42	Dharmacon	GAUGACCCCUCUACUAUUG	J-005057-07
siCDH5	Dharmacon	GAGCCCAGGUCAUUAUCAA	J-003641-07
siCTNNA1	Dharmacon	GAUGGUAUCUUGAAGUUGA	J-010505-06
siFZD4	Dharmacon	GAUCGAUUCUUCUAGGUUU	J-005503-06
siFZD6	Dharmacon	GAAGGAAGGAUUAGUCCAA	J-005505-07
siFZD7	Dharmacon	UGAUGUACUUUAAGGAGGA	J-003671-11
siFZD8	Dharmacon	UCACCGUGCCGCUGUGUAA	J-003962-08
siROR1	Dharmacon	UGACUUGUGUCGCGAUGAA	J-003171-09
siROR2	Dharmacon	GCAGGUGCCUCCUCAGAUG	D-003172-06
siRYK	Dharmacon	GGUUUGUUGUGCAGUAAUA	J-003174-11
siVCL	Dharmacon	UGAGAUAAUUCGUGUGUGUUA	J-009288-05
siWNT5A	Dharmacon	SMARTpool	L-003939-00-0005

III.3. Viral production and transduction

Replication-incompetent lentiviruses were produced by transient transfection of HEK293T of pLX303 lentiviral expression vector co-transfected with the viral packaging vector Δ8.9 and the viral envelope vector VSVG. Medium was replaced with fresh culture medium 6-8h post transfection. 48h after medium replacement, lentiviral particles were concentrated from supernatant by ultracentrifugation at 90000g for 1h30 and re-suspended in 0.1% BSA PBS.

Seeded HUVECs were transduced 24h post-transfection with varying concentrations of lentiviral plasmids containing VE-cad-TS, VE-cad-TL, Wnt5a-V5, Cdc42-2G, Vinculin-Full-Length-GFP, Vinculin-T12-mutant-GFP, α-catenin-vinculin-HA, α-catenin-vinculin(Mut)-HA and VE-cadherin-α-catenin-HA fusion protein sequences (see Table 2). 24h after viral transduction the culture medium was replaced by fresh complete medium and cells were kept under culture conditions up until 48h post-transduction and then processed for immunofluorescence or imaging. In the analysis, we used a mix population containing transduced and non-transduced cells, selecting areas where high transduction efficiencies were observed.

Table 2. List of constructs used.

Name	Construct information
Cdc42-2G	pLenti-Cdc42-2G was a gift from Olivier Pertz (# 68813 Addgene)
Lifeact-mCherry	Gift from Edgar Gomes (Instituto de Medicina Molecular)
VE-cad-TL	Commercial retrovirus (pLPCX-VEcadTS, #45848 Addgene) / Gift sequence inserted into lentiviral backbone (pLX303, #25897 Addgene)
VE-cad-TS	Commercial retrovirus (pLPCX-VEcadTL, #45849 Addgene) / Gift sequence inserted into lentiviral backbone (pLX303, #25897 Addgene)
VE-cad-αCat-HA	Commercial sequence (cloned in pUC57, GenScript) inserted into lentiviral backbone (pLX303, #25897 Addgene)
Vinculin-Full Length-GFP	Commercial sequence (pEGFPC1/GgVcl 1-1066, #46265 Addgene) inserted into lentiviral backbone (pLX303, #25897 Addgene)
Vinculin-T12 mutant-GFP	Commercial sequence (pEGFPC1/GgVcl 1-1066 T12 mutant, #46266 inserted into lentiviral backbone (pLX303, #25897 Addgene)
Wnt5a-V5	Gift sequence inserted into lentiviral backbone (pLX303, #25897 Addgene)
αCat-Vinc(Mut)-HA (vinculin P57A)	Commercial sequence(cloned in pUC57, General Biosytems) inserted into lentiviral backbone (pLX303, #25897 Addgene) with a point mutation at the Arp2/3 binding site
αCat-Vinc-HA	Commercial sequence (cloned in pUC57, General Biosytems) inserted into lentiviral backbone (pLX303, #25897 Addgene)

III.4. Site directed mutagenesis

Site directed mutagenesis was performed in αCat-Vinc-HA lentiviral plasmids in order to inhibit the Arp2/3 complex ligation to Vinculin. For this, Polymerase Chain Reaction (PCR) was executed with Herculase II Fusion DNA Polymerase (HPA600675, Soquimica) following the manufacturer's guidelines and a temperature gradient from 65ºC to 55ºC in the step of plasmid amplification. To produce αCat-Vinc-HA lentiviral plasmid, point mutation consisted in substituting a Proline to an Alanine (described by Kris A. DeMali et al., 2002) in the position 57 of vinculin's fusion protein sequence in the plasmid using forward primer 5' CCAGGCCCCCACCAGCAGAAGAGAAGGATG 3' and reverse primer 5' CATCCTTCTCTTCTGCTGGTGGGGGCCTGG 3' (primers designed based on http://www.bioinformatics.org/primerx/). PCR product was then digested 3h at 37ºC using restriction enzyme DpnI (R0176S, New England Biolabs) to eliminate original plasmids. Digested PCR product was transformed into 50uL chemically competent Stbl3 E.Coli cells (C7373-03, Life Technologies) and then plasmid concentration was increased using GeneJET Plasmid Miniprep Kit (K0503, Bioportugal) following the manufacturer's guidelines. Then, Sanger Sequencing (GATC Biotech) confirmed point mutations in the plasmids.

III.5. Wound-healing assay and drug treatment

To assess functional collective cell behavior properties (*i.e.*, polarity and migration), as well as morphological features of *in vitro* cultured HUVECs, we used the wound-healing assay. The wound was created by scratching the surface of a well-plate or a microscopy glass slide containing a monolayer of adherent HUVECs with a 200µL pipette tip. The culture medium was then replaced by fresh complete medium and HUVECs were allowed to migrate under optimal physiological conditions. When appropriate, drugs of interest were added to the medium. (see Table 3) For immunofluorescence staining experiments, cells migrated for 5h before being fixed and stained. For live imaging experiments HUVECs migration was followed up to 16h. Imaging was performed using a Zeiss Cell Observer SD (Carl Zeiss) equipped with an EC Plan-Neofluar 10x NA 0.3 PH1. To track individual cells within the monolayer more efficiently using the cell nuclei as reference, HUVECs were incubated in 1x Hoechst for 15min at 37ºC before the onset of the time lapse. Images of the scratch front were acquired at multiple positions every 10min. Analysis of migration, including wound closure, cell speed and straightness was performed using FIJI TrackMate plug in and the Chemotaxis and Migration Tool (free software from Ibidi).

Table 3. List of pharmacological inhibitors used.

Drug	Vendor	Cat No	Concentration
BAPTA-AM	Tocris	196419	2uM - 10 uM
Blebbistatin	Tocris	1852	20 uM
Ck-666	Sigma-Aldrich	SML0006	200 uM
Ionomycin	Life Technologies	I24222	2 uM - 5 uM
ML141	Sigma-Aldrich	SML0407	10 uM
ML-7	Merck Millipore	475880	10 uM
NSC 23766	Tocris	2161	100 uM
SP600125	Sigma-Aldrich	S5567	10 uM
Thapsigargin	Tocris	1138	2 uM
Y-27632	Tocris	1254	5 uM

III.6. Particle image velocimetry (PIV) analysis

The velocity field of the moving cell sheet was calculated in Matlab using cell image

velocimetry (CIV) (Milde *et al.*, 2012) software. Interrogation windows were set to 64x64 pxls with a 50% overlap. Velocity spatial correlation was calculated in Matlab using the x-component of the velocity as in (Petitjean *et al.*, 2010). Correlation length was determined from exponential fitting of correlation curves.

III.7. Atomic Force Microscopy (AFM)

HUVECs were re-plated onto 35mm Petri dishes (TPP) 48h post-transfection from 6-well plates (on a ratio of 1 6-well plate to 2 35mm Petri dishes per condition) to attain a confluence of 60-70%. On the following day, 1h before starting the cell-cell adhesion measurements, the culture medium was replaced by PBS in one of the 35mm Petri dish replicates, to ensure cell detachment. 5min before the experiment, the culture medium of the other 35mm Petri dish replicate was replaced with serum free culture medium. An atomic force microscope NanoWizard II (JPK Instruments, Berlin, Germany) mounted on the top of an Axiovert 200 inverted microscope (Carl Zeiss, Jena, Germany) was used for the cell-cell adhesion measurements. For these experiments, tipless arrow TL1 cantilevers (Nanoworld, Neuchatel, Switzerland) were used, with a nominal spring constant of 0.03N m^{-1}, as described previously (Ribeiro *et al.*, 2016). Cantilevers were cleaned for 15 min with UV light and coated with poly-D-lysine (50 μg ml^{-1}) for at least 30 min. Cantilevers were stored in poly-D-lysine solution until use.

After that, a set of adherent cells from the other Petri dish were selected to perform the cell-cell adhesion measurements, composed of 5 force-distance curves performed on each cell, with a cell-cell contact time of 5s and a 5s pause between them. Cell–cell contact was established with an applied force of 300 pN, at a constant height and in closed-loop mode. The AFM tip resonant frequency was maintained at 2 Hz, with a z-range displacement of 50 μm. For the internal negative controls, we used 4mM EGTA, a Ca^{2+} chelating agent that is able to sequestrate calcium ions from cadherins and render them inactive and unresponsive to force transmission. EGTA was added to the serum free culture medium of the Petri dish containing the adherent cells at the time of the recordings.

III.8. Analysis of tension sensors FRET measurements

Förster Resonance Energy Transfer (FRET) images were obtained using a confocal Laser Point-Scanning Microscope 880 (Zeiss) equipped with the Zen black software with a Plan Apochromat 63x NA 1.40 oil DIC M27 objective and an argon laser featuring 405, 458 and 514nm laser lines. For FRET experiments, a MBS 458/514 beam splitter and the following filters were used: mTFP1 GaAsP, band-pass 461–520; Venus/FRET, band-pass 525–575.

Acceptor photobleaching experiments were analyzed using a custom written Matlab script. A Gaussian filter with standard deviation of 0.75 was applied to the images before analysis. The intensity in the region of interest was measured before and after bleaching. FRET efficiency was calculated as $EF = \frac{I_{post} - I_{pre}}{I_{post}}$ where I_{post} and I_{pre} are the intensity of the donor channel after and before bleaching respectively.

III.9. Analysis of Cdc42 biosensor data

The Cdc42-2G FRET biosensor activity was obtained using a widefield fluorescence microscope Axio Observer (Zeiss) equipped with a Plan-Apochromat 63x, NA 1.40, oil immersion, DIC M27 objective. For ratiometric FRET experiments we used the following excitations and emission filters: ET436/20 and ET480/40 for ECFP; ET500/20 and ET535/30 for EYFP (Chroma Technology Corp) and the images for each condition were acquired during 5min with 1s time interval. FRET experiments were performed as described by Louis Hodgson. Analysis of ratiometric FRET biosensor was performed in Matlab and the preprocessing was performed using the Biosensor Processing 2.1 software package from the Dasnuser lab (Hodgson, *et al*., 2010).

The resulting images showing the localized activation of Cdc42 were further processed to retrieve quantitative information from such maps. Briefly, junctional or free-edges regions were selected from each time lapse-image and the differential of the intensity vs time traces was calculated. For each image a region where no activation was detected was also selected to determine the level of background signal. The local maxima for each curve above background level were determined. Maxima found within three frames from each other were assumed to correspond to the same activation

event.

III.10. RNA extraction and RT-qPCR

RNA extraction was performed from HUVECs seeded on 12-well plates using the RNeasy Mini Kit (Qiagen) and the GeneJet RNA Purification Kit (Thermo Scientific) as described by the manufacturer's protocol. RNA concentration was quantified using NanoDrop 1000 (Thermo Scientific) and adjusted equally, followed by DNase I digestion (Thermo Scientific) and cDNA synthesis (Superscript IV First-Strand Synthesis System, Invitrogen). cDNA samples were then diluted in RNAse/DNAse-free water for the subsequent quantitative real-time PCR (RT-qPRC) reactions.

RT-qPCR was performed using a 7500 Fast Real-Time PCR System (Applied Biosystems) with Power SYBR Green PCR Master Mix (Applied Biosystems) following the standard program of the system previously mentioned. For each reaction, 5µL of cDNA was combined with 10µL of Power SYBR Green PCR Master Mix, 4.5µL of RNAse/DNAse free water and 0.5µL of 4µM primers pool (Forward+Reverse) (see Table 4) in a MicroAmp Fast Optical 96-well Reaction Plate (Applied Biosystems). The expression levels of each sample duplicate were then normalized to GAPDH and the $2^{-\Delta\Delta T}$ method was used to calculate relative alterations in gene expression. All siRNAs used in this work were previously validated by RT-qPCR following the $2^{-\Delta\Delta T}$ method (Figure 13).

Table 4. List of qPCR primers used.

Primer	Forward Sequence	Reverse Sequence
ACTR3	CTGTAGATGCCCGGCTGAAA	TATCGCTGCATGTGGTGTGT
ARHGEF7	CGCAAACCTGAACGGAAGCCTT	GTTTTGGCGCTGGTGCAGTAAG
CDC42	TGACAGATTACGACCGCTGAGTT	GGAGTCTTTGGACAGTGGTGAG
CDH5	TCTCCGCAATAGACAAGGACA	TGGTATGCTCCCGGTCAAAC
CTNNA1	GGACCTGCTTTCGGAGTACATG	CTGAAACGTGGTCCATGACAGC
FZD4	TTCACACCGCTCATCCAGTACG	ACGGGTTCACAGCGTCTCTTGA
FZD6	GGCAGTGTATCTGAAAGTGCGC	GATGTGGAACCTTTGAGGCTGC
FZD7	GTCTTCAGCGTGCTCTACACAG	ACGGCATAGCTCTTGCACGTCT
FZD8	GCTCTACAACCGCGTCAAGACA	AAGGTGGACACGAAGCAGAGCA
GAPDH	GTCAAGGCTGAGAACGGGAA	TGGACTCCACGACGTACTCA
ROR1	GAGGCAACCAAAACACGTCAGAG	GGCACACTCACCCAATTCTTCC

ROR2	ACGTACCCTCGTGTAGTCC	CGATGACCAGTGGAATTGCG
RYK	CAGCAAGACCTGGTACACATGG	CAAGTCTCTGGAGAGGGCATTG
VCL	TGAGCAAGCACAGCGGTGGATT	TCGGTCACACTTGGCGAGAAGA
WNT5A	TACGAGAGTGCTCGCATCCTCA	TGTCTTCAGGCTACATGAGCCG

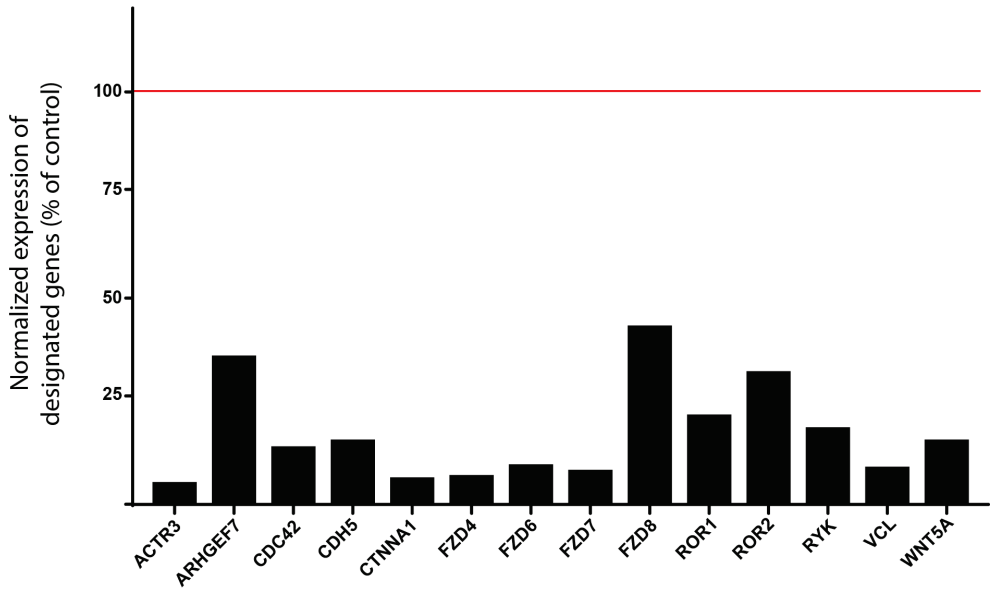

Figure 13. Quantification of RT-qPCR showing siRNA knockdown efficiency. Gene expression levels were normalized to GAPDH.

III.11. Protein extraction and Western Blotting

Protein extraction was performed from HUVECs seeded on 6-well plates which were lysed in 120µL of RIPA buffer (50mM Tris/HCl pH7.5, 1% NP-40, 150mM NaCl, 0.5% Sodium Deoxycholate, 0.1% SDS in H_2O) supplemented with phosphatase and proteinase inhibitors cocktail (1:100, #10085973 Fischer Scientific). Adherent cells were then detached from the plate with a cell scrapper and the cell lysates were gathered and transferred into an ice cold eppendorf tube. The cell lysates were then centrifuged at maximum speed for 10min at 4ºC and the supernatants collected into a new eppendorf tube. Protein concentration was quantified using the BCA protein assay kit (Pierce) following the guidelines recommended by the manufacturer. The Multimode microplate reader, Infinite M200 (Tecan), was used for spectrophotometric measurement of protein with the i-control™ software.

For Western Blotting protein samples were normalized up to 25µL and combined with

a mixture of 2x Laemmli Sample Buffer (#161-0747, Bio-rad Laboratories) with 450mM DTT (D0632, Sigma-Aldrich) and incubated at 70ºC in a Dry Block Thermostat (Grant Instruments, Ltd) for 10min (or 95ºC for 5min). Protein samples were loaded and separated on a 4-15% Mini-PROTEAN® TGX™ Gel (#456-1084, BioRad) along with 5µL of protein ladder (Full-Range RPN800E, GE Healthcare Rainbow Molecular Weight Markers), first at 50V for 5min and then at 100-130V for 1-2h in SDS-PAGE running buffer (10x SDS-PAGE: 250mM Tris, 1.92M Glycine, 1% SDS, pH8.3).

Gels were then transferred either onto a nitrocellulose membrane (iBlot Transfer Stack Regular/Mini size, #IB3010-01/-02, Invitrogen) with iBlot Dry Blotting System (Invitrogen) for 4–7min; or onto a Polyvinylidene Difluoride (PVDF) membrane (#IPVH00010, Merck Milipore) with Mini Trans-Blot® Electrophoretic Transfer Cell (Biorad) following the manufacturer's guidelines. After transfer, blotted membranes were incubated in Ponceau Red to assess transfer quality, and then washed in TBS-T (50mM Tris/HCl, 150mM NaCl, 0.1% Tween-20, pH7.5). Then, membranes were incubated in blocking buffer containing 3% BSA (Bovine Serum Albumin, MB04602, Nzytech) in TBS-T for 1h at RT, followed by an overnight incubation at 4ºC with the primary antibodies diluted in the same blocking buffer (see Table 5).

On the following day membranes were washed 3 times in TBS-T and incubated in blocking buffer containing the secondary horseradish peroxidase (HRP) conjugated antibodies for 1h at RT (see Table 6).

Before revelation membranes were washed again 3 times in TBS-T for 5min and then incubated in ECL™ Western Blotting Detection Reagent (RPN2209, GE Healthcare) following the manufacturer's protocol.

Protein bands were visualized in Chemidoc XRS+ and relative protein quantities were measured using the Image Lab software, both from Bio-Rad Laboratories. All results were normalized to tubulin levels. Some siRNAs used in this work were also validated by western blot (Figure 14).

III.12. Pulldown of active GTP-bound Cdc42

Active Cdc42 pulldown was performed from HUVECs cultured in 10cm plates non-stimulated or stimulated with recombinant human Wnt5a protein (645-WN, R&D Systems, 200ng/mL) for 15min using the Cdc42 Pull-down Activation Assay Biochem

Kit (Cytoskeleton) as described by the manufacturer's protocol. Briefly, after stimulation, cells were washed with ice cold PBS, scrapped and lysed in lysis buffer containing protease and phosphatase inhibitors. After lysate clarification, inputs from all the samples were gathered and the remaining lysate was used for the pulldown reaction. 10µg of PAK-PBD beads were added to equivalent protein amounts of cell lysates (300µg) for each condition. The mixture was then incubated for 1h at 4ºC with gentle rotation. After the pulldown reaction, beads were washed 3 times in washing buffer and the bound protein complexes were eluted in sample buffer with DTT by placing the beads for 5min at 95ºC. Samples were then blotted on SDS-PAGE following standard protocols.

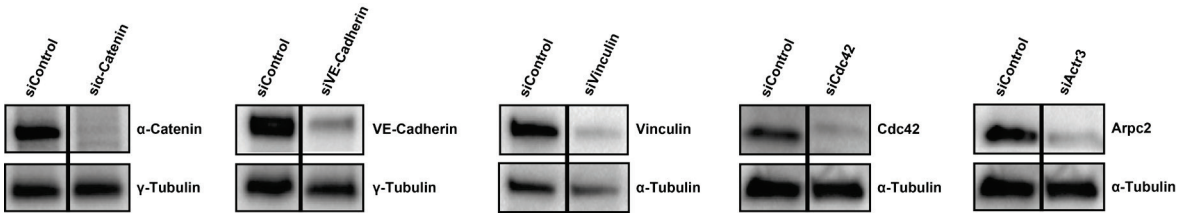

Figure 14. Western blot showing siRNA knockdown efficiency. Western blot showing siRNA knockdown efficiency for α-Catenin (n= 2), VE-cadherin (n= 2), vinculin (n= 1), Cdc42 (n= 1) and Actr3 (n=1).

III.13. Immunoprecipitation

VE-cadherin and vinculin immunoprecipitation was performed from HUVECs cultured in 10cm plates. After the wound-healing assay (described in III.5), cells were incubated with PBS supplemented with 1mM $CaCl_2$ and 0.5mM DSP (#22585, Thermo Scientific) for 20min at RT. Afterwards they were washed twice with ice cold PBS and then four times with ice cold quenching buffer (10mM Tris/HCl, pH 7.5, in PBS). Then, cells were scrapped and lysed in lysis buffer (25mM Tris/HCl, pH 7.5, 1% NP-40, 1% deoxycholic acid, 150mM NaCl) containing protease and phosphatase inhibitors. Cell lysates were centrifuged at 16,100g for 10min at 4ºC and the pellet digested in SDS IP buffer (15mM Tris/HCl, pH 7.5, 5mM EDTA, 2.5mM EGTA, 1% SDS). Samples were then incubated for 10min at 100ºC and diluted in lysis buffer. At this point, inputs from all the samples were gathered and the remaining lysate was used for immunoprecipitation. Pre-washed Pierce® G-protein agarose beads (#22851, Thermo Scientific) were added to equivalent protein amounts of cell lysates (100-200µg) for each condition, containing

either 2µg of anti-vinculin (V9264, Sigma-Aldrich) or anti-VE-cadherin (sc-9989, Santa Cruz Biotechnologies) antibody. The mixture was then incubated overnight at 4ºC with gentle rotation. After immunoprecipitation, beads were washed 4 times in ice cold lysis buffer and the bound protein complexes were eluted in sample buffer with DTT by placing the beads for 10min at 100ºC. Samples were then blotted on SDS-PAGE following standard protocols.

III.14. Immunofluorescence

For immunofluorescence of *in vitro* cultured HUVECs, cells seeded on 24-well plates with glass coverslips, or 8-well Ibidi slides (80826, Ibidi) previously coated with 0.2% Gelatin in sterile water (G1393, Sigma-Aldrich) or with Fibronectin in PBS (F1141, Sigma-Aldrich), respectively.

After the wound-healing assay (described in III.5), HUVECs were fixed in 1% Paraformaldehyde (PFA) supplemented with 1M $MgCl_2$ and 1M $CaCl_2$ (1µL/2mL) in PBS for 30min at RT. Cells were then washed with PBS to remove the remaining PFA and the immunostaining protocol initiated.

When the PBS was removed, HUVECs were blocked and permeabilized with blocking solution containing 3% BSA in PBS-T (PBS with 0.1% Triton X-100) for 30min at RT. Then cells were incubated for 2h at RT with the primary antibodies diluted in the blocking solution (see Table 5) and washed 3 times for 15min in PBS-T. Afterwards, cells were incubated in blocking solution containing the secondary fluorophore conjugated antibodies for 1h at RT in the dark (see Table 6), followed again by 3 washes of 15min in PBS-T. Finally, HUVECs were incubated with 1x DAPI (D1306, Molecular Probes by Life Technologies) diluted in PBS-T for 5min in the dark. Coverslips were then mounted on microscopy glass slides using Mowiol DABCO (Sigma-Aldrich), while for the 8-well Ibidi slides 50µL of Mowiol DABCO was added to each well.

To quantify co-localization of junctional molecules, high-resolution Z-stack images at multiple positions on the wound edge were acquired on a confocal Laser Point-Scanning Microscope 880 (Zeiss) equipped with the Zen black software with a Plan Apochromat 63x NA 1.40 oil DIC M27 objective. For polarity quantification, a tile-scan spanning the entire region of the wound was acquired on a motorized inverted

widefield fluorescence microscope, Zeiss Axiovert 200M (Carl Zeiss) equipped with the Metamorph software with an EC Plan-NeoFluar 40x NA 0.75 dry objective.

Table 5. List of primary antibodies used.

Name	Vendor	Cat No	Host	IF	WB
Anti-ARPC2	Merck Millipore	07-227	Rabbit	1/100	–
Anti-ARP3	Abcam	ab181164	Rabbit	–	1/1000
Anti-CD102	BD Biosciences	553326	Rat	1/200	–
Anti-Cdc42	Cell Signaling	2466	Rabbit	–	1/1000
Anti-ERG	Abcam	ab92513	Rabbit	1/200	–
Anti-GOLPH4	Abcam	ab28049	Rabbit	1/400	–
Anti-HA tag	BioLegend	901513	Mouse	1/100	–
Anti-p120-Catenin	Merck Millipore	05-1567	Mouse	1/100	–
Anti-V5 tag	Invitrogen	R960-25	Mouse	1/100	–
Anti-VE-cadherin	Santa Cruz Biotechnologies	sc-6458	Goat	1/100	1/1000
Anti-VE-cadherin	Santa Cruz Biotechnologies	sc-9989	Mouse	1/100	–
Anti-VE-cadherin	R&D Systems	AF938	Goat	1/100	1/400
Anti-Vinculin	Sigma-Aldrich	V9264	Mouse	1/400	1/1000
Anti-Vinculin	Sigma-Aldrich	V4139	Rabbit	1/100	1/1000
Anti-ZO-1	Invitrogen	402300	Rabbit	1/100	–
Anti-α18	Gift	–	Rat	1/20000	–
Anti-α-catenin	Sigma-Aldrich	C2081	Rabbit	1/200	1/1000
Anti-α-Tubulin	Sigma-Aldrich	T6199	Mouse	1/200	1/2000
Anti-β-catenin	Sigma-Aldrich	C2206	Rabbit	1/100	1/1000

Table 6. List of secondary antibodies used.

Name	Vendor	Cat No	Host	IF	WB
AffiniPureF(ab')$_2$ fragments Donkey anti-rabbit IgG	Jackson Immunoresearch	711-006-152	–	1/400	–
Donkey anti-Goat Alexa 647	Thermo Fisher Scientific	A21447	Donkey	1/400	–
Donkey anti-Goat HRP	Bethyl	A50-201P	Donkey	–	1/5000
Donkey anti-Mouse Alexa 488	Thermo Fisher Scientific	A21202	Donkey	1/400	–
Donkey anti-Rabbit Alexa 488	Thermo Fisher Scientific	A21206	Donkey	1/400	–
Donkey anti-Rabbit Alexa 568	Thermo Fisher Scientific	A10042	Donkey	1/400	–
Donkey anti-Rabbit Alexa 647	Thermo Fisher Scientific	A21447	Donkey	1/400	–
Goat anti-Rabbit HRP	Life Technologies	G-21234	Goat	–	1/5000

Goat anti-Rat Alexa 555	Thermo Fisher Scientific	A21434	Goat	1/400	–
Phalloidin 488	Thermo Fisher Scientific	A12379	–	1/400	–
Phalloidin 568	Thermo Fisher Scientific	A12380	–	1/200	–
Sheep anti-Mouse HRP	GE Healthcare	NA931V	Sheep	–	1/5000

III.15. Proximity Ligation Assay (PLA)

Confluent HUVECs seeded on 24-well plates were subjected to the wound-healing assay (described in III.5) and then processed for PLA using the Duolink® In Situ Red Mouse/Rabbit Starter Kit (DUO92101-1KT, Sigma-Aldrich) as described by the manufacturer's protocol. To probe interactions between vinculin and VE-cadherin, cells were incubated with an anti-vinculin antibody raised in rabbit (V4139, Sigma-Aldrich) and an anti-VE-cadherin antibody raised in mouse (sc-9989, Santa Cruz Biotechnologies). In parallel, cells were also incubated with an anti-VE-cadherin antibody raised in goat (AF938, R&D Systems) and subsequently with an anti-Goat fluorescent-conjugated secondary antibody (A21447, Thermo Fisher Scientific) to label adherens junctions. To quantify co-localization of PLA signal at adherens junctions, high-resolution Z-stack images at multiple positions on the wound edge were acquired on a confocal Laser Point-Scanning Microscope 880 (Zeiss) equipped with the Zen black software with a Plan Apochromat 63x NA 1.40 oil DIC M27 objective. Briefly, PLA dots were quantified only at adherens junctions, using a similar approach to the co-localization analysis (described in III.18), using VE-cadherin immunofluorescence staining signal to detect overlapping pixels between junctions and PLA signals.

III.16. Calcium switch

Confluent HUVECs seeded on 24-well plates were subjected to the wound-healing assay (described in III.5) and then incubated for 15min in Ca^{2+} free HBSS, followed by DMEM (#41966-029, Gibco) supplemented with 1% Penicillin/Streptomycin (#15140122, Gibco), 10% fetal bovine serum (FBS) (#10500-064, Gibco) and 2mM Ca^{2+} from 1 up to 30min at 37ºC, 5% CO_2. Afterwards, cells were immediately fixed in

1% Paraformaldehyde (PFA) supplemented with 1M $MgCl_2$ and 1M $CaCl_2$ (1µL/2mL) and processed for immunostaining.

III.17. Calcium imaging with FURA-2AM

Confluent HUVECs seeded on 8-well Ibidi slides were subjected to the wound-healing assay and then loaded with 5mM FURA-2 AM (F1221, Life Technologies), which was previously sonicated for 15min in a water bath to improve cell uptake, for 40min before the recordings. Intracellular calcium activity was monitored at the wound edge for 20min by imaging cells at 340nm and 380nm. The ratio 340/380 was used to calculate intracellular calcium levels in individual cells for the entire time span of the experiment. Basal calcium levels, peak activation, number of cells producing calcium peaks and the number of peaks were then quantified.

III.18. Polarity index calculation

To quantify cell polarity, tile-scan images of HUVECs stained with Golgi (Golph4) and nuclear (DAPI) markers were processed on Adobe Photoshop to separate leader cells, identified as the first row of cell directly in contact with the wound edge, from follower cells, comprising the second to fourth rows of cells away from the wound edge. Afterwards, each set of images was imported and analyzed in MATLAB using a modified version of a polarity analysis script kindly provided by Anne-Clémence Vion and Holger Gerhardt. Briefly, after segmenting each channel corresponding to the Golgi and nuclear staining, the centroid of each organelle was determined and a vector connecting the center of the nucleus to the center of its corresponding Golgi apparatus was drawn. The Golgi-nucleus assignment was done automatically minimizing the distance between all the possible couples. The polarity of each cell was defined as the angle between the vector and the scratch line. A polar histogram showing the angle distribution was then generated. Circular statistic was performed using Circular Statistic Toolbox (Berens, 2009). To test for circular uniformity, we applied the Rayleigh test, yielding a p-value indicating the likelihood of the distribution to be uniformly distributed around the circle.

The polarity index (PI) was calculated as the length of mean resultant vector for a given angular distribution:

$$\mathrm{PI} = \sqrt{\left(\frac{1}{\mathrm{N}}\sum_{1}^{\mathrm{N}}\cos\alpha\right)^{2} + \left(\frac{1}{\mathrm{N}}\sum_{1}^{\mathrm{N}}\sin\alpha\right)^{2}}$$

It varies between 0 and +1, with 0 corresponding to random distribution, meaning weakly polarized, and +1 corresponding to targeted distribution, meaning strongly polarized. PI indicates the collective orientation strength of the cell monolayer.
To calculate the PI as a function of distance, each image was divided starting from the wound edge in slices 50μm apart. The cell polarity within each slice was extracted and represented as angular histogram and the corresponding PI was calculated. For Fig.16A, a global polarity index was calculated merging together the results from different images from the same experimental conditions.

III.19. Co-localization analysis

For co-localization analysis, high-resolution Z-stack confocal images of HUVECs stained for junctional proteins (VE-cadherin, vinculin, α-catenin, β-catenin and p120-catenin) were imported and analyzed in Matlab using custom written code. An object-based co-localization approach was used. Briefly, each channel was segmented and a binary mask was generating. The masks were combined and the fraction of pixels with overlapping signals was quantified.

III.20. Statistical analysis

All statistical analysis was performed using GraphPad Prism 7 and Matlab (Mathworks). Statistical details of experiments are reported in the figures and figure legends. Sample size is reported in the figure legends. Comparisons between two experimental groups were analyzed with unpaired parametric t test, while multiple comparisons between more than two experimental groups were assessed with one-way ANOVA. We considered a result significant when $p < 0.05$.

Chapter IV. Results

IV.1. Wnt5a regulates endothelial collective cell polarization and migration

Author contribution

The author of this thesis performed all the experiments described in the following section, with the exception of the cryptic lamellipodia experiments that were done together with Catarina Fonseca, MSc. The Matlab scripts used to calculate the polarity index were developed by Anna Pezzarossa, PhD. The PIV analysis was performed by Anna Pezzarossa, PhD.

In order to confirm the preliminary data indicating that Wnt5a regulates collective EC migration *in vitro*, we used the wound-healing assay and scratched a confluent monolayer of HUVECs to assess directed collective EC migration in control, Wnt5a- and α-catenin (Ctnna1)-depleted cells. Cells were stained with Hoechst and allowed to migrate for 10-16h, while images of the wound edge were acquired in multiple positions every 10min (Figure 15A). First, we observed that collectively, α-catenin- and Wnt5a-depleted cells have a tendency to migrate more randomly compared to control cells (Figure 14B). The correlation length calculated from particle image velocimetry (PIV) analysis (Petitjean *et al*., 2010), confirmed loss of coordination in Wnt5a- and α-catenin-depleted cells (Figure 15C). Then, by analyzing a subset of cells from each population we observed that Wnt5a-depleted cells migrated in a more tortuous manner, albeit slightly faster than control cells, and as a result were less capable of closing the wound inflicted, which was in agreement with the preliminary data previously obtained (Figure 15D). Since non-canonical Wnt signaling has been associated with tissue polarity regulation (Niehrs *et al*., 2012) and cells lacking Wnt5a are less capable of migrating to close the inflicted wound, we wondered whether the lack of Wnt5a, would affect EC ability to break symmetry and polarize correctly, thus impairing their directed migration capability. To test this hypothesis *in vitro*, we used the wound-healing assay and allowed cells to migrate for 5h before fixation and immunostained for Golgi and nuclear markers. Since we showed that ECs position the Golgi apparatus in front of the nucleus toward the direction of migration *in vivo* (Franco *et al*., 2015), we considered nucleus-Golgi axial polarity (given by a vector drawn from the center of the cell nucleus to the center of the Golgi apparatus) as a readout of

individual cell front-rear polarity. The polarity of each cell relative to the wound edge was calculated subsequently by measuring the angle (α) between the wound edge and the axial polarity vector (Figure 16A). To easily analyze collective cell polarization, we defined a polarity index (PI) (see III.18), ranging from 0 to 1, where 1 depicts a strong polarization and 0 indicates random polarization (Figure 16B).

Calculation of PI from the leading edge towards the monolayer highlighted coordination of cell polarities up to 300-350µm in control cells (Figure 17A). To validate this approach, we used siRNA against α-catenin, a crucial component of adherens junctions and indispensable for collective cell migration (Bazellieres *et al.*, 2015). As expected, knockdown (KD) of α-catenin led to poor collective coordination

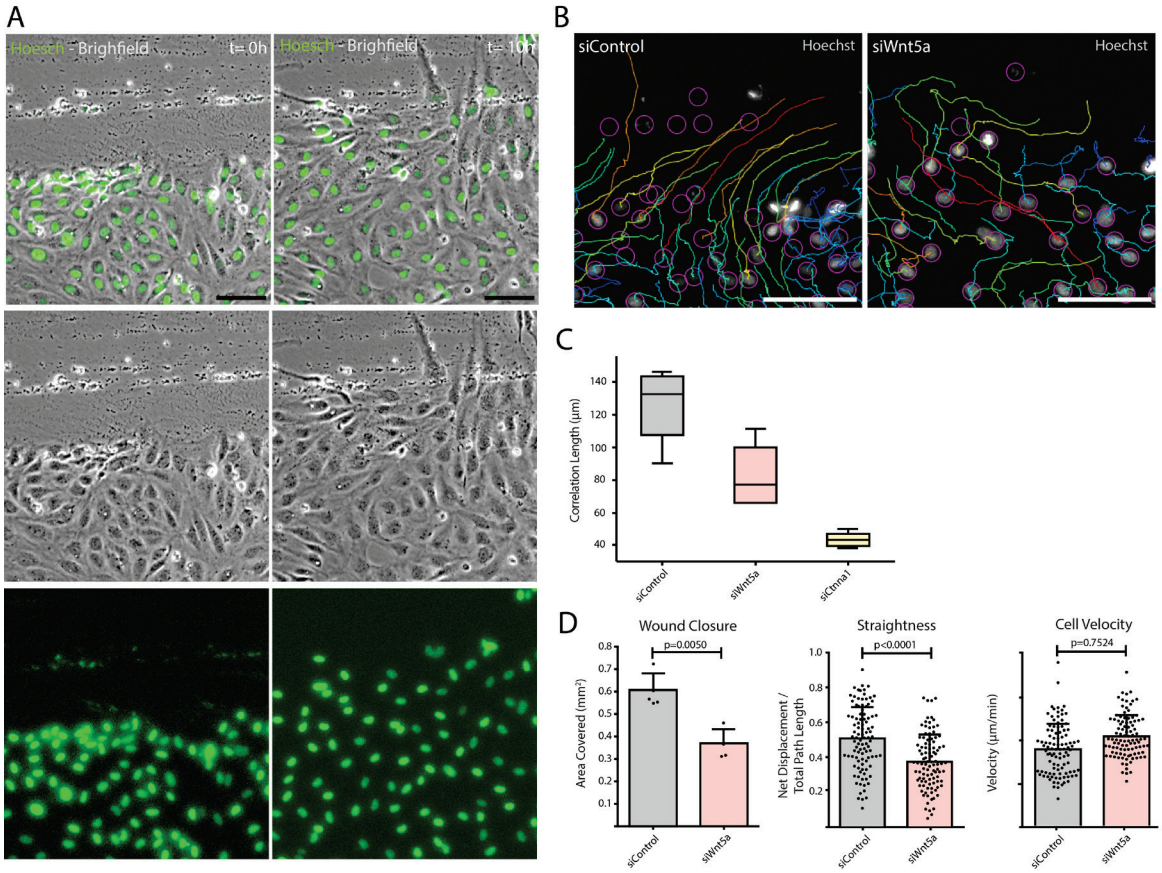

Figure 15. Wnt5a regulates endothelial collective cell migration.

(A) Phase contrast images from the wound edge of migrating HUVEC monolayer labeled for nuclei (Hoechst) at t=0h and 10h. Scale bar, 100µm.

(B) Wound edge of siControl (left) and siWnt5a (right) transfected cells showing individual cell trajectories within the monolayer. Circles indicate cell nuclei. Scale bar, 50µm

(C) Correlation length box plots from siControl (n=6), siWnt5a (n=8) and siCtnna1 (n=3).

(D) Quantification of wound closure, straightness and cell velocity over the course of 16h migration in siControl (n_{cells}=100; 4 fields of view) and siWnt5a (n_{cells}=100; 4 fields of view) transfected cells. Data are mean ± SD, p-values from unpaired t test (n=2).

demonstrated by low PI values along the monolayer. Deviations from the theoretical random (PI=0) reflect a polarity bias introduced by the empty wound space, which was used as a reference value for the experimental random in the system and set the threshold for uncoordinated migration (Fig.17A) at PI=0.10±0.04. We established this PI threshold by determining the mean +/- SD of the results obtained from the siCTNNA1 experiments across the monolayer. For the calculation of the mean value, we excluded the first row of cells, as these were strongly affected by wound monolayer asymmetry, leading to a stronger polarity towards the wound.

Remarkably, Wnt5a-deficient cells showed randomized polarity starting at 150-200µm from the leading edge, suggesting a dramatic loss of coordination of collective behavior (Figure 17A). To understand whether the polarity response of leaders and followers were equally affected, we measured the PI for leaders (1st row of cells) and followers (2nd-5th row of cells) separately. Interestingly, leader cells polarized strongly towards the wound edge in both control (PI=0.638) and siα-catenin (PI=0.358), however the polarity of siα-catenin follower cells was randomized (PI=0.101), while control cells showed strong forward polarization (PI=0.345). siWnt5a leader cells also showed robust polarization towards the wound edge (PI=0.493). However, follower cells showed a strong randomization of collective cell polarity (PI=0.104) when compared to control cells, similarly to α-catenin KD cells (Figure 17B).

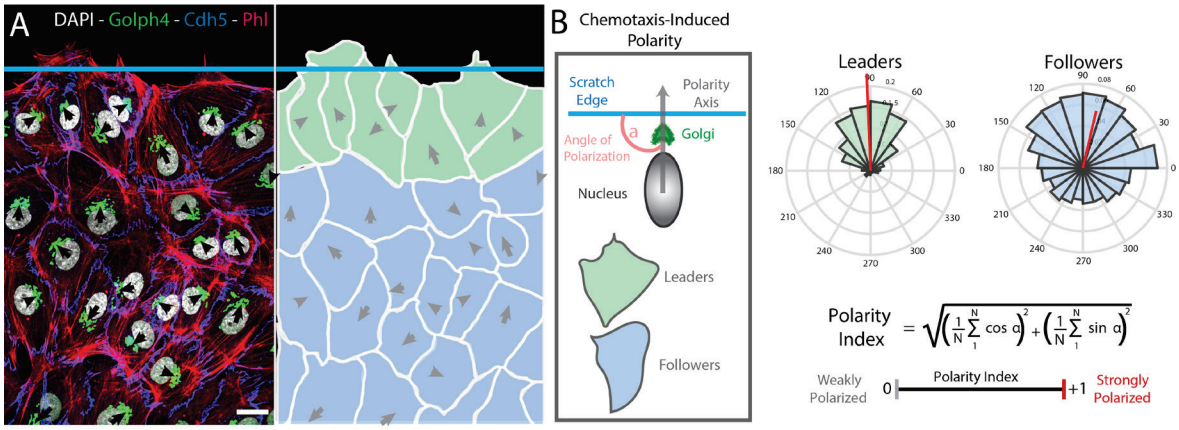

Figure 16. Chemotaxis-induced front-rear cell polarity readout.

(A) Wound edge of migrating HUVEC monolayer labeled for nuclei (DAPI), Golgi (Golph4), actin (phalloidin) and VE-cadherin (Cdh5) (left) and the corresponding image segmentation with leader cells in green, follower cells in blue and axial polarity vectors in gray (right). Scale bar, 20µm

(B) Chemotaxis-induced polarity was determined as the angle of polarization (α) between the scratch edge and the cell polarity axis defined by a vector drawn from the center of the cell nucleus to the center of the Golgi apparatus. Collective polarization was calculated with the polarity index (PI) (see III.18).

Remarkably, the same randomized polarity was observed in ECs lacking Wnt5a using the orientation of the cryptic lamellipodia (Farooqui and Fenteany, 2005) instead of the Golgi apparatus as a reference for EC axial polarity (Figure 17C–E). Therefore, these data demonstrate that in spite of not being essential for individual cell polarity, Wnt5a seems to be essential for coordinating EC behavior.

Taken together, these results suggest first that Wnt5a is not essential for single cell polarity, as leader cells lacking Wnt5a retain their ability to polarize towards the wound. And second that Wnt5a is necessary for EC behavior coordination, since

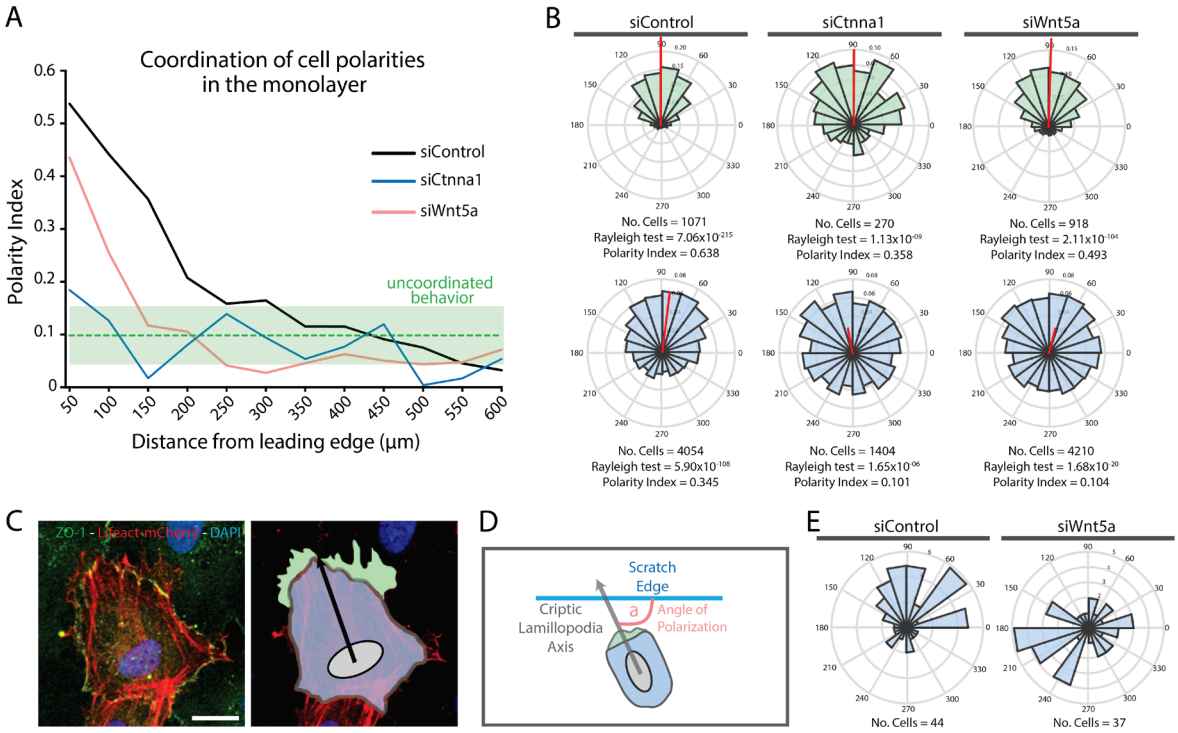

Figure 17. Wnt5a is crucial for coordinating endothelial cell collective behavior.

(A) Polarity index (PI) as function of the distance from the leading edge (µm) in HUVEC monolayers of siControl (black, n=9), siWnt5a (blue, n=10) and siCtnna1 (red, n=4) transfected cells.

(B) Angular histograms showing the polarity distributions of leaders (green) and followers (blue) from siControl (n=6), siWnt5a (n=8) and siCtnna1 (n=3) transfected cells. Area under each bin: number of cells polarized in that direction. p-values from Rayleigh test.

(C) Example of Lifeact-mCherry+ HUVEC extending cryptic lamellipodia under an adjacent cell labeled for nuclei (DAPI), tight junctions (ZO-1) and actin (Lifeact-mCherry) (left) and the corresponding image segmentation with the cryptic lamellipodia in green, the cell body in blue and the axial polarity vector in black (right). Scale bar, 20µm.

(D) Cryptic lamellipodia axial polarity at the wound edge of migrating HUVECs was determined by calculating the angle of polarization (α) between the scratch edge and the polarity axis defined by a vector drawn from the center of the cell nucleus to the center of the cryptic lamellipodia.

(E) Angular histograms showing the polarity distributions of cryptic lamellipodia of Lifeact-mCherry+ cells from siControl (n=4) and siWnt5a (n=4) transfected cells. Area under each bin: number of cells polarized in that direction. p-values from Rayleigh test.

Wnt5a-depleted follower cells are not able to polarize preferentially towards the wound edge. Therefore, these results clearly suggest that Wnt5a plays a pivotal role in regulating EC collective polarity and behavior *in vitro*.

IV.2. Local endogenous Wnt5a expression is able to rescue randomized cell polarity

Author contribution

The author of this thesis performed all the experiments described in the following section. Lentiviral plasmids containing protein fusion sequences were produced by Catarina Fonseca, MSc.

In order to confirm the specific influence of Wnt5a in regulating collective cell polarity, we attempted to rescue the randomized polarity phenotype of follower cells using two distinct strategies: one where Wnt5a was delivered exogenously, via a recombinant protein added to the culture media and another where Wnt5a was directly expressed by HUVECs, via lentivirus transduction. Exogenous delivery of Wnt5a failed to restore follower cell polarity in Wnt5a-depleted cells (PI=0.147), while Wnt5a-V5 was able to rescue the polarity defects observed in cells lacking Wnt5a (PI=0.219) (Figure 18). Thus, taken together these results indicate that collective cell polarity seems to rely on

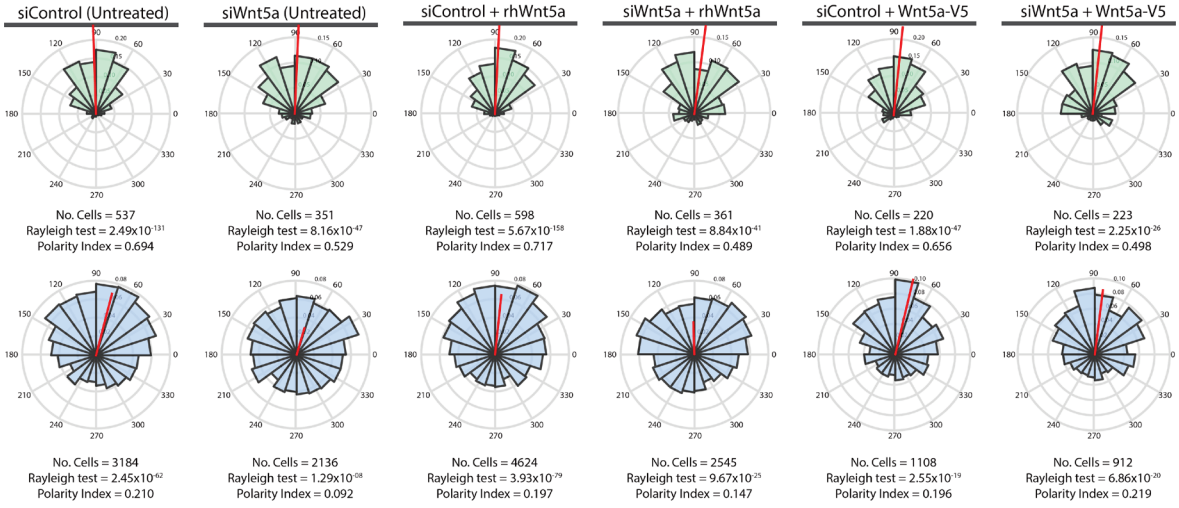

Figure 18. Endothelial collective cell polarity relies on local Wnt5a signaling.

Angular histograms showing the polarity distributions of leaders (green) and followers (blue) from siControl and siWnt5a transfected cells untreated (n=4) or treated with either exogenous (n=5) or endogenous Wnt5a (n=2). Area under each bin: number of cells polarized in that direction. p-values from Rayleigh test.

local Wnt5a signaling, regulated spatially at the single cell level.

IV.3. Wnt5a regulates adherens junctions' organization

Author contribution

The author of this thesis performed all the experiments described in the following section. Western blot experiments were performed independently by the thesis author and Isabela Fortunato, MSc. The Matlab scripts used to measure protein co-localization were developed by Anna Pezzarossa, PhD.

Adherens junctions are the key mediators of collective cell migration (Tambe *et al.*, 2011). Thus, we decided to analyze in detail the morphology, organization and expression patterns of key molecules composing the adherens junction complex in control and Wnt5a KD cells. In migrating cells, cell-cell adhesion contacts come in different flavors: linear, reticular or discontinuous junctions also called focal adhesion junctions (Fernández-Martin *et al.*, 2012; Huveneers *et al.*, 2012). Interestingly, Wnt5a-deficient cells showed a significant decrease in discontinuous (linked to high-force) and a concomitant increase in reticular junctions (linked to low-force), when compared to control cells (Figure 19A, B).

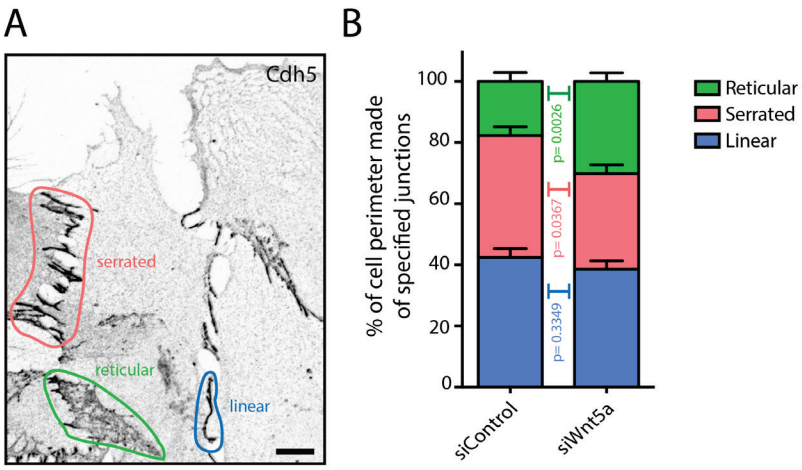

Figure 19. Wnt5a signaling influences adherens junction's morphology.

(A) HUVECs labeled for adherens junctions (VE-Cadherin), showing distinct junctions' morphologies: linear (blue), discontinuous (red) and reticular (green). Scale bar, 10µm.

(B) Quantification of cell perimeter (%) composed of linear (blue), discontinuous (red) and reticular (green) junctions in siControl (n_{cells}=62) and siWnt5a (n_{cells}=65) transfected cells. Data are mean ± SD, p-values from unpaired t test (n=4-6).

Although protein expression levels of junctional proteins VE-cadherin, β-catenin, α-catenin and vinculin were identical in control and Wnt5a-deficient cells (Figure 20A, B), co-localization studies identified a specific downregulation of vinculin binding to the cytoplasmic tail of VE-cadherin (Figure 21A, B). Vinculin binds to α-catenin when the former is on open conformation (le Duc *et al*., 2010; Yao *et al*., 2014; Yonemura *et al*., 2010). We used a specific antibody that recognizes open α-catenin (α18 antibody) (Yonemura *et al*., 2010) to test whether the impaired vinculin co-localization arises from defective α-catenin opening or from a specific inability to recruit vinculin. α18 antibody/VE-cadherin co-localization showed a mild but significant decrease in Wnt5a-depleted cells. Yet, vinculin/α18 antibody co-localization was strongly decreased in Wnt5a KD cells (Figure 21C). Therefore, altogether these results indicate that Wnt5a is important to recruit and/or stabilize vinculin binding to α-catenin at adherens junctions.

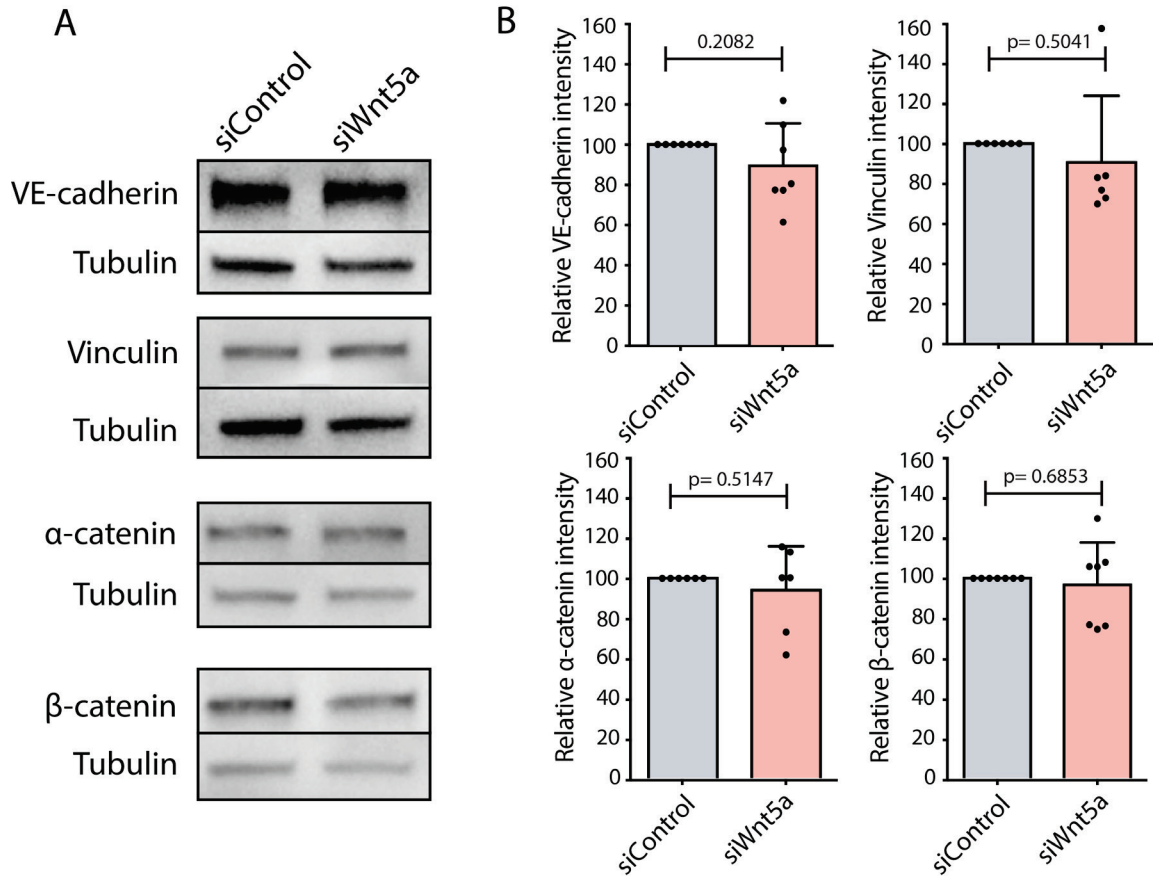

Figure 20. Lack of Wnt5a does not affect the expression levels of junctional proteins.

(A) Western blot assessing junctional protein levels – VE-Cadherin, Vinculin, α-catenin and β-catenin – in siControl and siWnt5a transfected cells (n=5).

(B) Quantification of relative intensity normalized to Tubulin. Data are mean ± SD, p-values from unpaired t test.

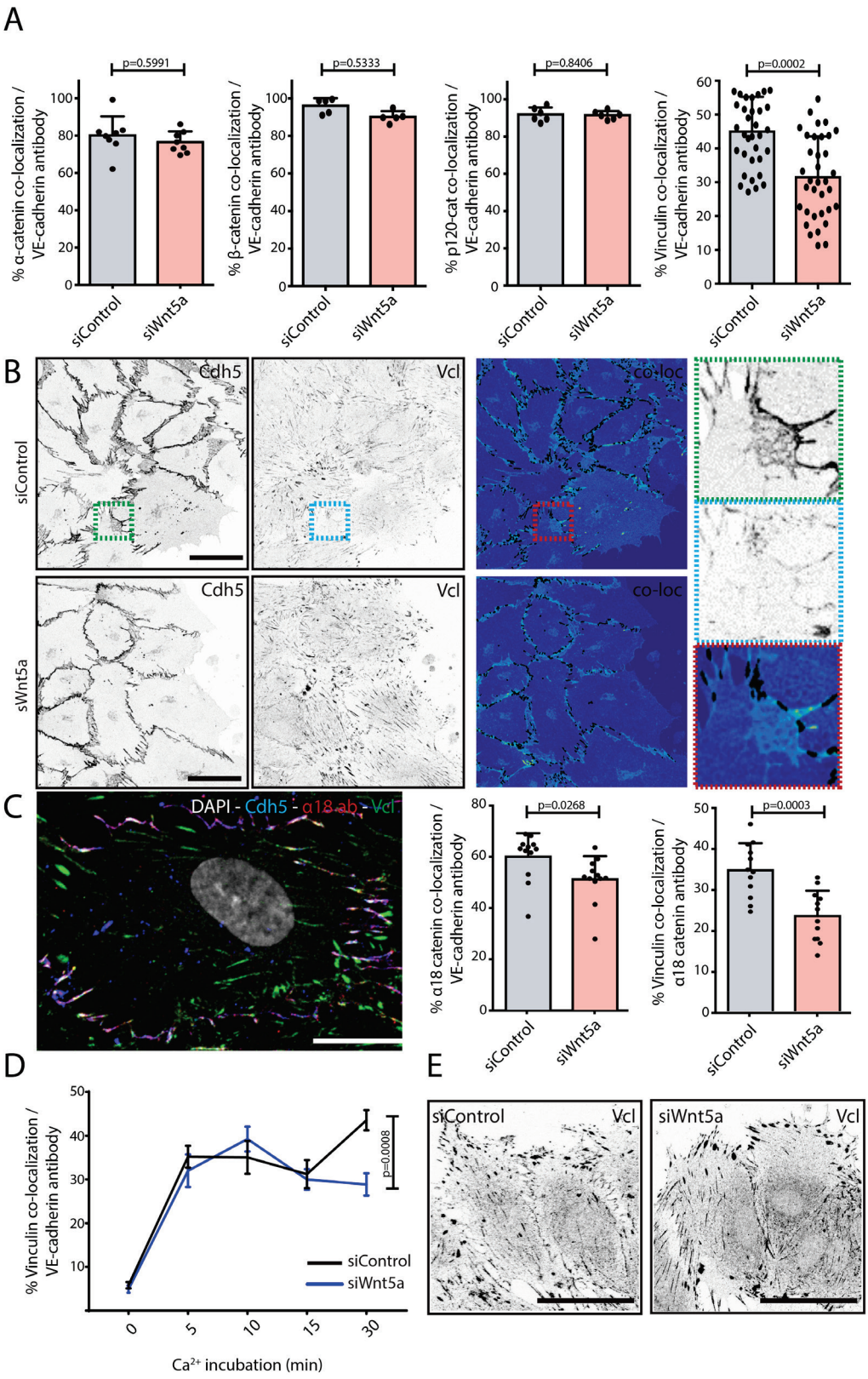

Figure 21. Wnt5a is necessary for long-term association of vinculin to adherens junctions.

(A) Co-localization (%) between α-catenin/VE-cadherin (n=3), β-catenin/VE-cadherin (n=3), p120-catenin/VE-cadherin (n=2) and vinculin/VE-cadherin (n=6) in siControl and siWnt5a transfected cells. Data are mean ± SD, p-values from unpaired t test.

Figure 21 continues on next page

Figure 21 continued

(B) Example of wound edge of migrating HUVEC monolayer labeled for VE-cadherin and vinculin used for co-localization analysis in siControl (top left) and siWnt5a (bottom left) transfected cells and the corresponding image segmentation showing the co-localizing pixels between both stainings in black (top and bottom right). Green (top right), blue (middle right) and red (bottom right) squares show a higher magnification of a junction where VE-cadherin and vinculin co-localize. Scale bar, 40µm.

(C) HUVEC labeled for nuclei (DAPI), VE-Cadherin (Cdh5), α18 catenin and vinculin (left). Co-localization (%) between α18 catenin/VE- cadherin (n=3) and vinculin/α18 catenin (n=3) in siControl and siWnt5a transfected cells (right). Data are mean ± SD, p-values from unpaired t test. Scale bar, 20µm.

(D) Co-localization (%) between vinculin/VE-cadherin as function of calcium incubation time (min) after the calcium switch in HUVECs monolayers of siControl (black) and siWnt5a (blue) transfected cells. Data are mean ± SEM, p-values from unpaired t test (n=2-3).

(E) HUVECs labeled for vinculin (Vcl) showing focal adhesions at the wound edge in siControl and siWnt5a transfected cells. Scale bar, 40µm.

To test whether the reduced vinculin/VE-cadherin and vinculin/α18 co-localization was due to a defect in recruitment or long-term stabilization of vinculin to the adherens junction complex, we performed a calcium switch assay. Interestingly, we did not observe significant differences in the first 15min following junction re-assembly. However, 30min after the switch, Wnt5a KD cells started to display lower vinculin/VE-cadherin co-localization values compared to control cells, suggesting that Wnt5a is not required for vinculin recruitment to the junctions, but it is necessary for its long-term

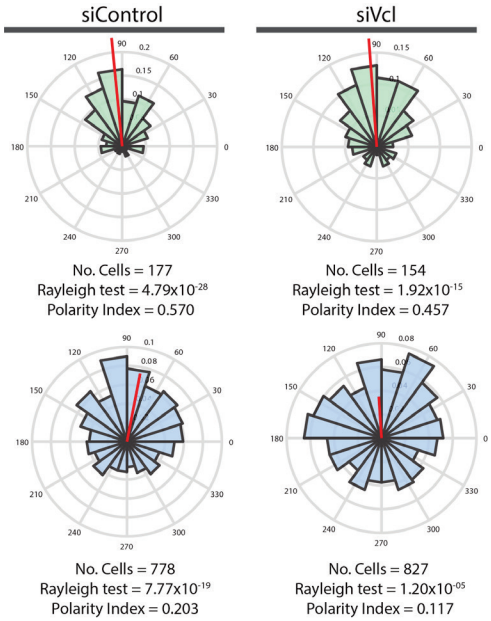

Figure 22. Vinculin is required for endothelial collective cell polarity.

Angular histograms showing the polarity distributions of leaders (green) and followers (blue) from siControl (n=2) and siVcl (n=2) transfected cells. Area under each bin: number of cells polarized in that direction. p-values from Rayleigh test.

association at cell junctions (Figure 21D).

Notably, this reduced association of vinculin to adherens junctions was accompanied by an apparent increase at focal adhesions, which were larger compared to those formed on control cells (Figure 21E), reinforcing the idea that Wnt5a is required for vinculin association to the cell junctions.

Finally, to confirm that vinculin association at adherens junctions is indeed essential for collective cell behavior, we KD vinculin with siRNA and analyzed its effects on cell polarity. As expected, vinculin-depleted follower cells completely phenocopied the polarity defects previously observed in Wnt5a KD follower cells (PI=0.117), highlighting the importance of vinculin stabilization at cell junctions (Figure 22).

Altogether, these results indicate that Wnt5a is important to stabilize vinculin binding to α-catenin in adherens junctions, in order to generate high-force junctions, which is essential for collective cell behavior.

IV.4. Wnt5a strengthens adherens junctions and enhances cell-cell force transmission

Author contribution

The author of this thesis performed all the experiments described in the following section, with the exception of the AFM experiments that were done in collaboration with Dra. Maria Filomena Aréde de Carvalho and the FRET experiments that were done by Catarina Fonseca, MSc. FRET analysis was performed by Anna Pezzarossa, PhD.

Vinculin binds to high-force adherens junctions (Huveneers *et al.*, 2012), and intercellular junctions are essential for force-dependent collective cell migration (Tambe *et al.*, 2011). Depletion of Wnt5a affected both vinculin stabilization and collective cell migration. Thus, we hypothesize that Wnt5a depletion might impact force transmission through adherens junctions. To test this hypothesis, we used atomic force microscopy to probe the force of cell-cell interactions (Figure 23A). Control-control cell interactions required on average $1x10^{-15}$ J of work for complete cell detachment, while Wnt5a KD-Wnt5a KD cell interactions required significant less work ($5x10^{-16}$ J) for complete cell separation. EGTA-treatment, which chelates calcium and

abolishes cadherin-dependent interactions, on control and Wnt5a KD cell interactions significantly reduced the strength of cell interactions, and annulled differences. VE-cadherin depleted cells showed a very similar level of interaction as EGTA-treated cells, confirming that the majority of strong cell-cell interactions are dependent on VE-cadherin homophilic interactions (Figure 23B). To test whether Wnt5a KD cell-cell interactions were able to recover to control levels with increased times of contact between cell pairs, we performed a time-course experiment with increased contact times from 2s up to 60s. As expected, the work required for complete cell detachment increased at higher contact times in both control-control and Wnt5a KD-Wnt5a KD cell pairs. Despite the low number of measurements for cell-cell interactions performed in this assay, and the high variability in work within replicas, there is a net tendency for a lower amount of work in Wnt5a KD-Wnt5a KD cell pairs compared to control-control interactions in all time points. This reinforces the idea that Wnt5a is necessary from strong cell-cell interactions (Figure 23C). Moreover, to confirm that Wnt5a regulates tension in VE-cadherin, we used a set of a previously characterized FRET-based tension sensors (Conway *et al.*, 2013) (Figure 24A). In Wnt5a-depleted cells, VE-cadherin FRET efficiency was significantly higher, implying lower level of tension, when compared to

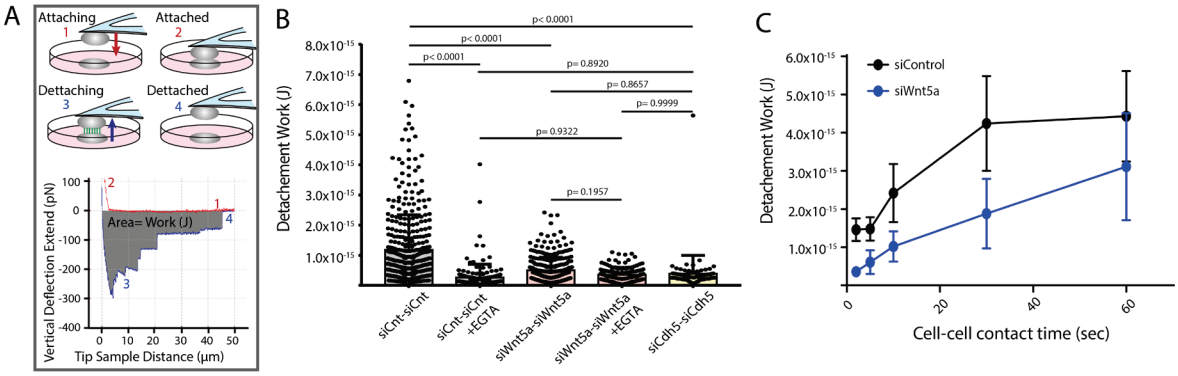

Figure 23. Wnt5a strengthens cell-cell adhesion.

(A) Diagram depicting the 4 steps involved in cell-cell adhesion measurements using atomic force microscopy, as well as its correspondence in the approximation/retraction curve obtained a posteriori: **(1)** Attaching – Cell attached to the tipless cantilever is lowered to make contact with another cell at the bottom; **(2)** Attached – Cells establish cell-cell contact; **(3)** Detaching – The upper cell is pulled in order to break the cell-cell contact previously established; **(4)** Detached – Cells are now fully separated. The gray area in the approximation/retraction curve corresponds to the work (J), which is equivalent to the total amount force necessary to break cell-cell contacts.

(B) Quantification of work detachment (J) in siControl with (n_{curves}=155) or without EGTA (n_{curves}=395), siWnt5a with (n_{curves}=205) or without EGTA (n_{curves}=299) and siCdh5 (n_{curves}=80) transfected cells. Data are mean ± SD, p-values from multiple comparisons in one-way ANOVA. (n=5 for siControl, 6 for siWnt5a and 1 for siCdh5).

(C) Work detachment (J) as function of cell-cell contact time (sec) in siControl (black) and siWnt5a (blue) transfected cell pairs. Data are mean ± SD (n=2).

control cells (Figure 24B, C). Taken together, we showed that Wnt5a signaling promotes tension and reinforces VE-cadherin-dependent cell-cell interactions through adherens junctions.

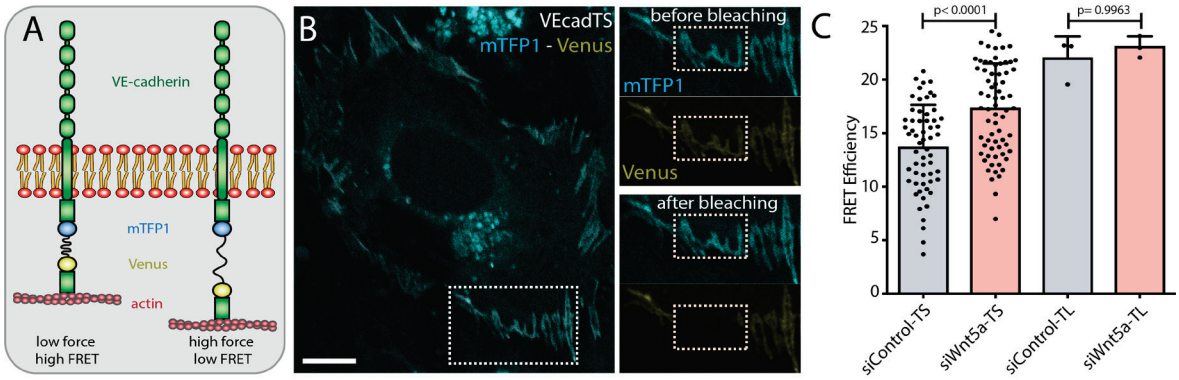

Figure 24. Wnt5a regulates tension at adherens junctions through VE-cadherin.

(A) Diagram showing the molecular structure and mechanism of action of the FRET VE-cadherin tension sensor (VE-Cad TS). The biosensor contains two fluorophores inserted in the cytoplasmic tail of VE-cadherin between the p120-catenin and the β-catenin binding domains – the donor, mTFP1 (blue) and the acceptor, Venus (yellow) – connected by a flagelliform elastic peptide module. When tension is being applied at cell junctions, the elastic module expands and FRET efficiency decreases as the two fluorophores are far apart. On the contrary, when no forces are being applied at the cell junctions, the elastic module contracts and FRET efficiency increases as the two fluorophores are in close proximity. The VE-cadherin tailless sensor (VE-Cad TL) is a negative control sensor that lacks the β-catenin binding domain at the cytoplasmic tail of VE-cadherin.

(B) HUVEC expressing VE-Cad TS undergoing FRET acceptor photobleaching at the adherens junction. Squares show the cell junction before (top) and after photobleaching (bottom). Scale bar, 10μm.

(C) Quantification of FRET efficiency in siControl ($n_{junctions}$=51) and siWnt5a ($n_{junctions}$=69) transfected cells expressing either VE-Cad TS or the tailless biosensor lacking the β-catenin binding-domain, VE-Cad TL ($n_{junctions}$=3 for siControl and siWnt5a). Data are mean ± SD, p-values from unpaired t test. n=6 for TS and n=1 for TL.

IV.5. Forced vinculin binding to α-catenin rescues Wnt5a knockdown phenotype

Author contribution

The author of this thesis performed all the experiments described in the following section. Lentiviral plasmids containing protein fusion sequences were produced by Francisca Vasconcelos, PhD and Isabela Fortunato, MSc.

To test whether decreased force transmission at adherens junctions and defective

collective cell migration on Wnt5a-deficient cells are regulated through vinculin association to the adherens junctions, we overexpressed a fusion protein containing the β-catenin binding domain of α-catenin together with the actin-binding domain of vinculin (αCat-Vinc) (Maddugoda *et al*., 2007) (Figure 25A). As expected, the construct is able to restore randomized cell polarity in vinculin KD cells (PI=0.217) (Figure 27). While αCat-Vinc overexpression in control cells did not significantly affect the overall polarity index of migrating cells (PI=0.232), it completely rescued Wnt5a-deficiency (PI=0.251). Interestingly, overexpression of a control VE-cadherin-α-catenin (VE-cad-αCat) fusion protein (Schulte *et al*., 2011) did not affect neither control (PI=0.260) nor Wnt5a KD polarity indexes (PI=0.117) (Figure 25A, B). Furthermore, overexpression of αCat-Vinc was also sufficient to restore straightness of cell migration in Wnt5a-depleted cells (Figure 25C). To further confirm that vinculin association to adherens junctions is indeed sufficient to restore Wnt5a randomized cell polarity, we overexpressed either a chicken vinculin full-length (Vinc-FL) or a chicken vinculin T12 mutant (Vinc-T12) construct in control and Wnt5a-deficient cells (Figure 26A). Vinc-T12 is a constitutive active form of vinculin containing four amino acid mutations that weaken the affinity of the auto-inhibitory head-to-tail interaction by 100-fold (Cohen *et al*., 2005). As expected, overexpression of both forms of vinculin restored randomized cell polarity in vinculin-depleted cells (PI=0.242 for Vinc-FL; PI=0.207 for Vinc-T12) (Figure 27), while it did not affect overall polarity of control cells (PI=0.229 for Vinc-FL; PI=0.208 for Vinc-T12) (Fig.26B). Interestingly, Vinc-T12 but not Vinc-FL rescued randomized cell polarity of Wnt5a KD cells (PI=0.208 and PI=0.150, respectively) (Fig.26B). Furthermore, overexpression of Vinc-T12 but not Vinc-FL also restored junctions' morphology in Wnt5a KD cells, promoting the formation of discontinuous high-tension junctions in detriment of low-tension reticular junctions (Fig.26C). Altogether, these data suggest that Wnt5a promotes EC behavior coordination by favoring vinculin association to force transmitting adherens junctions.

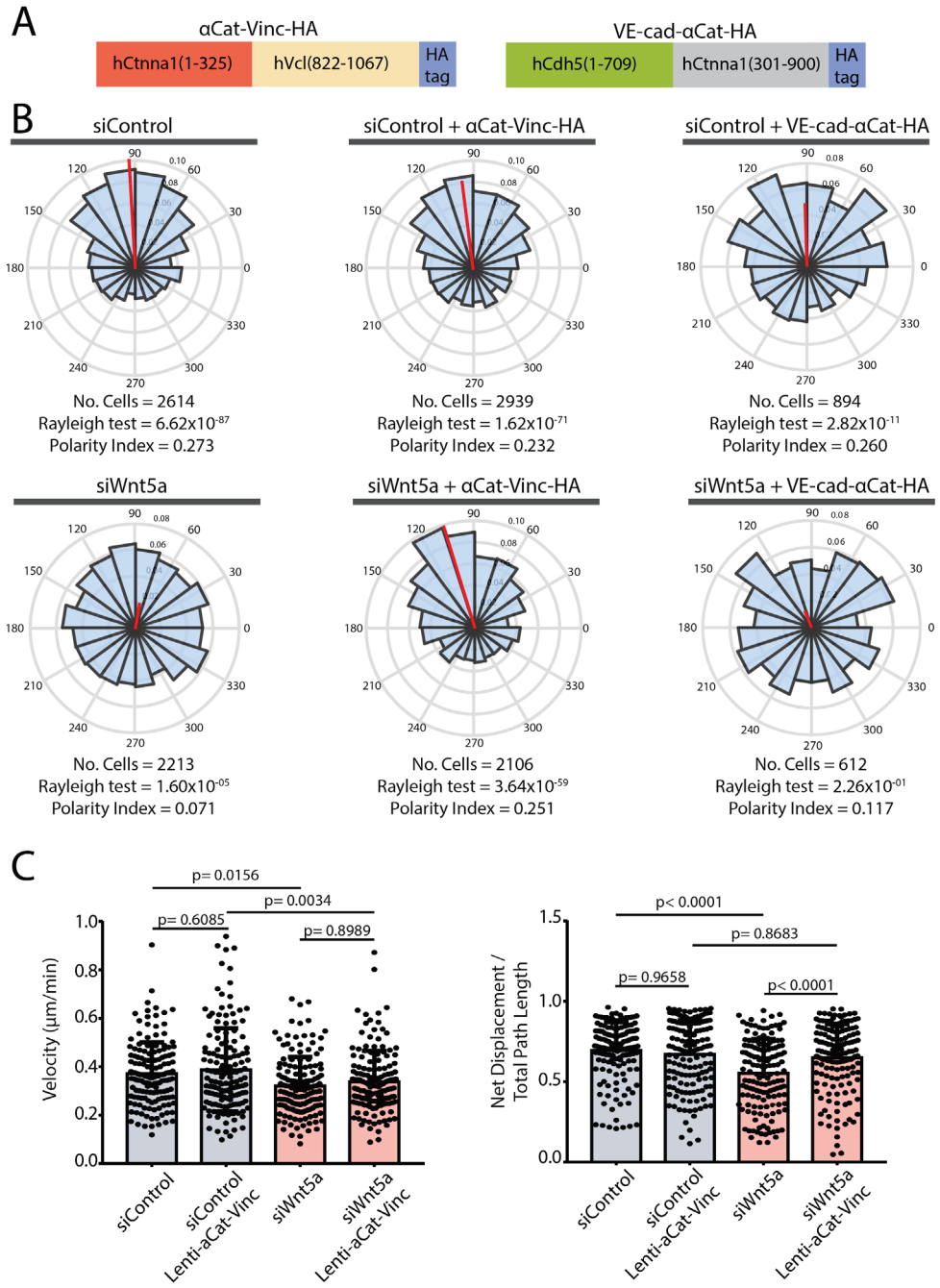

Figure 25. Vinculin association to adherens junctions is able to rescue Wnt5a randomized cell polarity.

(A) Diagram showing the molecular structures of the αCat-Vinc-HA (left) and the VE-cad-αCat-HA (right) constructs. αCat-Vinc-HA is a fusion protein containing the β-catenin binding domain of α-catenin (red) fused with the actin binding domain of vinculin (beige) and the HA tag (blue). VE-cad-αCat-HA is a fusion protein containing the extracellular, transmembranar and proximal intracellular domain of VE-cadherin (green) fused with the actin/vinculin binding domain of α-catenin (gray) and the HA tag (blue).

(B) Angular histograms showing the polarity distributions of siControl and siWnt5a transfected cells non-infected (n=6) or infected with either αCat-Vinc-HA (n=6) or VE-cad-αCat-HA (n=2). Area under each bin: number of cells polarized in that direction. p-values from Rayleigh test.

(C) Quantification of cell velocity and straightness over the course of 16h migration in siControl and siWnt5a transfected cells non-infected (n_{cells}=150) or expressing αCat-Vinc (n_{cells}=150). Data are mean ± SD, p-values from unpaired t test compare siControl and siWnt5a groups (n=1).

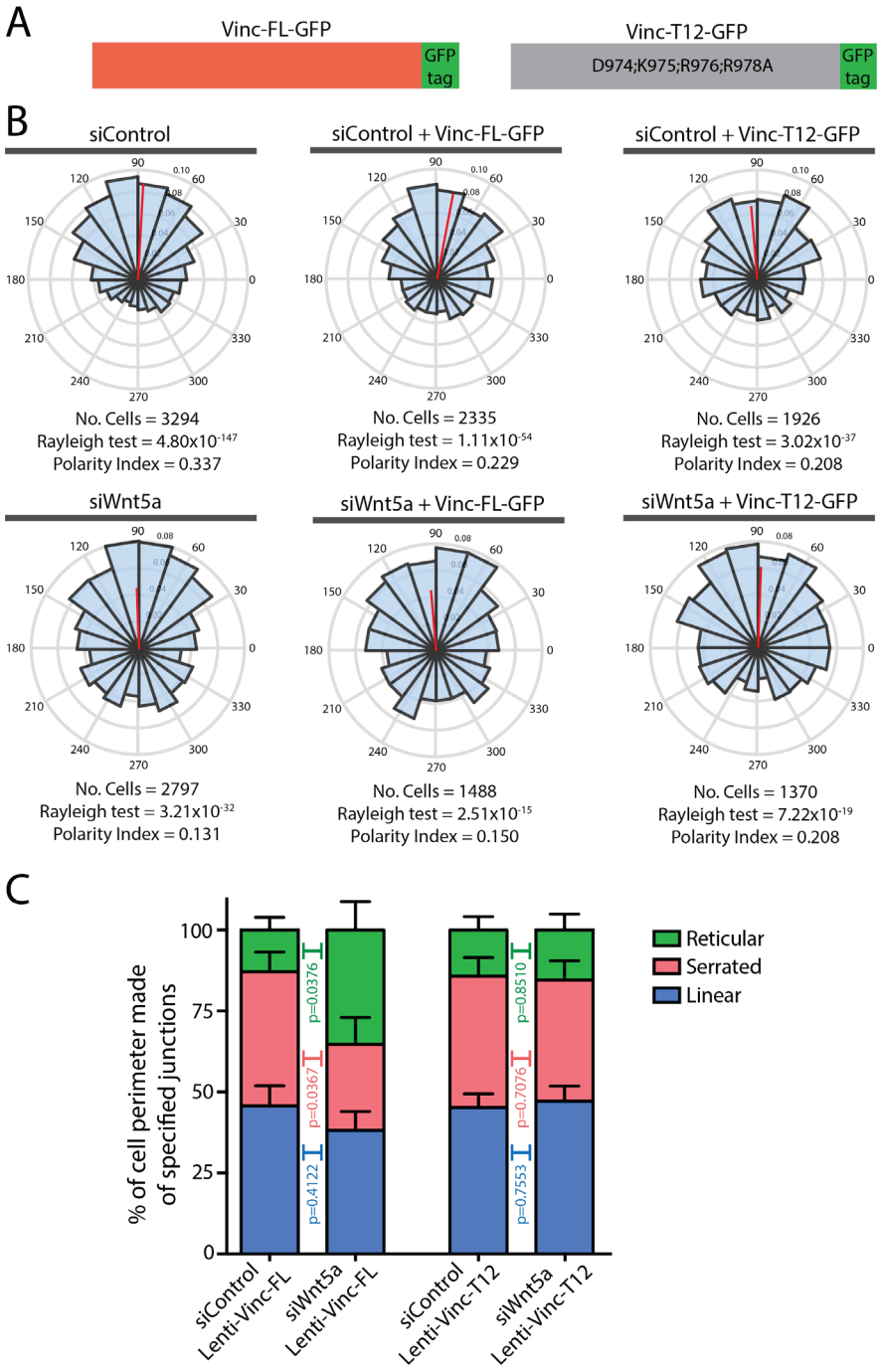

Figure 26. Vinculin reinstatement restores Wnt5a randomized cell polarity.

(A) Diagram showing the molecular structures of the Vinc-FL-GFP (left) and the Vinc-T12-GFP (right) constructs. Vinc-FL-GFP is a fusion protein containing the whole sequence of chicken vinculin (red) fused with the GFP tag (green). Vinc-T12-GFP is a fusion protein containing whole sequence of chicken vinculin with four amino acid mutations (gray) fused with the GFP tag (green).

(B) Angular histograms showing the distribution of polarization angles from siControl and siWnt5a transfected cells either non-infected (n=6) or expressing Vinculin-Full-Length-GFP (n=6) or Vinculin-T12-GFP (n=6). Area under each bin: number of cells polarized in that direction. p-values from Rayleigh test.

(C) Quantification of cell perimeter (%) composed of linear (blue), serrated (red) and reticular (green) in siControl and siWnt5a transfected cells expressing either Vinculin-Full-Length-GFP (n^{cells}=16 and 10, respectively) or Vinculin-T12-GFP (n_{cells}=21 and 20, respectively). Data are mean ± SD and p-values from unpaired t-test (n=3).

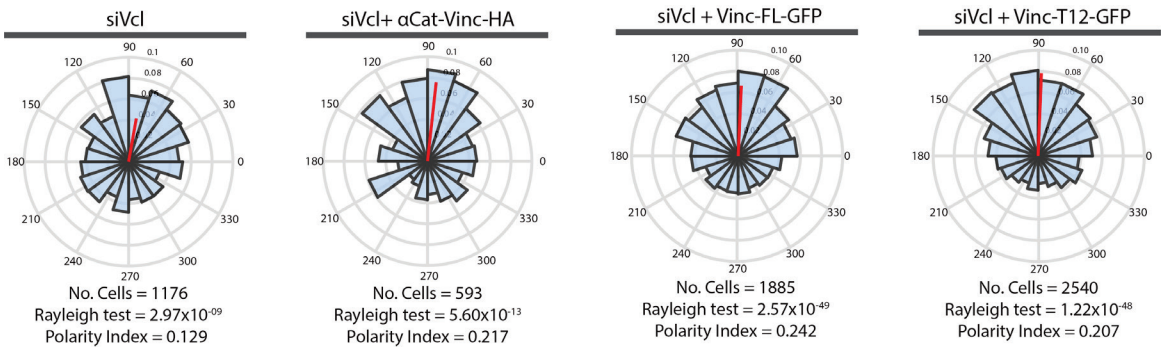

Figure 27. Overexpression of vinculin constructs rescues polarity defects of vinculin-depleted cells. Angular histograms showing the distribution of polarization angles from siVcl transfected cells either non-infected (n=2) or expressing αCat-Vinc-HA (n=2), Vinculin-Full-Length-GFP (n=2) or Vinculin-T12-GFP (n=2). Area under each bin: number of cells polarized in that direction. p-values from Rayleigh test.

IV.6. Vinculin coupling to junctional VE-cadherin is weakened in Wnt5a-deficient cells

Author contribution

The author of this thesis performed all the experiments described in the following section. Co-immunoprecipitation experiments were performed independently by the thesis author and Isabela Fortunato, MSc.

To confirm that vinculin coupling to adherens junctions was compromised in the absence of Wnt5a, we probed vinculin/VE-cadherin physical interactions by proximity ligation assay (PLA) and co-immunoprecipitation (co-IP). As expected, the PLA signal indicative of vinculin/VE-cadherin interactions was reduced in Wnt5a KD cells compared to control cells (Figure 28A, B). In agreement, co-IP of vinculin and VE-cadherin yield approximately 40% less VE-cadherin and vinculin in Wnt5a-transfected cells compared to control cells (Figure 28C, D). Thus, altogether these findings confirm that vinculin association to the adherens junctions complex is weakened in the absence of Wnt5a, thereby impairing efficient force transmission and cell-cell coordination.

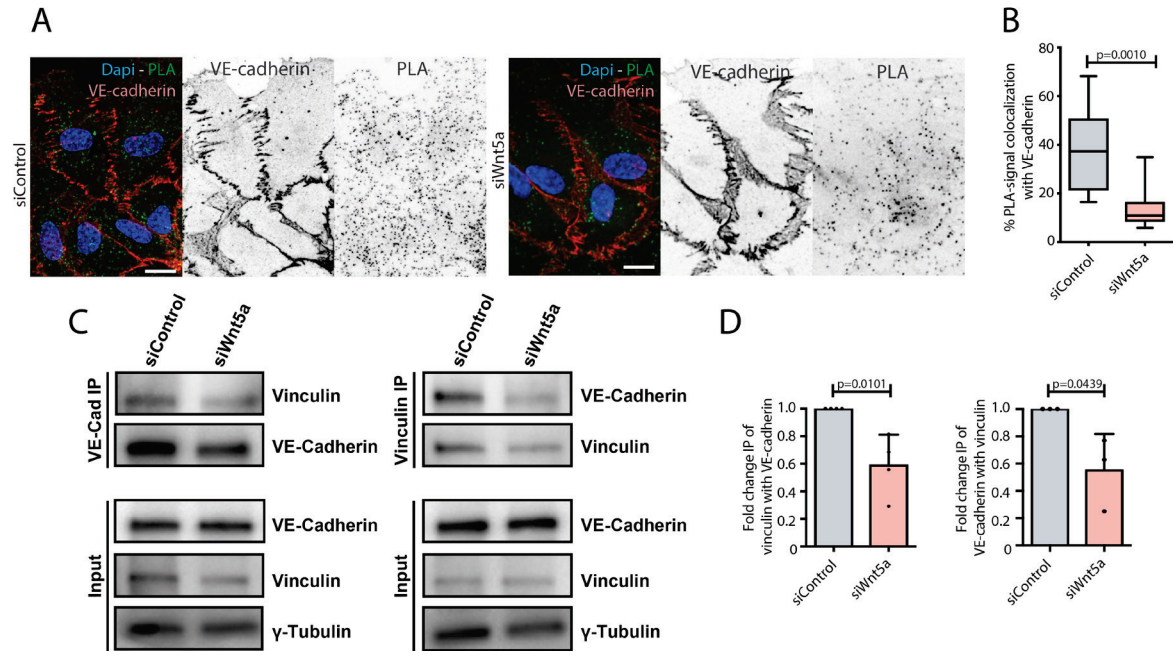

Figure 28. Vinculin association to junctional VE-cadherin is weakened in the absence of Wnt5a.

(A) Representative images of HUVECs close to the wound labeled with VE-cadherin used for proximity ligation assay (PLA) between vinculin and VE-cadherin in siControl (n=6) and siWnt5a (n=6) transfected cells. Nucleus labeled with Dapi. Scale bar, 20 µm.

(B) Co-localization (%) between PLA signal and VE-cadherin in siControl (n=6) and siWnt5a (n=6) transfected cells. Data are mean ± SD, p-values from unpaired t test.

(C) VE-cadherin and vinculin co-immunoprecipitation in siControl and siWnt5a transfected cells (n=2-3).

(D) Fold change quantification of vinculin-VE-cadherin and VE-cadherin-vinculin binding in siControl and siWnt5a transfected cells (n=3-4).

IV.7. Wnt5a signals through ROR2

Author contribution

The author of this thesis performed all the experiments described in the following section.

In order to identify how Wnt5a signaling is being transduced in the system, we screened for the effects of downregulating a set of Wnt5a receptors previously reported to be expressed in the endothelium, including Frizzled receptors (FZD), tyrosine kinase like orphan receptor 1/2 (ROR1/2) and receptor-like tyrosine kinase (RYK), using siRNAs. With this approach we identified that ROR2 KD was the only one phenocopying the polarity defects arising from Wnt5a depletion in follower cells

(PI=0.114) (Figure 29A). Moreover, ROR2 KD cells also showed a significant decrease in vinculin/VE-cadherin co-localization (Figure 29B), supporting the hypothesis that this could be the most relevant receptor involved in Wnt5a signaling.

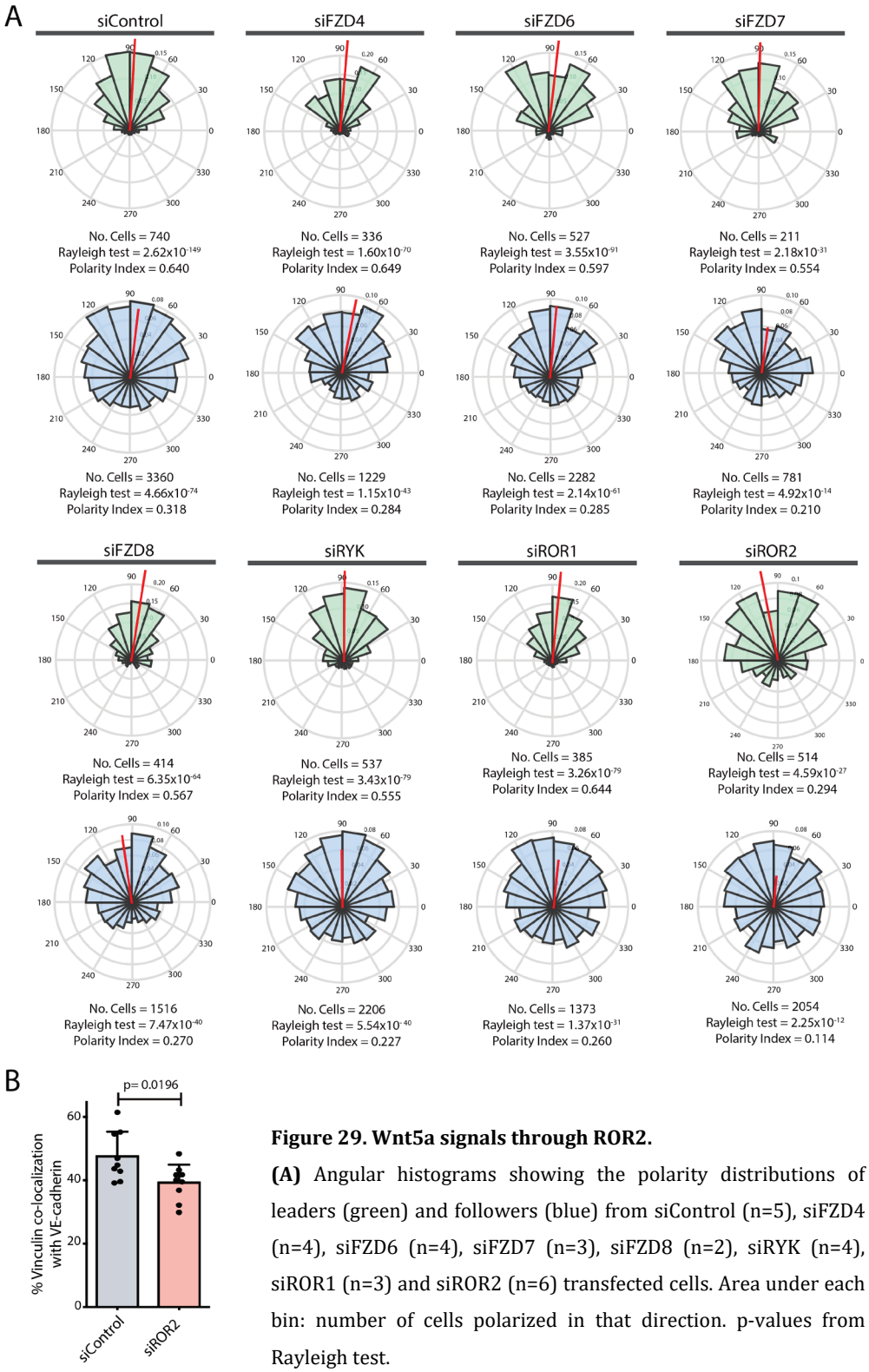

Figure 29. Wnt5a signals through ROR2.

(A) Angular histograms showing the polarity distributions of leaders (green) and followers (blue) from siControl (n=5), siFZD4 (n=4), siFZD6 (n=4), siFZD7 (n=3), siFZD8 (n=2), siRYK (n=4), siROR1 (n=3) and siROR2 (n=6) transfected cells. Area under each bin: number of cells polarized in that direction. p-values from Rayleigh test.

(B) Co-localization (%) between vinculin/VE-cadherin (n=3) in siControl and siROR2 transfected cells. Data are mean ± SD, p-values from unpaired t test.

IV.8. Wnt5a signaling is not dependent on the non-canonical calcium branch

Author contribution

The author of this thesis performed all the experiments described in the following section, with the exception of the calcium imaging experiments that were done together with Catarina Fonseca, MSc.

Non-canonical Wnt signaling is known to transduce its signals through either JNK/PCP or PKC/CamKII pathways (Kohn and Moon, 2005; Minami *et al*., 2010).

Therefore, we set out to discover which signaling branch could be activated downstream Wnt5a/ROR2. We started by exploring the calcium branch using a set of intracellular calcium modulators and analyzing their effects on control and Wnt5a-depleted ECs polarity. Intracellular calcium depletion with BAPTA-AM had a positive effect on follower cell polarity in both control and Wnt5a-depleted cells (PI=0.289 and PI=0.245) (Figure 30A). On the contrary, increasing intracellular calcium levels with either Thapsigargin or Ionomycin had the opposite effect, leading to randomized polarity in control follower cells (PI=0.054 and PI=0.111, respectively) to levels similar to those observed on Wnt5a KD cells (PI=0.053 and PI=0.072, respectively) (Figure 30A).

To test whether there were significant differences in the basal calcium levels of Wnt5a KD cells compared to control cells, we incubated cells in FURA-2 AM and imaged the wound edge to monitor oscillations in calcium levels for 20min. The basal calcium levels and peak activation in control and Wnt5a KD cells were identical (Figure 30B). Surprisingly, the major alteration we found between control and Wnt5a-depleted cells was the frequency and number of calcium peaks. On average, only 35% of Wnt5a-depleted cells had at least one calcium peak during the recordings and from those that did, the majority only had 1 or 2 peaks, while 60% of control cells produced up to 4 peaks during the same time interval (Figure 30B). Interestingly, while BAPTA-AM treatment did not affect basal calcium levels (Figure 30B), it completely abrogated the formation of calcium peaks. Therefore, taken together these results indicate that calcium activation peaks are not required for collective cell behavior and the improvement observed upon treatment with BAPTA-AM on collective cell polarity

must be due to a Wnt5a-independent effect.

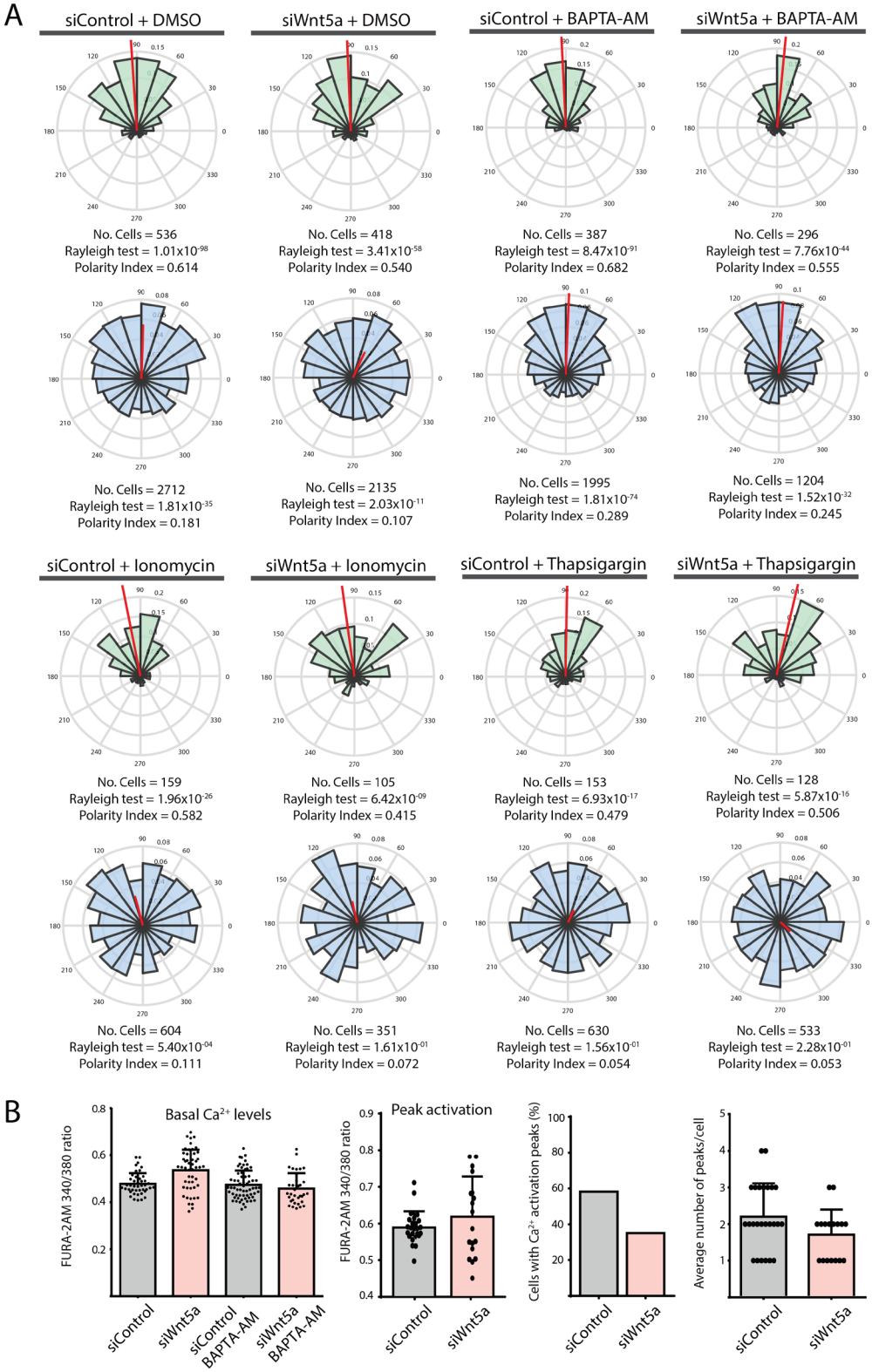

Figure 30. Wnt5a signaling is not dependent on the non-canonical calcium branch.

(A) Angular histograms showing the polarity distributions of leaders (green) and followers (blue) from siControl and siWnt5a transfected cells treated with DMSO (n=4), BAPTA-AM (n=3), Ionomycin (n=1) and Thapsigargin (n=1). Area under each bin: number of cells polarized in that direction. p-values from Rayleigh test.

Figure 30 continues on next page

Figure 30 continued

(B) Quantification of basal calcium levels, peak activation, number of cells with calcium peaks (%) and average number of calcium peaks over the course of 20min migration in siControl and siWnt5a transfected cells. Data are mean ± SD, p-values from unpaired t test (n=2).

IV.9. Wnt5a-dependent junctional vinculin depends on Cdc42 activation

Author contribution

The author of this thesis performed all the experiments described in the following section, with the exception of the FRET experiments that were done by Catarina Fonseca, MSc. Lentiviral plasmids containing protein fusion sequences were produced by Francisca Vasconcelos, PhD. FRET analysis was performed by Anna Pezzarossa, PhD.

As Wnt5a signaling acts independently of the calcium branch and ROR2 was previously shown to activate JNK, Rac1 and Cdc42 pathways downstream of Wnt5a stimulation (Green *et al*., 2014; Stricker *et al*., 2017), we decided to test whether inhibiting proteins belonging to the JNK/PCP branch would impair collective cell polarity. Curiously, inhibiting JNK (SP600125), Rac1 (NSC23766) or ROCK (Y-27632)
did not significantly decrease collective polarity in follower cells (PI=0.209, PI=0.242 and PI=0.410) (Figure 31). Interestingly, inhibiting ROCK both in control and Wnt5a KD cells improved the polarity response of follower ECs, much alike BAPTA-AM treatment (PI=0.372 and PI=0.204) (Figure 30). This observation was unexpected since ROCK inhibition had been previously reported to exert a negative impact on front-rear cell polarity (Li *et al*., 2005; Nakayama *et al*., 2008). ROCK is a kinase that phosphorylates several proteins, including myosin light chain (MLC) phosphatase, it is involved in cytoskeleton rearrangements downstream of Rho, stress fiber formation and cell contraction regulation (Amano *et al*., 1997; Watanabe *et al*., 1999). Given its function in controlling MLC phosphorylation, we treated cells either with blebbistatin or ML-7 to inhibit myosin ATPase activity or prevent MLC phosphorylation, respectively. Interestingly, both blebbistatin and ML-7 to a lesser degree, substantially improved follower cell polarity in control (PI=0.421 and PI=0.289, respectively) and

Wnt5a KD cells (PI=0.220 and PI=0.174, respectively) (Figure 32). Altogether, these findings indicate that reducing cell contractility somehow affects other mechanisms that indirectly favor cell-cell force transmission, which are sufficient to compensate for the lack of Wnt5a.

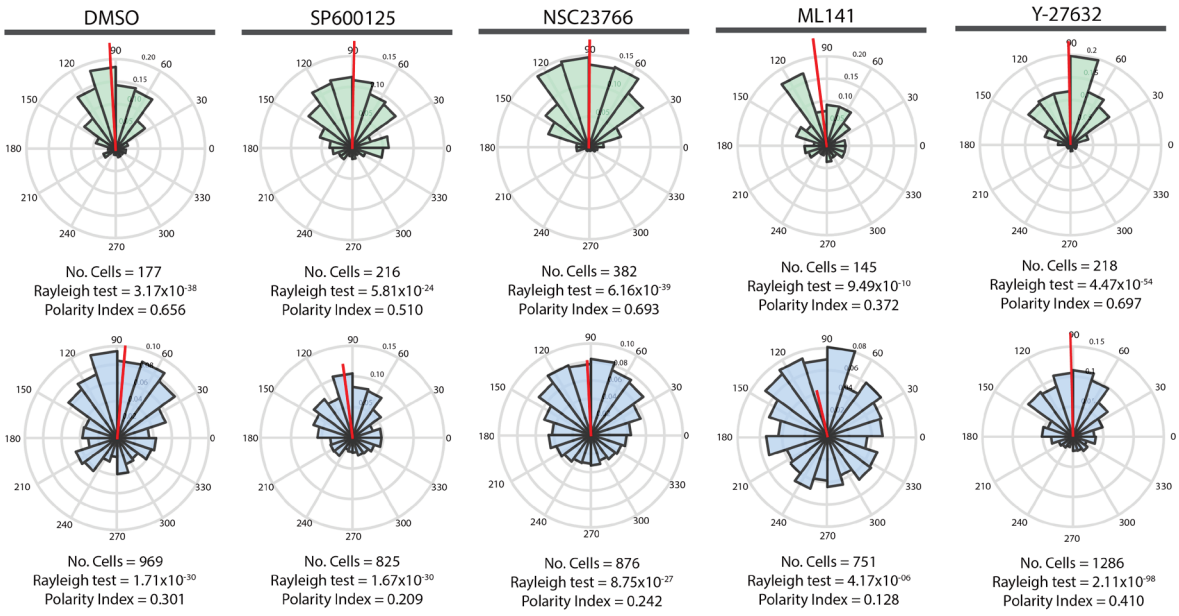

Figure 31. ROCK inhibition improves collective endothelial cell polarity.

Angular histograms showing the polarity distributions of leaders (green) and followers (blue) from wild type cells treated with either DMSO (n=2), SP600125 (n=2), NSC27632 (n=2), ML141 (n=2) and Y-27632 (n=2). Area under each bin: number of cells polarized in that direction. p-values from Rayleigh test.

Interestingly, only Cdc42 inhibition (ML141) led to randomized follower cell polarity (Figure 31) in wild-type cells (PI=0.128). We observed the same randomized cell polarity phenotype by knocking down Cdc42 (PI=0.082) or β_1Pix (ARHGEF7) (PI=0.042), a Cdc42/Rac1 guanine exchange factor (Daniels *et al.*, 1999; Manser *et al.*, 1998), therefore confirming its importance for collective cell polarity (Figure 33A). Moreover, Cdc42 depletion led to a reduction in the number of high-force discontinuous junctions and reduced the association between actin stress and VE-cadherin (Figure 33B-D). Also, Cdc42 depletion lowered vinculin/VE-cadherin co-localicalization at adherens junctions, phenocopying cells lacking Wnt5a and ROR2 (Figure 33E). In addition, PAK1-PBD-mediated pull-down of active GTP-bound Cdc42 confirmed that Wnt5a activates Cdc42 downstream of ROR2 (Figure 33F). Moreover, using a FRET sensor of active Cdc42 (Cdc42-2G) (Martin *et al.*, 2016), we observed activation of Cdc42 at cell-cell junctions in siControl cells (Figure 33G, H). Interestingly,

siWnt5a cells showed a significant decrease in the number of Cdc42-activation peaks at cell junctions, but not at the leading edge, when compared to siControl cells (Figure 33H).

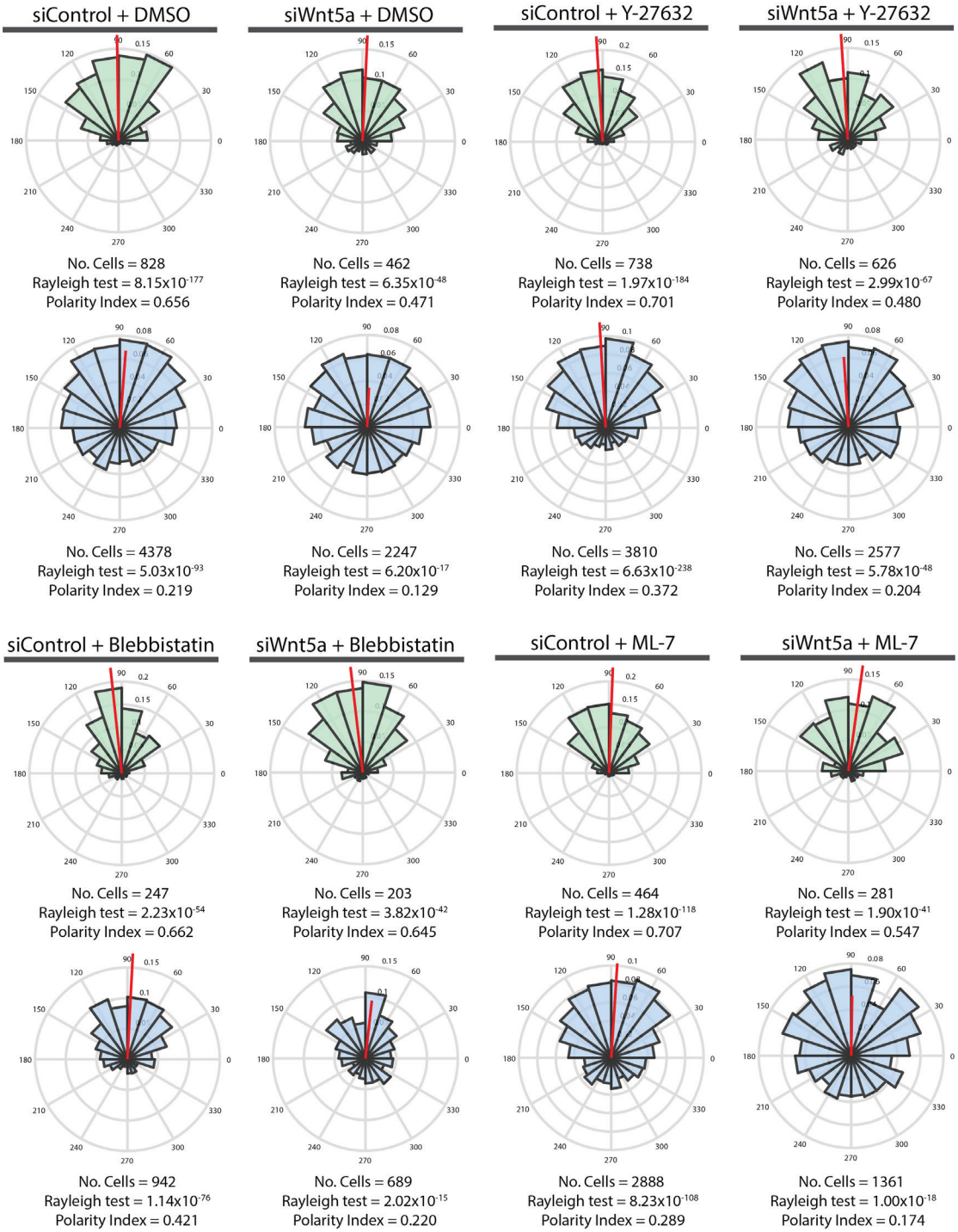

Figure 32. Reducing cell contractility can improve the polarity response of follower cells.
Angular histograms showing the polarity distributions of leaders (green) and followers (blue) from siControl and siWnt5a transfected cells treated with DMSO (n=6), Y-27632 (n=6), Blebbistatin (n=2) and ML-7 (n=3). Area under each bin: number of cells polarized in that direction. p-values from Rayleigh test.

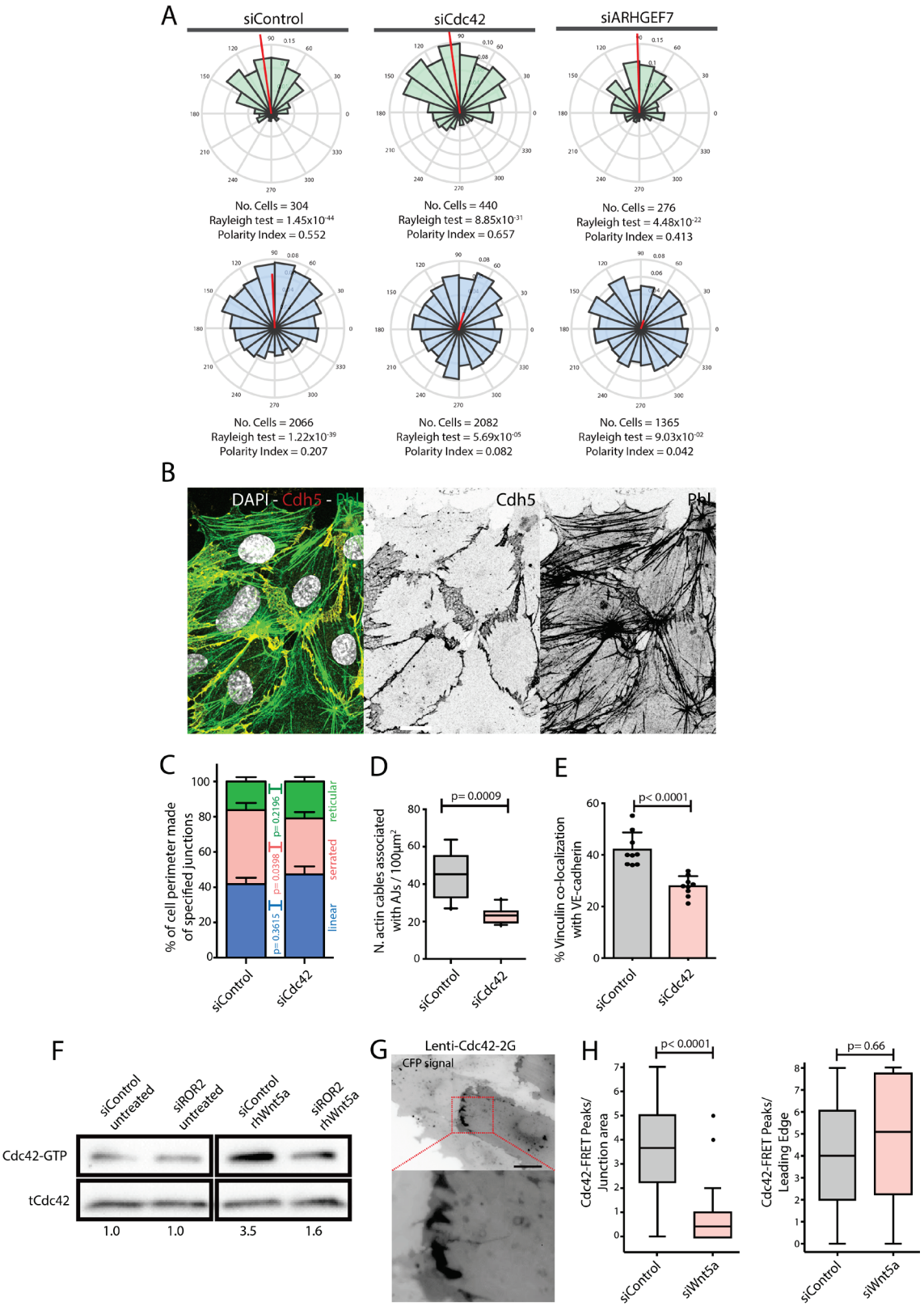

Figure 33. Wnt5a signaling seems to rely on Cdc42 activation.

(A) Angular histograms showing the polarity distributions of leaders (green) and followers (blue) from siControl (n=3), siCdc42 (n=5) and siARHGEF7 (n=3). Area under each bin: number of cells polarized in that direction. p-values from Rayleigh test.

Figure 33 continues on next page

Figure 33 continued

(B) Detail of wound edge of a migrating HUVEC monolayer showing the distribution of actin stress fibers (Phalloidin) and VE-cadherin (Cdh5) in siCdc42 transfected cells. Scale bar, 20µm.

(C) Quantification of cell perimeter (%) composed of linear (blue), serrated (red) and reticular (green) in siControl (n_{cells}=78) and siCdc42 (n_{cells}=75) transfected cells. Data are mean ± SEM and p-value from unpaired t-test (n=2).

(D) Quantification of the number of actin stress fibers connected to VE-cadherin positive cell-cell junctions in siControl or siCdc42 treated cells. Data are mean ± SD, and p-values from unpaired t-test (n=3).

(E) Quantification of co-localization (%) between vinculin/VE-cadherin (n=3) in siControl and siCdc42 transfected cells. Data are mean ± SD, p-values from unpaired t test.

(F) Pulldown of active GTP-bound Cdc42 in siControl and siROR2 transfected cells unstimulated or stimulated with recombinant human Wnt5a protein (rhWnt5a) (n=1).

(G) HUVEC expressing Cdc42-2G at adherens junction. Scale bar, 20µm.

(H) Box plots showing the number of Cdc42 FRET peaks per junction and per leading edge in siControl (n=11 cell-cell interfaces; n=5 leading edges) and siWnt5a (n=9 cell-cell interfaces; n=6 leading edges) transfected cells. p-values from unpaired t-test.

Taken together, our results showed that Wnt5a, via a ROR2/Cdc42 signaling pathway, promotes mechanocoupling between adherens junctions and the actin cytoskeleton by recruiting vinculin to α-catenin, which is necessary to promote collective endothelial cell polarity and migration.

Since Cdc42 has been shown to recruit and activate Arp2/3 (Kim *et al*., 2000; Machesky and Insall, 1999), which is implicated in Golgi reorientation during wound-healing (Magdalena *et al*., 2003), we wondered whether this actin nucleator could be required for collective cell polarity. To test this hypothesis, we depleted Arp2/3 via siRNA or blocked its activity by treating cells with Ck666. In both cases follower cells displayed randomized cell polarity, phenocopying both Wnt5a and vinculin KD cells (PI=0.109 and PI=0.066, respectively) (Figure 34), indicating that Arp2/3 is necessary for collective cell polarity. Upon closer inspection, we found that vinculin contains a binding domain for Arp2/3, which prompted us to question whether the same α-catenin-vinculin fusion protein with a point mutation in the vinculin Arp2/3 binding site (P57A), hereafter αCat-Vinc(Mut) (DeMali *et al*., 2002) (Figure 35A), would still be able to rescue polarity of Wnt5a KD cells. Interestingly, much alike VE-cad-αCat-HA, the polarity indexes of control and Wnt5a deficient cells remained unaltered (PI=0.226 and PI=0.073, respectively) (Figure 35B), suggesting that not only vinculin, but also Arp2/3 association at adherens junctions is necessary for coordinated EC behavior. In accordance, we also found a specific downregulation of Arp2/3 co-localization with

junctional VE-cadherin in the absence of Wnt5a (Figure 35C), confirming that Wnt5a signaling specifically promotes collective cell migration by promoting vinculin and Arp2/3 association at adherens junctions.

Arp2/3 is an actin nucleator that promotes the formation and expansion of new actin filaments at their barbed ends, resulting in the creation of branched actin networks (Mullins *et al*., 1998). Therefore, to investigate whether we were able to distinguish major changes in the cytoskeleton architecture of cells lacking Wnt5a, we stained control and Wnt5a-depleted cells for phalloidin to visualize the actin cytoskeleton network. Interestingly, we could not detect significant alterations in the distribution nor organization of the cell cytoskeleton in cells lacking Wnt5a (Figure 35D). However, we found a specific deficiency in the level of association of actin stress fibers to VE-cadherin junctions at high-force junctions in Wnt5a-depleted cells (Figure 35D, E). This observation is in agreement with our previous data indicating that association of vinculin and Arp2/3 is reduced in Wnt5a KD cells.

Taken together, these results suggest that Wnt5a signaling recruits vinculin and Arp2/3 to adherens junctions, enhancing actin polymerization and junction stabilization, which is crucial for force transmission and efficient collective cell migration.

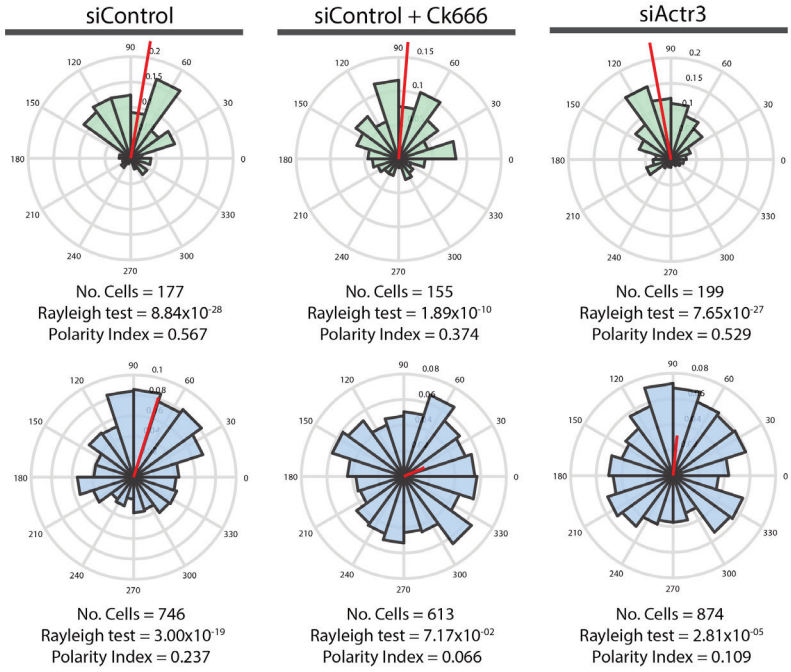

Figure 34. Arp2/3 is necessary for collective endothelial cell polarity.

Angular histograms showing the polarity distributions of leaders (green) and followers (blue) from siControl untreated (n=2) or treated with Ck666 (n=2) and siActr3 (n=2) transfected cells. Area under each bin: number of cells polarized in that direction. p-values from Rayleigh test.

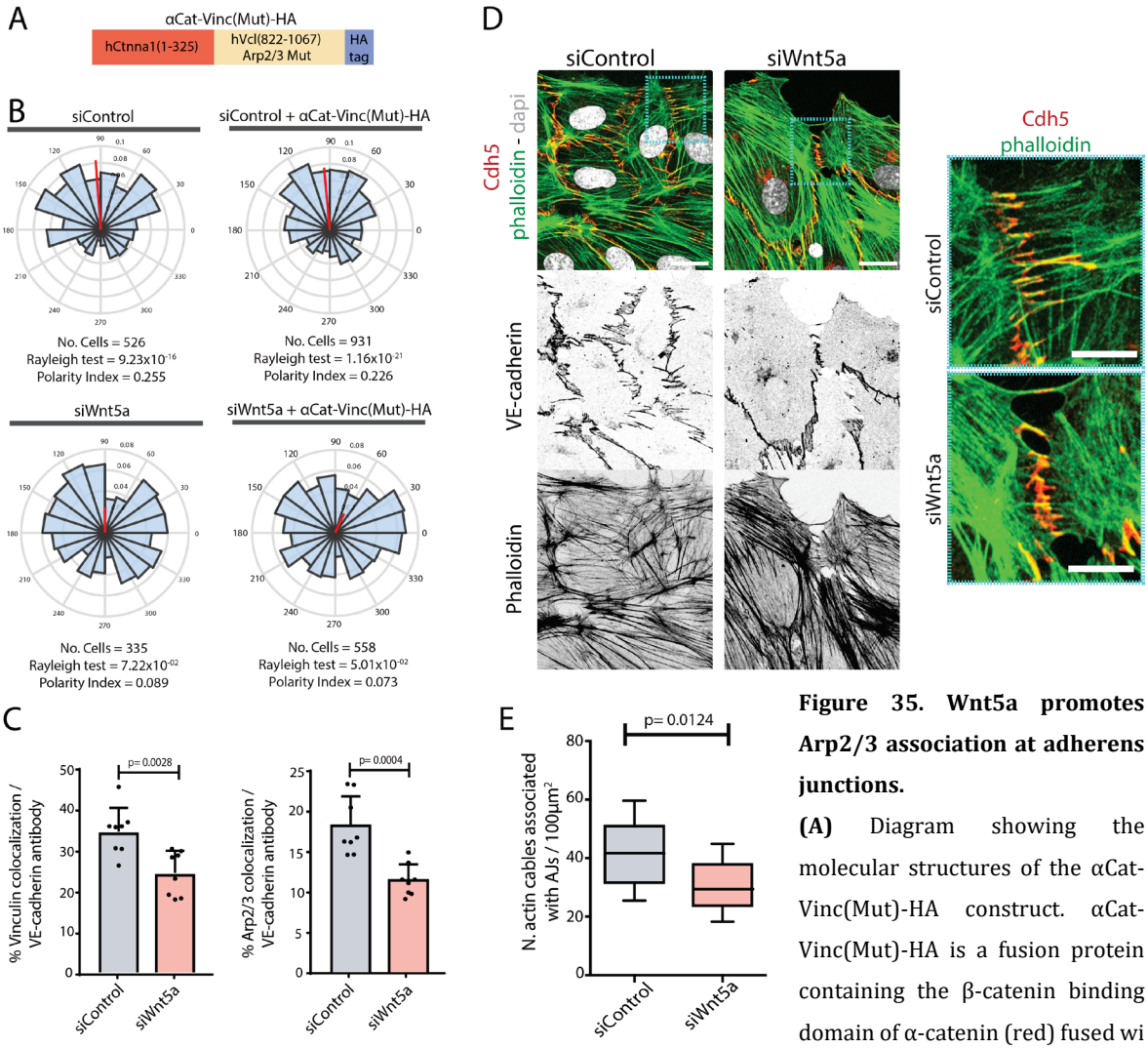

Figure 35. Wnt5a promotes Arp2/3 association at adherens junctions.

(A) Diagram showing the molecular structures of the αCat-Vinc(Mut)-HA construct. αCat-Vinc(Mut)-HA is a fusion protein containing the β-catenin binding domain of α-catenin (red) fused wi with the actin binding domain of vinculin (beige) that contains a single point mutation at the Arp2/3 binding domain and the HA tag (blue).

(B) Angular histograms showing the polarity distributions of siControl and siWnt5a transfected cells non-infected (n=2) or infected with αCat-Vinc(Mut)-HA (n=2). The area under each bin: number of cells polarized in that direction. p-values from Rayleigh test.

(C) Quantification of co-localization (%) between vinculin/VE-cadherin (n=2) and Arp2/3/VE-cadherin (n=2) in siControl and siWnt5a transfected cells. Data are mean ± SD, p-values from unpaired t test.

(D) Detail of wound edge of a migrating HUVEC monolayer showing the distribution of actin stress fibers (phalloidin) and VE-cadherin (Cdh5) in siControl and siWnt5a transfected cells. Scale bar, 20µm. Blue squares show a higher magnification of a junction in which actin stress fibers (phalloidin) are associated with VE-cadherin (Cdh5) in siControl and siWnt5a transfected cells. Scale bar= 10µm.

(E) Quantification of the number of actin stress fibers connected to VE-cadherin positive cell-cell junctions in siControl and siWnt5a cells. Data are mean ± SD, and p-values from unpaired t-test (n=2).

Chapter V. Discussion

Non-canonical Wnt signaling plays a key role in tissue polarity regulation, cytoskeleton remodeling, cell fate determination and migration, and as a result, it is crucial for several processes involving collective cell migration (Franco *et al*., 2009; Niehrs, 2012). However, in the context of angiogenesis its contribution is far less clear and only started to emerge recently. Wnt5a, a non-canonical Wnt ligand, has been described as a pro-angiogenic factor that promotes EC proliferation, migration and network formation (Masckauchan *et al*., 2006; Cirone *et al*., 2008; Descamps *et al*., 2012). More recently, Franco *et al* has shown that combined loss of non-canonical Wnt ligands – Wnt5a and Wnt11 – in retinal endothelial cells resulted in decreased radial expansion and vessel density in the mouse retina (Franco *et al*., 2016). Therefore suggesting that during the initial phase of sprouting angiogenesis non canonical Wnt signaling promotes oriented migration of vessel sprouts and the subsequent expansion of the vascular plexus. This raised the possibility that lack of Wnt5a, the most important ligand operating in the system (Franco *et al*., 2016), could compromise the ability of ECs to break symmetry and polarize correctly, and as a result, impair their directed migration capability. Thus, we decided to investigate the specific molecular mechanisms by which Wnt5a exerts these functions on ECs using a simpler, easy to manipulate, well-established *in vitro* assay – the wound-healing assay. In addition, we developed a quantitative highly reproducible system to quantify collective cell polarity, the polarity index (PI) (Figure 16). With this system, we uncovered that ECs were able to coordinate their polarities up to 350μm away from the wound edge. However, when lacking Wnt5a, this distance dropped significantly to 150μm (Figure 17A), indicating that loss of Wnt5a dramatically impairs coordination of EC collective behavior. Our results also showed that cells lacking Wnt5a migrated more randomly during wound healing, further supporting the idea that Wnt5a is necessary for EC coordination (Figure 15). Interestingly, we also showed that Wnt5a deficiency leads to randomized follower cell polarity, while it does not affect leader cells (Figure 17B). This could be explained by the fact that while follower cells heavily rely on mechanical and biochemical cues provided by leaders to polarize and migrate, leader cells are able to polarize towards their free edge, which acts as an external default polarity cue. Remarkably, we also showed that Wnt5a deficiency does not compromise the formation of cryptic lamellipodia during collective cell migration, but impairs their orientation (Figure 17E). Therefore, we believe that Wnt5a is not required for intrinsic

mechanisms of individual cell polarity response, but has an important role in promoting coordinated collective EC behavior. Interestingly, randomized follower polarity associated with Wnt5a deficiency could not be restored by providing cells with exogenous recombinant Wnt5a (Figure 18). This indicates that while Wnt5a levels are not the limiting factor acting in the system, the local and temporal activation window of the pathway must be tightly controlled at the individual cell level to ensure EC behavior coordination. Given that Wnt5a signals in a paracrine/autocrine manner in several tissues (Blumenthal *et al*., 2006; Borcherding *et al*., 2015; Pacheco and Macleod, 2008), it would be reasonable to assume that upon activation the signal should be restricted to a set of adjacent cells, which may contribute to maintain cell-cell coordination. In this sense, it would be interesting to investigate the activation patterns of leaders and followers and study how the signal propagates within the monolayer during wound healing. It also remains to be investigated whether this could be a cell-autonomous process, where all cells within the monolayer are able to secret and respond to Wnt5a signaling cues, or if, on the other hand, signaling events spreading paracrinally from a source are able to influence neighbor cell behavior without altering the signaling profiles of the recipient cells.

As collective cell migration relies on adherens junctions to enable coordinated cell behavior, we wondered whether Wnt5a might have a direct impact on cell-cell junctions components and/or organization. Morphologically we observed that cells lacking Wnt5a had a significant increase in low-force reticular junctions and a concomitant decrease in high-force discontinuous junctions near the wound edge (Figure 19), suggesting that either these cells are not able to sense mechanical forces or are unable to produce a proper mechanotransduction response. Although we were not able to detect significant alterations in the expression levels of junctional proteins in Wnt5a-depleted cells (Figure 20), we identified a specific downregulation of vinculin co-localization to VE-cadherin at cell junctions (Figure 21A, B). A combination of co-localization and calcium switch experiments led us to conclude that this specific downregulation was not caused by an intrinsic inability in recruiting vinculin to the adherens junctions, but rather a long-term stabilization issue (Figure 21C, D). This association of vinculin to cell junctions was then proved to be essential for EC collective behavior, as vinculin-depleted follower cells fully phenocopied the polarity defects of Wnt5a KD cells (Figure 22). We also found that Wnt5a-depleted cells seem to re-

localize vinculin from the adherens junctions to focal adhesions, which were larger compared to those found in control cells (Figure 21E). This could be a morphological indication of a distinct force distribution pattern within these cells – more tension force concentrated at the cell-substrate interface rather than at cell-cell junctions, presumably arising from the unstable long-term association of vinculin to cell junctions. This distinct force distribution pattern in Wnt5a-depleted cells may also contribute to the randomized cell polarity and overall lack of coordination observed during cell migration, since adjacent cells would be more engaged with the substrate rather than closely coupled mechanically.

Interestingly, vinculin has been proposed in the past to exert a protective role by binding to adherens junctions undergoing high tension to prevent them from breaking (Huveneers *et al.*, 2012). With this in mind, one can imagine two interesting possibilities: either cells lacking Wnt5a are not able to generate sufficient mechanical forces and vinculin decrease at adherens junctions is a consequence of low-force, or on the contrary, the fact that vinculin is diminished at cell junctions in Wnt5a KD cells induces cell-cell junction destabilization/rupture and therein lack of force transmission between adjacent cells. To try to distinguish between these two distinct scenarios, we first performed AFM and FRET experiments and confirmed that Wnt5a deficiency leads to a significant decrease in cell-cell force transmission, which is dependent on VE-cadherin homophilic interactions (Figure 23; Figure 24). Then, we showed that randomized cell polarity in Wnt5a-depleted cells could be rescued by forcing the association of vinculin to cell junctions by overexpressing the αCat-Vinc fusion protein (Figure 25), or by overexpressing a constitutive active form of vinculin (Vinc-T12) (Figure 26). Moreover, we confirmed in subsequent co-IP and PLA experiments that vinculin association to VE-cadherin is perturbed in Wnt5a-deficient cells (Figure 28), which explains the reason why restoring vinculin association to adherens junctions is sufficient to rescue randomized cell polarity in Wnt5a-depleted cells. Therefore, we believe that Wnt5a does not affect the intrinsic mechanical properties of ECs. However, it seems to promote vinculin association at force transmitting junctions, stabilizing them and enhancing mechanocoupling during collective cell migration.

Finally, we sought to dissect the components downstream Wnt5a and identified ROR2/Cdc42 as the most relevant signaling transducers. siRNA depletion of both ROR2

and Cdc42 led to randomized follower cell polarity and to a significant reduction in the amount of vinculin co-localizing with VE-cadherin at adherens junctions, mimicking the effects of Wnt5a depletion (Figure 29; Figure 33). Moreover, by performing a pull-down of active GTP-bound Cdc42, we showed that Wnt5a activates Cdc42 downstream of ROR2, confirming their involvement in the Wnt5a signaling cascade (Figure 33F). Interestingly, using a FRET sensor of active Cdc42 we found that in Wnt5a-depleted cells the number of Cdc42-activation peaks were decreased at cell junctions, but not at the leading edge, suggesting that Wnt5a/Cdc42 signaling is particularly important at cell-cell contacts (Figure 33G, H). This is in agreement with our previous observations and supports our hypothesis that Wnt5a plays an essential role in cell coordination during collective cell migration by promoting cell-cell mechanocoupling.

ROR2 has been reported to interact with Wnt5a in several tissues (Martinez *et al*., 2015; Oishi *et al*., 2003) and is known to signal not only through Cdc42, but also through JNK and Rac1 downstream of Wnt5a (Green *et al*., 2014; Stricker *et al*., 2017). Surprisingly, unlike previous studies (Li *et al*., 2005; Nakayama *et al*., 2008), we did not observe a negative effect on front-rear cell polarity by inhibiting ROCK. In fact, collective cell polarity response even improved when cells were treated with Y-27632 (Figure 31; Figure 32). We believe this unexpected effect is likely due to a decrease in cell contraction caused by a reduction of phosphorylated MLC. Mechanically, we observed that reducing cell contractility either by destroying myosin (blebbistatin) or preventing MLC phosphorylation (ML-7) always led to better cell polarity (Figure 30). In this context, we argue that reducing cell contractility somehow affects other mechanisms that indirectly favor cell-cell force transmission, which are sufficient to compensate for the lack of Wnt5a. This may be, for instance, due to the fact that actomyosin contraction acts primarily on focal adhesions, indirectly leading to enhanced mechanotransduction at adherens junctions. Alternatively, one may also consider the possibility that reducing actomyosin contraction may preserve junctions' ability to induce polarity cues. This is because cells with decreased actomyosin activity cannot produce enough force to induce junctional disruption. This could explain why cells have a better polarity response, even in the absence of Wnt5a.

Then we also found that Arp2/3, an actin nucleator shown to be recruited and activated by Cdc42 (Kim *et al*., 2000; Machesky and Insall, 1999), also plays a crucial role in collective EC polarity (Figure 34). Interestingly, much alike vinculin, in the absence of

Wnt5a, Arp2/3 co-localization with junctional VE-cadherin was reduced (Figure 35C). Its importance was further confirmed when we failed to restore Wnt5a polarity defects after overexpressing a mutated form of vinculin that was unable to bind to Arp2/3 (αCat-Vinc (Mut) fusion protein) (Figure 35A, B). Since Arp2/3 is directly involved in actin polymerization, we examined the actin cytoskeleton of cells lacking Wnt5a expecting to find abnormalities. Although we did not observe significant changes in the overall structure and organization of the actin cytoskeleton in Wnt5a KD cells (Figure 35D), we noticed that less actin stress fibers were associated to VE-cadherin junctions in these cells (Figure 35E). Likewise, we found the same lack of association between actin stress fibers and cell-cell junctions in Cdc42-depleted cells (Figure 33D). With these results in mind one can argue that the combined reduction of junctional vinculin and Arp2/3 may contribute to lack of force transmission and EC collective coordination caused by a disruption in Wnt5a/Cdc42 signaling at cell-cell contacts. To understand better the molecular bases of this mechanism it would be interesting to investigate in more detail the link between Wnt5a/Cdc42 signaling, Arp2/3 and vinculin by interaction and functional assays.

Based on all the data presented, we propose a model where leader cells polarize automatically towards their free edge, while activating Wnt5a signaling. Then, Wnt5a via ROR2/Cdc42 promotes vinculin and Arp2/3 association to force transmitting junctions at the boundary between leaders and followers, enhancing actin polymerization and junction stabilization and therefore enabling stable force transmission from leaders to followers. Follower cells would then activate Wnt5a signaling themselves and the cycle would repeat, leading to high EC coordination during wound-healing. In the absence of Wnt5a, cell-cell junctions lacking vinculin and Arp2/3 become unstable, and as a result, force transmission is less efficient from leaders to followers, resulting in randomized follower cell polarity and uncoordinated cell behavior during collective cell migration (Figure 36). Since Wnt signaling is an evolutionarily conserved pathway in metazoan organisms (Komiya and Habas, 2008) and is largely implicated in morphogenetic processes that require cell-cell mechanocoupling, we believe the mechanotransduction function we described here may be applicable to other tissues and contexts. In the context of vascular biology, our findings may be relevant to understand the mechanical and molecular mechanisms involved in the collective migration of vessel sprouts driven by tip cells *in vivo*. More

specifically, the role of non-canonical Wnt5a in the retinal endothelium, the contribution of adherens junctions for force transmission from tip to stalk cells and the molecular components involved in the collective polarization of blood vessel sprouts during sprouting angiogenesis. Moreover, several studies pointed out Wnt5a as a potential key regulator of cancer, acting both as a tumor suppressor and as a pro-oncogenic factor, depending on the tumor type (Dejmek *et al.*, 2005; Kurayoshi *et al.*, 2006). Therefore, it would be interesting to investigate whether the mechanisms we described here might be relevant to understand disease onset and progression and even contribute to the development of potential therapies.

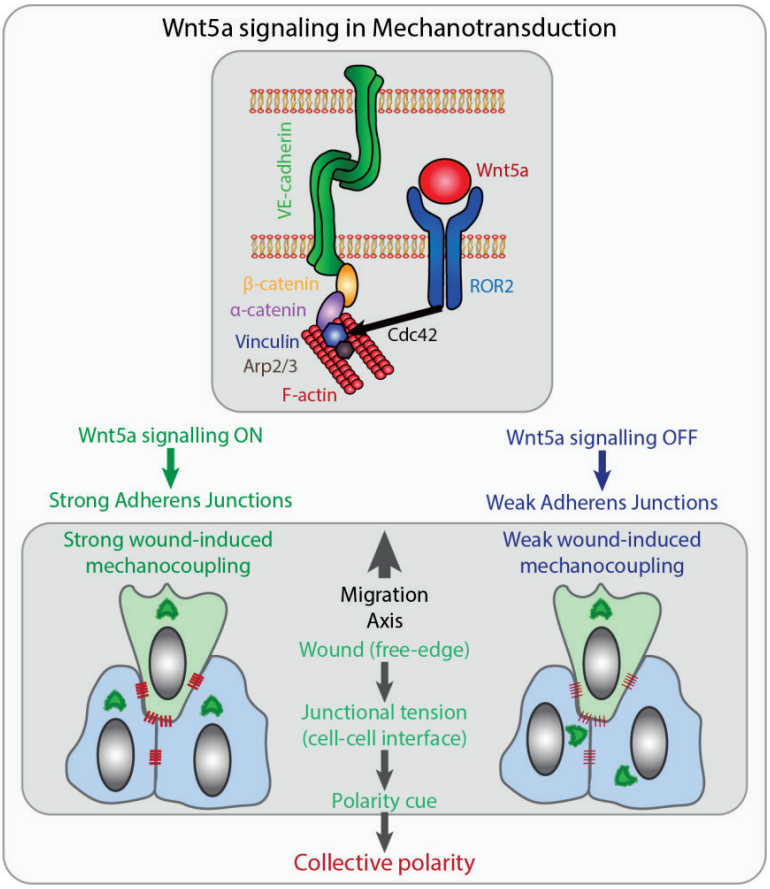

Figure 36. Working model for the role of non-canonical Wnt5a in mechanotransduction. Wnt5a, through ROR2, activates Cdc42 at adherens junctions, which is necessary for the association of vinculin and Arp2/3 to adherens junctions, and efficient mechanocoupling between endothelial cells. Low non-canonical Wnt signaling weakens adherens junctions, impairs force propagation, and disrupts collective cell migration of endothelial cells.

References

Adams, R. H. and Alitalo, K. 2007. "Molecular regulation of angiogenesis and lymphangiogenesis." *Nat. Rev. Mol. Cell Biol.* **8**, 464–478

Ananthakrishnan, R. and Ehrlicher, A. 2007. "The forces behind cell movement." *Int. J. Biol. Sci.* **3**, 303–317

Aman, A. and Piotrowski, T. 2008. "Wnt/β-catenin and Fgf signaling control collective cell migration by restricting chemokine receptor expression." *Dev. Cell* **15**, 749–761

Amano, M. *et al*. 1996. "Formation of actin stress fibers and focal adhesions enhanced by Rho-kinase." *Science*. **275**, 1308–1311

Bazellieres, E. *et al*. 2015. "Control of cell-cell forces and collective cell dynamics by the intercellular adhesome." *Nat Cell Biol* **17**, 409-420

Bear, J. E. and Haugh, J. M. 2014. "Directed migration of mesenchymal cells: where signaling and the cytoskeleton meet." *Curr. Opin. Cell Biol.* **30**, 74–82

Berens, P. 2009. "CircStat: A Matlab Toolbox for Circular Statistics." *Journal of Statistical Software* **31**, 1–21

Blumenthal, A. *et al*. 2006. "The Wingless homolog WNT5Aand its receptor Frizzled-5 regulate inflammatory responses of human mononuclear cells induced by microbial stimulation." *Blood*, **108**, 965-973

Booth-Gauthier, E. A. *et al*. 2012. "Force-induced changes in subnuclear movement and rheology." *Biophys. J.* **103**, 2423–2431

Borcherding, N. *et al*. 2015. "Paracrine WNT5A signaling inhibits expansion of tumor-initiating cells." *Cancer Res* **75**, 1972-82

Buckley, C. D. *et al*. 2014. "The minimal cadherin-catenin complex binds to actin filaments under force." *Science* **346**, 1254211

Carmona-Fontaine, C. *et al*. 2008. "Contact inhibition of locomotion in vivo controls neural crest directional migration." *Nature* **456**, 957–961

Carmeliet, P. and Jain, R. K. 2011. "Molecular mechanisms and clinical applications of angiogenesis." *Nature* **473**, 298–307

Cattelino, A. *et al*. 2003. "The conditional inactivation of the beta-catenin gene in endothelial cells causes a defective vascular pattern and increased vascular fragility." *J*

Cell Biol. **162**, 1111-22

Caussinus, E. *et al*. 2008. "Tip-cell migration controls stalk-cell intercalation during *Drosophila* tracheal tube elongation." *Curr. Biol.* **18**, 1727–1734

Chen, Q. *et al*. 2012. "Haemodynamics-driven developmental pruning of brain vasculature in zebrafish." *PLoS biology* **10**, e1001374

Chihara, T. and Hayashi, S. 2000. "Control of tracheal tubulogenesis by Wingless signaling." *Development* **127**, 4433–4442

Cirone, P. *et al*. 2008. "A role for planar cell polarity signaling in angiogenesis." *Angiogenesis* **11**, 347-360

Cohen, D. M. *et al*. 2005. "Two distinct head-tail interfaces cooperate to suppress activation of vinculin by talin." *J. Biol. Chem*. **280**, 17109-17

Conway, D. E. *et al*. 2013. "Fluid shear stress on endothelial cells modulates mechanical tension across VE-cadherin and PECAM-1." *Curr Biol.* **23**, 1024-1030

Corada, M. *et al*. 2010. "The Wnt/beta-catenin pathway modulates vascular remodeling and specification by upregulating Dll4/Notch signaling." *Dev. Cell* **18**, 938-949

Dahl, K. N. and Kalinowski, A. 2011. "Nucleoskeleton mechanics at a glance." *J. Cell Sci.* **124**, 675–678

Daneman, R. *et al*. 2009. "Wnt/beta-catenin signaling is required for CNS, but not non-CNS, angiogenesis." *Proc. Natl. Acad. Sci. U.S.A.* **106**, 641-646

Daniels, R. H. *et al*. 1999. "αPix stimulates p21-activated kinase activity through exchange factor-dependent and -independent mechanisms." *J. Biol. Chem.* **274**, 6047–6050

Das, T. *et al*. 2015. "A molecular mechanotransduction pathway regulates collective migration of epithelial cells." *Nat. Cell Biol.* **17**, 276–287

De Robertis, E. M. *et al*. 2000. "The establishment of Spemann's organizer and patterning of the vertebrate embryo." *Nat Rev Genet*. **1**, 171–181

De Smet, F. *et al*. 2009. "Mechanisms of vessel branching: filopodia on endothelial tip cells lead the way." *Arterioscler. Thromb. Vasc. Biol.* **29**, 639–649

Dejmek J. *et al*. 2005. "Wnt-5a protein expression in primary dukes B colon cancers identifies a subgroup of patients with good prognosis." *Cancer Res* **65**, 9142–9146

DeMali, K. *et al*. 2002. "Recruitment of the Arp2/3 complex to vinculin." *J Cell Biol*. **159**, 881–891

Descamps B. *et al*. 2012. "Frizzled 4 regulates arterial network organization through noncanonical Wnt/planar cell polarity signaling." *Circ. Res.* **110**, 47-58

Duchek, P. and Rorth, P. 2001. "Guidance of cell migration by EGF receptor signaling during *Drosophila* oogenesis." *Science* **291,** 131–133

Duchek, P. *et al*. 2001. "Guidance of cell migration by the *Drosophila* PDGF/VEGF receptor." *Cell* **107**, 17–26

Ehling, M. *et al*. 2013. "Notch controls retinal blood vessel maturation and quiescence." *Development* **140**, 3051-3061

Eilken, H. M. and Adams, R. H. 2010. "Dynamics of endothelial cell behavior in sprouting angiogenesis." *Curr. Opin. Cell Biol.* **22**, 617–625.

Etienne-Manneville, S. 2009. "APC in cell migration." *Adv. Exp. Med. Biol.* **656**, 30–40

Farooqui, R. and Fenteany, G. 2005. "Multiple rows of cells behind an epithelial wound edge extend cryptic lamellipodia to collectively drive cell-sheet movement." *J. Cell Sci.* **118**, 51–63

Franco C.A. *et al*. 2009. "Vascular morphogenesis: a Wnt for every vessel?" *Curr Opin Genet Dev.* **19**, 476-83

Franco C.A. *et al*. 2013. "SRF selectively controls tip cell invasive behavior in angiogenesis." *Development* **140**:2321–2333.

Franco, C. A. *et al*. 2015. "Dynamic endothelial cell rearrangements drive developmental vessel regression." *PLoS Biol.* **13**, e1002125

Franco, C. A. *et al*. 2016. "Non-canonical Wnt signalling modulates the endothelial shear stress flow sensor in vascular remodeling." *Elife* **5**, e07727

Friedl, P. and Weigelin, B. 2008. "Interstitial leukocyte trafficking and immune function." *Nature Immunol.* **9**, 839–848

Friedl, P. and Gilmour, D. 2009. "Collective cell migration in morphogenesis, regeneration and cancer." *Nat. Rev. Mol. Cell Biol.* **10**, 445–457

Ganguly, A. *et al*. 2012. "The Role of Microtubules and Their Dynamics in Cell Migration." *J Biol Chem.* **287,** 43359–43369

Gerhardt, H. *et al*. 2003. "VEGF guides angiogenic sprouting utilizing endothelial tip cell filopodia." *J. Cell Biol.* **161**, 1163–1177

Ghabrial, A. S. and Krasnow, M. A. 2006. "Social interactions among epithelial cells during tracheal branching morphogenesis." *Nature* **441**, 746–749

Green, J. *et al*. 2014. "The role of Ryk and Ror receptor tyrosine kinases in Wnt signal

transduction." *Cold Spring Harb Perspect Biol* **6**

Guolla, L. *et al.* 2012. "Force transduction and strain dynamics in actin stress fibres in response to nanonewton forces." *J. Cell Sci.* **125**, 603–613

Gupton, S.L. and Gertler, F.B. 2007. "Filopodia: the fingers that do the walking." *Sci. STKE 400*, *re5. Erratum. Sci STKE* **401**:er4

Haase, K. and Pelling, A. E. 2015. "Investigating cell mechanics with atomic force microscopy." *J R Soc Interface.* **12**, 20140970

Hayot, C. *et al.* 2005. "Characterization of the activities of actin-affecting drugs on tumor cell migration." *Toxicol Appl Pharmaco*. **211**, 30-40

Heisenberg, C.P. *et al*. 2000. "Silberblick/Wnt11 mediates convergent extension movements during zebrafish gastrulation." *Nature* 405, 76-81

Herbert, S. and Stainier, D. 2011. "Molecular control of endothelial cell behaviour during blood vessel morphogenesis." *Nat. Rev. Mol. Cell Biol.* **12**, 551-564

Hodgson, L. *et al*. 2010. "Biosensors for characterizing the dynamics of rho family GTPases in living cells." *Curr Protoc Cell Biol.* Chapter **14**: Unit 14.11.1-26.

Huang, S. *et al.* 2005. "Symmetry-breaking in mammalian cell cohort migration during tissue pattern formation: role of random-walk persistence." *Cell Motil Cytoskeleton* **61**, 201–213

Huelsken, J. and Birchmeier, W. 2001. "New aspects of Wnt signaling pathway in higher vertebrates." *Curr. Opin. Genet. Dev.* **11**, 547-553

Huveneers, S. *et al*. 2012. "Vinculin associates with endothelial VE-cadherin junctions to control force-dependent remodeling." *J Cell Biol* **196**, 641-652

Huveneers, S. and de Rooij, J. 2013. "Mechanosensitive systems at the cadherin-F-actin interface." *J Cell Sci*. **126**, 403-13

Iden, S. and Collard, J. G. 2008. "Crosstalk between small GTPases and polarity proteins in cell polarization." *Nat Rev Mol Cell Biol.* **9**, 846–59

Iruela-Arispe, M. L. and Davis, G. E. 2009. "Cellular and molecular mechanisms of vascular lumen formation." *Dev. Cell* **16**, 222–231

Jaalouk, D. E. and Lammerding, J. 2009. "Mechanotransduction gone awry." *Nat Rev Mol Cell Biol.* **10**, 63-73

Jaffe, A. B. and Hall, A. 2005. "Rho GTPases: biochemistry and biology." *Annu. Rev. Cell Dev. Biol.* **21**, 247–269

Jakobsson, L. *et al*. 2010. "Endothelial cells dynamically compete for the tip cell position during angiogenic sprouting." Nat. Cell Biol. **12**, 943–953

Ji, L. *et al*. 2008. "Fluctuations of intracellular forces during cell protrusion." *Nat. Cell Biol.* **10**, 1393–1400

Kamei, M. *et al*. 2006. "Endothelial tubes assemble from intracellular vacuoles in vivo." *Nature* **442**, 453–456

Keller, R *et al*. 2003. "How we are shaped: the biomechanics of gastrulation." *Differentiation* **71**, 171–205

Kikuchi, A. *et al*. 2011. "New insights into the mechanism of Wnt signaling pathway activation." *Int. Rev. Cell. Mol. Biol.* **291**, 21–71

Kim, A. S. *et al*. 2000. "Autoinhibition and activation mechanisms of the Wiskott-Aldrich syndrome protein." *Nature* **404**, 151-158

Kochhan, E. *et al*. 2013. "Blood flow changes coincide with cellular rearrangements during blood vessel pruning in zebrafish embryos." *PLoS One* **8**, e75060

Kohn, A. D. and Moon, R. T. 2005. "Wnt and calcium signaling: Beta-catenin-independent pathways." *Cell Calcium* **38**, 439–446

Komiya, Y. and Habas, R. 2008. "Wnt signal transduction pathways." *Organogenesis* 2, 68–75

Korn, C. *et al*. 2014. "Endothelial cell-derived non-canonical wnt ligands control vascular pruning in angiogenesis." *Development* **141**, 1757–1766

Kozopas, K.M. and Nusse R. 2002. "Direct flight muscles in Drosophila develop from cells with characteristics of founders and depend on DWnt-2 for their correct patterning." *Dev. Biol*. **243**, 312-25

Kühl, M. *et al*. 2001. "Antagonistic regulation of convergent extension movements in Xenopus by Wnt/beta-catenin and Wnt/Ca2+ signaling." *Mech Dev.* **106**, 61–76

Kurayoshi M. *et al*. 2006. "Expression of Wnt-5a is correlated with aggressiveness of gastric cancer by stimulating cell migration and invasion." *Cancer Res* **66**, 10439–10448

le Digabel, J. *et al*. 2010. "Microfabricated substrates as a tool to study cell mechanotransduction." *Med Biol Eng Comput* **48,** 965–976

le Duc, Q. *et al*. 2010. "Vinculin potentiates E-cadherin mechanosensing and is recruited to actin-anchored sites within adherens junctions in a myosin II-dependent manner." *J Cell Biol*. **189**, 1107-1115

le Noble, F. *et al*. 2008. "Neural guidance molecules, tip cells, and mechanical factors in vascular development." *Cardiovasc. Res.* **78**, 232–241

Li, Z. *et al*. 2005. "Regulation of PTEN by Rho small GTPases." *Nat Cell Biol.* **7**, 399–404

Liebner, S. *et al*. 2008. "Wnt/beta-catenin signaling controls development of the blood-brain barrier." *J. Cell Biol.* **183**, 409-417

Lobov, I. B. *et al*. 2005. "WNT7b mediates macrophage-induced programmed cell death in patterning of the vasculature." *Nature* **437**, 417–421

Machacek, M. *et al*. 2009. "Coordination of Rho GTPase activities during cell protrusion." *Nature* **461**, 99–103

Machesky, L. and Insall, R. H. 1999. "Signaling to actin dynamics." *J. Cell Biol.* **146**, 267-272

Maddugoda, M. P. *et al*. 2007. "Myosin VI and vinculin cooperate during the morphogenesis of cadherin cell-cell contacts in mammalian epithelial cells." *J Cell Biol* **178**, 529-540

Magdalena, J. *et al*. 2003. "Involvement of the Arp2/3 complex and Scar2 in Golgi polarity in scratch wound models." *Mol. Biol. Cell* **14**, 670-684

Manser, E. *et al*. 1998. "PAK kinases are directly coupled to the PIX family of nucleotide exchange factors." *Mol. Cell* **1**, 183–19

Martinez, S. *et al*. 2015. "The PTK7 and ROR2 Protein Receptors Interact in the Vertebrate WNT/Planar Cell Polarity (PCP) Pathway." *J Biol Chem.* **290**, 30562–30572.

Martin, K. *et al*. 2016. "Spatio-temporal co-ordination of RhoA, Rac1 and Cdc42 activation during prototypical edge protrusion and retraction dynamics." *Sci Rep*. **6**, 21901

Masckauchan, T. N. H. *et al*. 2006. "Wnt5a signaling induces proliferation and survival of endothelial cells in vitro and expression of MMP-1 and Tie-2." *Mol. Biol. Cell* **17**, 5163-5172

Mayor, R. and Etienne-Manneville, S. 2016. "The front and rear of collective cell migration." *Nat Rev Mol Cell Biol*. **17**, 97–109

Milde, F. *et al*. 2012. "Cell Image Velocimetry (CIV): boosting the automated quantification of cell migration in wound healing assays." *Integr Biol* (Camb) **4**, 1437-1447.

Minami, Y. *et al*. 2010. "Ror-family receptor tyrosine kinases in noncanonical Wnt signaling: Their implications in developmental morphogenesis and human diseases."

Dev Dyn **239**, 1–15

Moon, R. T. *et al*. 1997. "WNTs modulate cell fate and behavior during vertebrate development." *Trends Genet.* **13**, 157-162

Moon, R. T. *et al*. 2002. "The promise and perils of Wnt signaling through beta-catenin." *Science* **296** 1644–1646

Moore, J. K. and Cooper, J. A. 2010. "Coordinating mitosis with cell polarity: molecular motors at the cell cortex." *Semin. Cell Dev. Biol.* **21**, 283–289

Mullins, R. D. *et al*. 1998. "The interaction of Arp2/3 complex with actin: Nucleation, high affinity pointed end capping, and formation of branching networks of filaments." *Proc Natl Acad Sci*. **95**, 6181–6186

Murphy, P. A. *et al*. 2012. "Notch4 normalization reduces blood vessel size in arteriovenous malformations." *Sci Transl Med*. **4**, 117ra8

Nakayama, M. *et al*. 2008. "Rho-kinase phosphorylates PAR-3 and disrupts PAR complex formation." *Dev Cell*. **14**, 205–215

Näthke, I.S. 2004. "The adenomatous polyposis coli protein: the Achilles heel of the gut epithelium." *Annu. Rev. Cell Dev. Biol.* **20**, 337–366

Neumann, C. J. and Cohen, S. M. 1997. "Long-range action of Wingless organizes the dorsalventral axis of the Drosophila wing." *Development* **124**, 871–880

Nguyen, B. P. *et al*. 2000. "Deposition of laminin 5 in epidermal wounds regulates integrin signaling and adhesion." *Curr. Opin. Cell Biol.* **12**, 554–562

Niehrs, C. 2012. "The complex world of WNT receptor signaling." *Nat. Rev. Mol. Cell Biol.* **13**, 767-79

Nobes, C. D. and Hall, A. 1995. "Rho, Rac, and Cdc42 GTPases regulate the assembly of multimolecular focal complexes associated with actin stress fibers, lamellipodia, and filopodia." *Cell* **81**, 53–62

Nobes, C. D. and Hall, A. 1999. "Rho GTPases control polarity, protrusion, and adhesion during cell movement." *J. Cell Biol.* **144**, 1235–1244

Oishi, I. *et al*. 2003. "The receptor tyrosine kinase Ror2 is involved in non-canonical Wnt5a/JNK signalling pathway." *Genes Cells*. 8, 645-54.

Pacheco I. and Macleod RJ. 2008. "CaSR stimulates secretion of Wnt5a from colonic myofibroblasts to stimulate CDX2 and sucrase-isomaltase using Ror2 on intestinal epithelia." *Am J Physiol Gastrointest Liver Physiol*, **295**, 748-759

Peglion, F. *et al.* 2014. "Adherens junction treadmilling during collective migration." *Nat. Cell Biol.* **16**, 639–651

Peng, H. *et al*. 2013. "Integrins regulate centrosome integrity and astrocyte polarization following a wound." *Dev. Neurobiol.* **73**, 333–353

Pertz, O. *et al.* 2006. "Spatiotemporal dynamics of RhoA activity in migrating cells." *Nature* **440**, 1069–1072

Petitjean, L. et al. 2010. "Velocity fields in a collectively migrating epithelium." *Byophys J*. **98**, 1790–1800

Petrie, R. J. *et al*. 2009. "Random versus directionally persistent cell migration." *Nat. Rev. Mol. Cell Biol.* **10**, 538–549

Phng, L. K. and Gerhardt, H. 2009. "Angiogenesis: a team effort coordinated by notch." *Dev. Cell* **16**, 196–208

Phng, L. K. *et al*. 2009. "Nrarp coordinates endothelial Notch and Wnt signaling to control vessel density in angiogenesis." *Dev Cell.* **16**, 70-82

Potente, M. *et al*. 2011. "Basic and therapeutic aspects of angiogenesis" *Cell* **146**, 873-887

Pravincumar, P. *et al*. 2012. "Viscoelastic cell mechanics and actin remodeling are dependent on the rate of applied pressure." *PLoS ONE* **7**, e43938

Reffay, M. *et al.* 2014. "Interplay of RhoA and mechanical forces in collective cell migration driven by leader cells." *Nat. Cell Biol.* **16**, 217–223

Reinhart-King, C. A. *et al*. 2008. "Cell–cell mechanical communication through compliant substrates." *Biophys. J.* **95**, 6044–6051

Ribeiro, A.S. *et al*. 2016. "Atomic force microscopy and graph analysis to study the P-cadherin/SFK mechanotransduction signalling in breast cancer cells." *Nanoscale* **8**, 19390-19401.

Ridley, A. J. *et al.* 2003. "Cell migration: integrating signals from front to back." *Science* **302**, 1704–1709

Rottner, K. *et al.* 1999. "Interplay between Rac and Rho in the control of substrate contact dynamics." *Curr. Biol*. **9**, 640–648

Schulte, D. *et al*. 2011. "Stabilizing the VE-cadherin-catenin complex blocks leukocyte extravasation and vascular permeability." *EMBO J.* **30**, 4157-4170

Segditsas, S. and Tomlinson, I. 2006. "Colorectal cancer and genetic alterations in the Wnt pathway." *Oncogene* **25**, 7531–7537

Stenman, J. M. *et al*. 2008. "Canonical Wnt signaling regulates organ-specific assembly and differentiation of CNS vasculature." *Science* **322**, 1247-1250

Stricker, S. *et al*. 2017. "ROR-Family Receptor Tyrosine Kinases." *Curr Top Dev Biol* **123**, 105-142

Tambe, D. T. *et al*. 2011. "Collective cell guidance by cooperative intercellular forces." *Nat. Mater*. **10**, 469–475

Tao, Q. *et al*. 2005. "Maternal wnt11 activates the canonical wnt signaling pathway required for axis formation in Xenopus embryos." *Cell* **120**, 857–871

Thery, M. 2010. "Micropatterning as a tool to decipher cell morphogenesis and functions." *J Cell Sci* **123**, 4201–4213

Trepat, X. *et al*. 2009. "Physical forces during collective cell migration." *Nat. Phys*. **5**, 426–430

Vassilev, V. *et al*., 2017. "Catenins steer cell migration via stabilization of front-rear polarity." *Dev Cell.* **43**, 463-479

Vedula, S. R. *et al.* 2013. "Collective cell migration: a mechanistic perspective." *Physiology* **28**, 370–9

Veeman, M. T. *et al*. 2003. "A second canon. Functions and mechanisms of beta-catenin-independent Wnt signaling." *Dev Cell*. **5**, 367–377

Wang, H. *et al*. 2006. "Gene expression profile signatures indicate a role for Wnt signaling in endothelial commitment from embryonic stem cells." *Circ. Res.* **98**, 1331-1339

Wang, Q. *et al*. 2010. "Spatial restriction of FGF signaling by a matrix metalloprotease controls branching morphogenesis." *Dev. Cell* **18**, 157–164

Wang, Y. *et al*. 2012. "Norrin/Frizzled4 signaling in retinal vascular development and blood brain barrier plasticity." *Cell* **151**, 1332–1344

Watanabe, N. *et al*. 1999. "Cooperation between mDia1 and ROCK in Rho-induced actin reorganization." *Nat Cell Biol*. **1**, 136–143

Weijer, C. J. 2009. "Collective cell migration in development." *J. Cell Sci.* **122**, 3215–3223

Wheeler, A. P. and Ridley, A. J. 2004. "Why three Rho proteins? RhoA, RhoB, RhoC, and cell motility." *Exp. Cell Res.* **301**, 43–49

Wolf, K. *et al.* 2007. "Multi-step pericellular proteolysis controls the transition from individual to collective cancer cell invasion." *Nature Cell Biol.* **9**, 893–904

Yao, M. *et al*. 2014. "Force-dependent conformational switch of alpha-catenin controls vinculin binding." *Nat Commun*. **5**, 4525

Yonemura, S. *et al*. 2010. "α-catenin as a tension transducer that induces adherens junction development." *Nat. Cell Biol.* **12**, 533–542

Zaidel-Bar, R., *et al*. 2007. "Functional atlas of the integrin adhesome." *Nature Cell Biol.* **9**, 858–867

Zecca, M. 1996. "Direct and long-range action of a wingless morphogen gradient." *Cell* **87**, 833–844

Appendix

The following version of the manuscript has been accepted for publication at ELife and can be accessed online at https://elifesciences.org/articles/45853

Title

Non-canonical Wnt signaling regulates junctional mechanocoupling during angiogenic collective cell migration

Authors

Carvalho JR[1], Fortunato IC[1], Fonseca CG[1], Pezzarossa A[1], Barbacena P[1], Dominguez-Cejudo MA[1], Vasconcelos FF[1], Santos NC[1], Carvalho FA[1], Franco CA[1]*

Affiliations

[1]Instituto de Medicina Molecular - João Lobo Antunes, Faculdade de Medicina, Universidade de Lisboa, Lisbon, Portugal.

*** corresponding author:**

Claudio A. Franco, PhD

Vascular Morphogenesis Laboratory

Instituto de Medicina Molecular

Faculdade de Medicina da Universidade de Lisboa

Avenida Professor Egas Moniz

1649–028 Lisboa

Portugal

Tel +351 217999569

Fax +351 217999412

Email: cfranco@medicina.ulisboa.pt

Website: imm.medicina.ulisboa.pt/en/investigacao/labs/franco-lab

ABSTRACT

Morphogenesis of hierarchical vascular networks depends on the integration of multiple biomechanical signals by endothelial cells, the cells lining the interior of blood vessels. Expansion of vascular networks arises through sprouting angiogenesis, a process involving extensive cell rearrangements and collective cell migration. Yet, the mechanisms controlling angiogenic collective behavior remain poorly understood. Here, we show this collective cell behavior is regulated by non-canonical Wnt signaling. We identify that Wnt5a specifically activates Cdc42 at cell junctions downstream of ROR2 to reinforce coupling between adherens junctions and the actin cytoskeleton. We show that Wnt5a signaling stabilizes vinculin binding to alpha-catenin, and abrogation of vinculin *in vivo* and *in vitro* leads to uncoordinated polarity and deficient sprouting angiogenesis in *Mus musculus*. Our findings highlight how non-canonical Wnt signaling coordinates collective cell behavior during vascular morphogenesis by fine-tuning junctional mechanocoupling between endothelial cells.

INTRODUCTION

Morphogenesis is driven by coordinated and dynamic cell movements, which are regulated by a combination of chemical and physical cues (Jaalouk and Lammerding, 2009). Morphogenic cues are sensed and read at the single cell-level, yet biomechanical information is relayed to and integrated by neighboring cells leading to tissue-level collective cell behaviors. These emergent collective behaviors arise by mechanically coupling cadherin-based adhesion and actomyosin-based contraction, allowing propagation of cell-cell interactions across large cell populations (Friedl and Mayor, 2017; Lecuit and Yap, 2015; Yap et al., 2017). One of such morphogenic processes is the formation of blood vessels. Vascular morphogenesis occurs mainly through sprouting angiogenesis, a process where endothelial tip cells lead the vascular sprout, migrate and invade into avascular tissues in response to pro-angiogenic molecules. Endothelial stalk cells follow tip cells contributing to sprout elongation and branch formation through proliferation and migration (Potente and Makinen, 2017). Although sprouting angiogenesis is considered a collective cell migration process (Friedl and Gilmour, 2009; Vitorino and Meyer, 2008), little is known about the mechanisms regulating this collective behavior. Recently, endothelial cell front-rear polarity has emerged as a crucial regulator of collective behavior in sprouting angiogenesis. In fact, EC-specific deletion of NCK1/2 and Cdc42 impairs cell polarity, which correlates with decreased sprouting efficiency (Dubrac et al., 2016; Lavina et al., 2018). However, the mechanisms controlling and coordinating polarity patterns of endothelial cells during sprouting angiogenesis remain elusive.

Recent reports showed that non-canonical Wnt signaling, a known regulator of cell migration and cell polarity in key morphogenic events such as gastrulation, neural tube closure, fur orientation, and ureteric bud formation (Gray et al., 2011; Yang and Mlodzik, 2015), also controls sprouting angiogenesis and vascular remodeling (Franco et al., 2016; Korn et al., 2014). Non-canonical Wnt signaling was shown to control vascular remodeling by blocking excessive vessel regression in a flow-dependent manner (Franco et al., 2016; Korn et al., 2014). In this context, non-canonical Wnt signaling modulates the threshold for flow-dependent EC polarization, inducing premature vessel regression, and leading to a decrease in vessel density (Franco et al., 2016). In parallel, abrogation of endothelial non-canonical Wnt ligands also leads to reduce sprouting efficiency (Franco et al., 2016; Korn et al., 2014). Yet, it remains unresolved how mechanistically non-canonical Wnt signaling regulates sprouting angiogenesis.

Here, we have established a simple assay to measure endothelial collective cell behavior *in vivo* and *in vitro* using axial polarity histograms. Using this assay, we uncovered a novel Wnt5a pathway that stabilizes the binding of vinculin to α-catenin at adherens junctions, and consequently the efficient coupling between adherens junctions and the actin

cytoskeleton in endothelial cells. We showed that vinculin loss-of-function impairs collective polarity *in vivo* and *in vitro*, leading to deficient sprouting angiogenesis. Overall, we propose that non-canonical Wnt signaling coordinates collective cell behavior during vascular morphogenesis by fine-tuning junctional mechanocoupling between endothelial cells.

RESULTS

Non-canonical Wnt signaling is required for the coordination of collective cell polarity *in vitro* and *in vivo*

Non-canonical Wnt signaling deficiency leads to impaired sprouting angiogenesis, a process that requires extensive cell migration (Franco et al., 2016; Korn et al., 2014). To investigate the role of non-canonical Wnt ligands in endothelial cell migration properties we used a well-characterized model of collective cell migration, the scratch-wound assay (Tambe et al., 2011). Wnt5 is the major non-canonical Wnt ligand operating *in vivo* (Franco et al., 2016; Korn et al., 2014) and *in vitro* (Fig.1-figure supplement1A). In the scratch-wound assay, siRNA-mediated knockdown (KD) of Wnt5a, hereafter siWNT5a, significantly impaired wound closure and straightness of cell migration without affecting cell velocity in human umbilical vein endothelial cells (HUVECs) (Fig.1A). Accordingly, single cell tracking highlighted coordinated collective behavior in control siRNA (siControl) cells, whereas siWNT5a cells showed uncoordinated migration paths (Fig.1B). The correlation length calculated from particle image velocimetry (PIV) analysis (Ng et al., 2012; Petitjean et al., 2010), confirmed loss of coordinated cell migration in siWNT5a cells, although not to the same extent as in cells treated with siRNA against alpha-E-catenin (α-catenin/CTNNA1), a crucial component of adherens junctions and indispensable for collective cell migration (Fig.1C) (Bazellieres et al., 2015).

Axial polarity correlates with the direction of migration in endothelial cells *in vivo* and *in vitro* (Franco et al., 2015; Kwon et al., 2016). Taking advantage of this feature, we generated a simplified method, compared to PIV analysis, to quantify the degree of coordination between cells by measuring the front-rear cell polarity (nucleus-to-Golgi apparatus axis) at the population level. The angular histogram of axial polarities relative to the wound-edge displays the distribution of cell polarities in the monolayer relative to the wound-edge (Fig.1D). As a measure of collective polarization, we defined a polarity index (PI, see material and methods), which ranges from 1 (strongly polarized) to 0 (random distribution) (Fig.1D). The PI represents the length of the mean resultant vector (Berens, 2009). Using this approach, we measured PIs in consecutive 50 μm-wide areas from the leading edge towards the monolayer (details in Material and Methods). As expected, siCTNNA1 led to a generalized poor collective coordination of polarities demonstrated by low PIs throughout the monolayer (Fig.1E). According to the PI equation, perfect randomization should give a PI=0. However, α-catenin KD cells shows PI>0, which highlights a polarity bias caused by geometrical constraints that are generated by the free space-cell monolayer interface. Therefore, we used the polarity patterns of siCTNNA1 cells to define the threshold of PI that defines uncoordinated behavior. We established this PI threshold by determining the mean

+/- SD of the results obtained from the siCTNNA1 experiments across the monolayer. For the calculation of the mean value, we excluded the first row of cells, as these were strongly affected by wound-monolayer asymmetry, leading to a stronger polarity towards the wound. Taking these rules, we defined the PI threshold for uncoordinated migration at PI= 0.14 (corresponding to the upper limit of the mean +/- SD, PI= 0.1±0.04, in α-catenin KD experiments (Fig.1E). SiControl cells showed coordination of cell polarities up to ~300 µm from the leading edge (Fig.1E). Remarkably, siWNT5a cells showed uncoordinated polarity starting at ~150 µm from the leading edge (Fig.1E).

In the wound assay, coordinated migration emerges because leader cells, localized at the edge of the monolayer, are polarized due to the presence of a free edge, and instruct follower cells' directionality of migration through force transmission at adherens junctions (Etienne-Manneville and Hall, 2001; Friedl and Mayor, 2017). To understand the extent to which the polarization patterns of leaders and followers were affected in their polarization patterns, we measured the PI for leaders (1st row of cells) and followers (2-5th row of cells) separately (Fig.1F). Leader cells showed polarization towards the leading edge above random in all three groups: siControl (PI= 0.638), siWNT5a (PI= 0.493) and siCTNNA1 cells (PI= 0.358) (Fig.1G,H; Fig.S1B,C). However, siWNT5a (PI= 0.104) and siCTNNA1 (PI= 0.101) follower cells showed randomized polarity patterns whilst siControl follower cells displayed coordinated polarity patterns (PI= 0.345) (Fig.1I,J; Fig.1-figure supplement1B,C). Defects in collective polarity in siWNT5a follower cells were rescued by re-expression of exogenous WNT5a (Fig.1J).

Cryptic lamellipodia in follower cells have been associated with collective cell migration (Das et al., 2015). Thus, we examined if WNT5a plays a role in the formation of these pro-migratory structures. We observed that WNT5a deficiency did not compromise the formation of cryptic lamellipodia but it affected their orientation toward the leading edge (Fig.1-figure supplement1D,E). Taken together, these results indicate that WNT5a signaling is necessary to coordinate follower cell behavior at the population-level.

In vivo, endothelial tip cells lead the vascular sprout, whilst endothelial stalk cells follow tip cells and contribute to sprout elongation (Potente et al., 2011). In order to evaluate if *Wnt5a* also regulates collective cell polarity *in vivo*, we calculated PIs for endothelial cells at the vascular sprouting front in control and non-canonical Wnt signaling deficient mouse retinas (Fig.1K,L). Remarkably, we observe a significant decrease in polarity patterns of mutant retinas compared to WT retinas, similar to the effect in the *in vitro* experiments. We observed collective polarization (PI= 0.187) in control retinas demonstrating that the PI is able to capture collective behavior during sprouting angiogenesis. Whilst, non-canonical Wnt ligand deficient showed a PI close to randomization (PI= 0.094) (Fig.1M,N). Thus, endothelial-derived non-canonical Wnt signaling is required for the coordination of collective

cell polarity *in vitro* and *in vivo*.

Non-canonical Wnt signaling regulates mechanical tension at adherens junctions

To understand how Wnt5a mechanistically controls collective behavior, we analyzed its effects on the adherens junction complex, a key mediator of collective cell migration (Tambe et al., 2011). We first characterized the different junctional arrangements in endothelial cells, which are associated with low or high junctional tension (Huveneers et al., 2012). We observed that siWNT5a cells had a significant decrease in the frequency of high-force serrated junctions, and a concomitant increase in the frequency of low-force reticular junctions (Fig.2A,B). Reduction in the number of high-force junctions correlated with a decreased in the association between VE-cadherin and actin stress fibers (Fig.2C,D), suggesting that Wnt5a depletion might negatively impact on force transmission through adherens junctions.

To test this hypothesis, we used atomic force microscopy to probe mechanical strength of cell-cell interactions (Fig.3A). Control-control cell interactions required on average 1.0 fJ ($1.0x10^{-15}$ J) of work (energy) for complete cell-cell detachment (Fig.3B). siWNT5a-siWNT5a cell interactions required significant less work (0.5 fJ; $p<0.0001$) for complete cell separation (Fig.3B). EGTA-treatment, which chelates extracellular calcium and abolishes cadherin-dependent interactions, significantly reduced the strength of interactions between siControl cells, and cancelled the differences between siControl and siWNT5a conditions (Fig.3B). VE-cadherin-depleted cells showed a very similar strength of interaction as EGTA-treated cells (Fig.3B). A detailed analysis of the frequency of detachment force of each cell-cell interactions in siVE-cadherin condition highlights that the majority of strong cell-cell contacts are mediated by VE-cadherin homophilic interactions (Fig.3C). These are significantly reduced in siWNT5a cells (Fig.3C-F), suggesting that Wnt5a signaling increases the strength of cell-cell interactions through adherens junctions.

Strength of adhesion at adherens junctions relies on efficient coupling between the cytoplasmic VE-cadherin C-terminus tail and the actin cytoskeleton (Gumbiner, 2005). To confirm that WNT5a regulates tension in VE-cadherin, we used previously characterized FRET-based VE-cadherin tension sensors (Conway et al., 2013). In Wnt5a-depleted cells, VE-cadherin FRET efficiency was significantly higher than in siControl cells, implying lower level of junctional tension (Fig.3G,H). Force-insensitive VE-cadherin FRET sensors showed similar levels between siControl and siWNT5a cells (Fig.3I). Taken together, these data demonstrate that Wnt5a signaling promotes high tension at the VE-cadherin intracellular domain and strengthens cell-cell interactions.

Non-canonical Wnt signaling regulates vinculin stability at adherens junctions to

reinforce junctional mechanocoupling

Next, we investigated why loss of siWNT5a results in decreased coupling between adherens junctions and the actin cytoskeleton. First, we quantified the expression levels of key junctional proteins. We confirmed that levels of VE-cadherin, ß-catenin, α-catenin, or vinculin were unaltered between control and Wnt5a-deficient cells (Fig.4A,B). Next, we assessed the spatial distribution of components of the VE-cadherin complex by co-localization experiments (Fig.4C,D). Interestingly, we observed a significant decrease of VE-cadherin co-localization with vinculin in siWNT5a cells but no change in co-localization with other junctional proteins (Fig.4D). We further confirmed a specific decrease in vinculin recruitment to VE-cadherin in siWNT5a cells by proximity ligation assay (PLA) and co-immunoprecipitation (co-IP) (Fig.4E-H) in wounded monolayers. Altogether, these results indicate that Wnt5a is important to recruit and/or to stabilize vinculin binding to adherens junctions, which in turn is necessary for efficient collective cell polarity.

Vinculin binds adherens junctions via α-catenin. It has also been proposed that a conformational change in α-catenin promotes vinculin recruitment and binding to adherens junctions (le Duc et al., 2010; Yao et al., 2014; Yonemura et al., 2010). To test whether the impaired vinculin co-localization with VE-cadherin arises from defective α-catenin conformational change or from the inability to recruit vinculin once opened, we used a specific antibody that recognizes α-catenin in its open conformation (α18 antibody) (Yonemura et al., 2010). α18 antibody-VE-cadherin co-localization showed a significant but mild decrease (~15%) in Wnt5a-depleted cells. Yet, the decrease in vinculin-α18 antibody co-localization was stronger (~32%) in these same cells (Fig.5A,B), suggesting a possible defect in vinculin junctional localization even when α-catenin is in its open conformation. To clarify whether WNT5a affects recruitment or stabilization of vinculin to junctions, we quantified the dynamics of vinculin recruitment to adherens junctions at newly formed cell-cell junctions by performing a calcium-switch experiment in siControl and siWNT5a cells. Remarkably, the initial dynamics of vinculin recruitment were similar between siControl and siWNT5a cells. However, a significant decrease of VE-cadherin-vinculin co-localization in siWNT5a cells was observed 30 minutes after junction reassembly (Fig.5C). This suggests that rather than controlling its initial recruitment, Wnt5a signaling regulates vinculin stabilization at junctions.

Vinculin is necessary for collective cell polarity *in vitro* and *in vivo*

The role of vinculin in adherens junctions' mechanical coupling between cells, and in the regulation of collective behavior have been recently established in *in vitro* studies (Bazellieres et al., 2015; Seddiki et al., 2018). Accordingly, vinculin loss-of-function (LOF) in the scratch-wound assay results in impaired collective cell polarity and migration *in vitro*,

as reflected by the decrease in the closure rate (Fig.6A-C). In contrast, the role of vinculin in collective cell migration *in vivo* remains controversial (Alatortsev et al., 1997; Han et al., 2017). Thus, we next evaluated the relevance of vinculin in collective polarity *in vivo*, using the mouse retina model of angiogenesis. We crossed the *Vinculin* floxed mouse (Zemljic-Harpf et al., 2007) together with the *Pdgfb*-iCre mouse (Claxton et al., 2008) to genetically abrogate vinculin expression in endothelial cells in post-natal mice. *Vinculin* endothelial-specific KO (EC-KO) mice showed decreased radial expansion, decreased vessel density (Fig.6D,E), and a significant increase in the number of vessel regression profiles (Fig.6F). Strikingly, analysis of polarity patterns of endothelial cells at the sprouting front demonstrated that *Vinculin* EC-KO have a significant decrease in PI when compared with control littermates (Fig.6G-I). Altogether, these results indicate that *Vinculin* is necessary for efficient collective cell polarity in endothelial cells *in vitro* and *in vivo*. Remarkably, the *Vinculin* phenotype shows strong similarities with the one reported for non-canonical Wnt signaling EC-KO not only in terms of radial expansion, vessel density and regression profiles (Franco et al., 2016), but also in terms of polarity patterns (Fig.1M,N), suggesting that *Vinculin* might participate in a pathway regulated by non-canonical Wnt signaling

Constitutively active vinculin is sufficient to rescue collective behavior defects in Wnt5a-deficient endothelial cells

Our cumulative observations place junctional vinculin as the main mediator of Wnt5a signaling in collective cell behavior. This prompted us to test whether reinstating junctional vinculin activity would rescue Wnt5a deficiency. To this end, we overexpressed either full-length chicken vinculin (Vinc-FL) or chicken vinculin T12 (Vinc-T12) in siControl and siWNT5a cells. Vinc-T12 caries 4 amino acid mutations in its protein sequence which weaken the affinity of the auto-inhibitory head-to-tail interaction by 100-fold (Cohen et al., 2005). Thus, Vinc-T12 is considered to be a constitutively active vinculin. We confirmed that both constructs were able to efficiently rescue polarity defects of siVinculin cells (Fig.7-figure supplement1). Overexpression of either form of vinculin did not affect significantly the strength of polarity of control cells (Fig.7A,B). Remarkably, Vinc-T12 but not Vinc-FL rescued impaired polarity of Wnt5a KD cells (Fig.7A,B, and Fig.7-figure supplement2). Furthermore, overexpression of Vinc-T12 but not Vinc-FL led to a rescue in the organization of junctions in siWNT5a cells, promoting the formation of serrated high-tension junctions with the concomitant decrease in reticular junctions (Fig.7C,D). To confirm if vinculin's actin binding properties are required downstream of Wnt5a signaling pathway, we overexpressed a fusion protein containing the β-catenin binding domain of α-catenin and the actin-binding domain of vinculin (Fig. 8A) (Maddugoda et al., 2007). α-catenin-vinculin (αCat-Vinc) fusion protein strongly localizes to adherens junctions (Fig.8B). αCat-Vinc overexpression did not

significantly affect the overall PI of control cells, whilst it completely rescued collective cell polarity defects in siWNT5a cells (Fig.8C,D and Fig.8-figure supplement1). Moreover, αCat-Vinc overexpression was sufficient to rescue cell migration straightness, the ratio of displacement to trajectory length, in siWNT5a cells (Fig.8E). Altogether, these observations are highly indicative that Wnt5a signaling leads to the activation of vinculin at adherens junctions to promote stable interactions between α-catenin and the actin cytoskeleton.

Non-canonical Wnt signaling regulates junctional vinculin activity and collective cell polarity through the ROR2-Cdc42 signaling axis

To investigate how Wnt5a signaling leads to vinculin activity at the junctions, we screened for cell polarity defects upon downregulation of several known receptors for non-canonical Wnt ligands. Of all receptors tested, siROR2 was the only one phenocopying WNT5a depletion (Fig.9A,B and Fig.9-figure supplement1). Moreover, siROR2 cells also showed a significant decrease in VE-cadherin-vinculin co-localization (Fig.9C). ROR2 is a tyrosine kinase receptor and it has been shown to activate JNK, Rac1 and Cdc42 pathways downstream of Wnt5a stimulation (Green et al., 2014; Lee and Heur, 2014; Schambony and Wedlich, 2007; Stricker et al., 2017). Inhibition of Rac1 or JNK did not affect collective cell polarity (Fig.9D). However, inhibition or siCdc42 impaired collective polarity of endothelial cells (Fig.9D-F). In accordance, siCdc42 impaired vinculin co-localization with VE-cadherin (Fig.9G). Analogous to siWNT5a, siCdc42 showed a significant decrease in the number of high-force serrated junctions (Fig.9H,I), and a significant reduction in the association between actin stress fibers and VE-cadherin (Fig.9J). PAK1-PBD-mediated pull-down of active GTP-bound Cdc42 confirmed that Wnt5a activates Cdc42 via ROR2 (Fig.9K). Moreover, using a FRET sensor of active Cdc42 (Cdc42-2G) (Martin et al., 2016), we observed activation of Cdc42 at cell-cell boundaries in siControl cells (Fig.9L,M, Video 1 and 2). Interestingly, siWNT5a cells showed a significant decrease in the number of Cdc42-activation peaks at cell junctions between leader-follower or follower-follower cells when compared to siControl cells, whilst activation at the leading edge of leader cells was comparable between conditions (Fig.9N and Video 3 and 4). To test whether Cdc42 regulates collective cell polarity during sprouting angiogenesis *in vivo* (Lavina et al., 2018), we inhibited Cdc42 activity in postnatal mouse pups, as previously reported (Fantin et al., 2015), and quantified collective polarity of endothelial cells at the vascular sprouting front. Remarkably, inhibition of Cdc42 led to a specific and significant randomization of endothelial cell polarity at the angiogenic sprouting front *in vivo* (Fig.9O-Q). Thus, our results confirm that Cdc42 regulates collective cell polarity during sprouting angiogenesis *in vivo*.

Taken together, we propose that Wnt5a signaling, through ROR2-Cdc42 activity, stabilizes vinculin at adherens junctions to reinforce its connection to the actin cytoskeleton. In this

context, non-canonical Wnt signaling reinforces mechanocoupling between endothelial cells, which is essential for collective cell polarity in sprouting angiogenesis.

DISCUSSION

Sprouting angiogenesis requires efficient coordination of cell specification, cell proliferation, cell migration, and cell rearrangements. Previous work has elucidated the basic cellular and molecular mechanisms leading to endothelial tip/stalk cell specification and proliferation (Potente and Makinen, 2017). Yet, the mechanisms controlling collective cell polarity, migration and cell rearrangements at the vascular sprouting front are still poorly understood. Here, we identify a novel signaling pathway that reinforces mechanocoupling between endothelial cells to coordinate collective cell polarity and migration during sprouting angiogenesis. We uncover that Wnt5a, through ROR2, activates Cdc42 at adherens junctions, which is necessary for stable binding of vinculin to α-catenin, and efficient mechanocoupling between endothelial cells (Fig.10). Low non-canonical Wnt signaling weakens adherens junctions, impairs force propagation, and disrupts collective behavior of endothelial cells, which in turn affects angiogenic sprouting efficiency.

We identify that Cdc42 plays an important role downstream of Wnt5a-ROR2 signaling in the regulation of vinculin's stabilization and activation at adherens junctions. Cdc42 is a well-known regulator of cell polarity, playing important roles in yeast budding, epithelial polarity, migratory polarity and fate specification during cell division (Heasman and Ridley, 2008). In this context, Cdc42 frequently interacts with the PAR complex (PAR6–PAR3–aPKC) to mediate both front-rear polarity and apical-basal polarity (Etienne-Manneville and Hall, 2001, 2003; Wu et al., 2007). In endothelial cells, Cdc42 was previously implicated in filopodia formation (Barry et al., 2015; Fantin et al., 2015; Wakayama et al., 2015), adherence, junction stability (Broman et al., 2006), cell migration (Vitorino and Meyer, 2008; Wakayama et al., 2015), and more recently on collective polarity (Lavina et al., 2018). Yet, Cdc42 seems to be dispensable for apical-basal but essential for front-rear polarization (Lavina et al., 2018). Interestingly, non-canonical Wnt pathway was shown to cooperate with Cdc42/PAR complex to regulate front-rear polarity in migrating fibroblasts at the leading edge (Schlessinger et al., 2007), evoking two parallel mechanisms regulating polarity of leader cells. This fits with our own results, as leader cells were mildly affected by Wnt5a KD. In endothelial cells, we show that Wnt5a regulates Cdc42 activity at cell-cell boundaries but not at the leading edge of leader cells. This signaling spatial regulation could explain why leader cells are less affected by deficient Wnt5a signaling. Indeed, Cdc42 inhibition or LOF *in vitro* or *in vivo* gives to a stronger polarity phenotype than non-canonical Wnt signaling LOF experiments (Lavina et al., 2018). This suggests that Cdc42 is regulated by multiple inputs to control cell polarity, and that Wnt5a signaling fine-tunes Cdc42 activity at cell-cell junctions.

Our data further shows that the role of non-canonical Wnt signaling on mechanocoupling relies on vinculin stabilization at adherens junctions. The biological function of vinculin at adherens junctions has been a theme of controversy. Despite being present at high-tension junctions in several model organisms, vinculin is dispensable for zebrafish and fruitfly normal development (Alatortsev et al., 1997; Han et al., 2017). However, its absence during mouse embryonic development results in lethal cardiovascular and neuronal defects (Xu et al., 1998). To explain these differences, it has been proposed that mechanical and molecular properties of proteins from the adherens junctions might have diverged during evolution (Han et al., 2017). For instance, zebrafish α-catenin is monomeric and can form a complex with β-catenin and F-actin simultaneously, whilst the murine orthologue forms dimers and cannot bind simultaneously to F-actin and β-catenin in solution (Buckley et al., 2014; Miller et al., 2013). Thus, vinculin is required to promote efficient coupling between α-catenin and F-actin in mouse. However, the factors that would regulate these interactions are so far elusive. Our results are compatible with the idea that a Wnt5a-ROR2-Cdc42 signaling axis could have evolved in mammals to enhance cadherin mechanoproperties through vinculin. Moreover, the ability to rescue the collective cell polarity defects on Wnt5-defficient cells by re-expression of Vinc-T12 or αCat-Vinc fusion protein further suggests that Wnt5a modulates mechanocoupling efficiency by regulating vinculin's actin-binding properties. How Wnt5a affects the dynamics or affinity of vinculin to actin filaments shall be investigated in future work.

In addition, our results strongly suggest that Wnt5a acts as a permissive rather than an instructive cue regarding cell polarity. The ability to rescue the collective polarity phenotype of siWNT5a cells by re-expression of either Vinc-T12 or αCat-Vinc fusion protein implies that the polarity cue organizing collective cell polarity does not depend on Wnt5a. In this context, Wnt5a seems to be mainly necessary to potentiate mechanocoupling between cells via vinculin activation, a condition sufficient to propagate the external polarity cue in the system. This is also concordant with our previous observations that overexpression of Wnt5a in endothelial cells *in vivo* led to normal vascular sprouting and remodeling phenotypes (Franco et al., 2016). Interestingly, a similar debate regarding a permissive or instructive role involves non-canonical Wnt signaling in planar cell polarity (PCP) establishment (Humphries and Mlodzik, 2018), where conflicting evidences exists in favor of each role. Our results suggest that non-canonical Wnt signaling plays a role in force transmission within cell populations. As mechanical cues were shown to play a contributing role in PCP establishment (Humphries and Mlodzik, 2018), a mechanobiology perspective into the function of non-canonical Wnt signaling in PCP could in part conciliate the possibility that non-canonical Wnt signaling can be seen as instructive or permissive, depending on

the experimental setting.

Non-canonical Wnt signaling was previously implicated in the regulation of vessel regression (Franco et al., 2016; Korn et al., 2014). Intriguingly, *Vinculin* EC-KO shows a very similar phenotype, with an increase in vessel regression, and a decrease in vessel density and radial expansion. It was suggested that non-canonical Wnt signaling regulates vessel regression by controlling a mechanosensitive threshold, based on wall shear stress, that induces endothelial cell polarization and migration (Franco et al., 2016). The mechanisms controlling this threshold are still unclear. Given the well-known mechanoresponsive proprieties of vinculin, it is tempting to speculate that vinculin could also play a relevant role in establishing this threshold. Further work is necessary to clarify this question. Nevertheless, it is relevant to note that Wnt5a and vinculin regulates a different mechanosensitive pathway in flow-independent conditions. This also raises the question of how shear stress and junctional mechanotransduction pathways are regulated and coordinated by non-canonical Wnt signaling in space and time within the vascular network.

Taken together, our results show that Wnt5a signaling fine-tunes junctional mechanocoupling between endothelial cells to promote collective cell behavior during vascular morphogenesis.

ACKNOWLEDGEMENTS

The authors thank M. Schwartz (Yale University, New Haven) for plasmids; R.S. Ross (University of California, San Diego) for providing the Vinculin floxed mouse; M. Takeichi (RIKEN, Kobe) for a18 antibody; A.C. Vion and H. Gerhardt (Max-Delbruck Center, Berlin) for providing the basis of our Matlab script for automated polarity analysis; and M. Nakayama (MPI Bad Nauheim), J. Barata, D. Henrique, and E. Gomes (iMM, Lisbon) for discussions. Research was supported by European Research Council starting grant (679368), the H2020-Twinning grant (692322), the Fundação para a Ciência e a Tecnologia funding (grants: IF/00412/2012; EXPL-BEX-BCM-2258-2013; PRECISE-LISBOA-01-0145-FEDER-016394; and a grant from the Fondation Leducq (17CVD03); and personal fellowships: BD/52224/2013 to J.R.C., BD/105856/2014 to P.B., and BD/128375/2017 to C.F.) and LISBOA-01-0145-FEDER-007391, project cofunded by FEDER, through POR Lisboa 2020 - Programa Operacional Regional de Lisboa, PORTUGAL 2020, and Fundação para a Ciência e a Tecnologia. Authors declare no competing interests.

FIGURE LEGENDS

Figure 1 - Wnt5a regulates endothelial collective cell migration in vitro and in vivo.
(A) Quantification of wound closure, straightness and cell velocity over the course of 16h migration in siControl (n= 100 cells, from 2 independent experiments) and siWNT5a (n= 100 cells, from 2 independent experiments) transfected cells. Data are mean ± SEM, p-values from unpaired t-test.
(B) Wound edge of siControl (left) and siWNT5a (right) transfected cells showing individual cell trajectories within the monolayer. Circles indicate cell nuclei. Scale bar, 50μm.
(C) Correlation length box plots from siControl (n= 6), siWNT5a (n= 8) and siCtnna1 (n= 3).
(D) Polarity axis of each cell was defined as the angle (α) between the scratch edge and the cell polarity axis, defined by the vector drawn from the center of the cell nucleus to the center of the Golgi apparatus. The polarity index was calculated according to the formula and it was used as a measure for collective polarization.
(E) Polarity index as function of the distance from the leading edge (μm) in HUVECs monolayers binning data every 50 μm. Green area corresponds to the mean +/- SD of the PI obtained of siCtnna1 cells across the monolayer, excluding leader cells.
(F) Representative images of scratch-wound assay showing polarity angles of siControl and siWNT5a KD endothelial cells. Scale bar, 50 μm.
(G) Angular histograms showing the distribution of polarization angles of leader cells from siControl (n= 13 images, from 6 independent experiments) and siWNT5a (n= 19 images, from 8 independent experiments).
(H) Polarity index box plots of non-infected siControl (n= 13 images, from 6 independent experiments) and siWNT5a (n= 19 images, from 8 independent experiments) leader cells or from siControl (n= 5 images, from 3 independent experiments) and siWNT5a (n= 6 images, from 3 independent experiments) leader cells transduced with WNT5a-V5 lentiviruses. p-values from unpaired t-test.
(I) Angular histograms showing the distribution of polarization angles of follower cells from siControl (n= 13 images, from 6 independent experiments) and siWNT5a (n= 19 images, from 8 independent experiments).
(J) Polarity index box plots of non-infected siControl (n= 13 images, from 6 independent experiments) and siWNT5a (n= 19 images, from 8 independent experiments) follower cells or from siControl (n= 5 images, from 3 independent experiments) and siWNT5a (n= 6 images, from 3 independent experiments) follower cells transduced with Wnt5a lentiviruses. p-values from unpaired t-test.
(K) Representative images of sprouting fronts from *Wnt5a* WT; *Wnt11* WT and *Wnt5a* EC-KO; *Wnt11* KO mouse retinas labeled for EC nuclei (Erg, green), lumen (Icam2, blue/grey)

and Golgi (Golph4, red). Each insert shows corresponding image segmentation of the vascular plexus showing axial polarity vectors (red) and lumen of blood vessels (grey). Scale bar, 200 μm.

(L) Polarity axis of each cell was defined as the angle (α) between the sprouting front edge and the cell polarity axis, defined by the vector drawn from the center of the cell nucleus to the center of the Golgi apparatus.

(M) Angular histograms showing the distribution of polarization angles of endothelial cells at the vascular sprouting front from *Wnt5a* WT; *Wnt11* WT (n= 4 retinas) and *Wnt5a* EC-KO; *Wnt11* KO (n= 4 retinas) mouse retinas.

(N) Polarity index box plots of endothelial cells from *Wnt5a* WT; *Wnt11* WT (n= 4 retinas) and *Wnt5a* EC-KO; *Wnt11* KO (n= 4 retinas) mouse retinas. p-values from unpaired t-test.

Figure 2 - Wnt5a regulates adherens junctions' organization.

(A) Example of the distinct junctions' morphologies in endothelial cells labeled for adherens junctions (VE-Cadherin) showing: linear (blue), serrated (red) and reticular (green). Scale bar, 10μm.

(B) Quantification of cell perimeter (%) composed of linear (blue), serrated (red) and reticular (green) in siControl (n= 22 leader and n= 40 follower cells, from 4 independent experiments) and siWNT5a (n= 40 leader and n= 46 follower cells, from 6 independent experiments) transfected cells. Data are mean ± SD and p-values from unpaired t-test.

(C) Detail of wound edge of HUVECs showing the association of actin stress fibers (phalloidin) to the adherens junctions (VE-Cadherin) in siControl and siWNT5a transfected cells. Nucleus labeled with Dapi. Scale bar, 20μm. Blue squares show a higher magnification of the association of actin filaments (phalloidin) and adherens junctions (VE-Cadherin) in siControl and siWNT5a cells. Scale bar, 10 μm.

(D) Quantification of the number of actin stress fibers connected to VE-cadherin positive cell-cell junctions in siControl and siWNT5a cells. N= 10 images, from 2 independent experiments. Data are mean ± SD, and p-values from unpaired t-test.

Figure 3 - Wnt5a signalling strengthens adherens junctions and enhances cell-cell force transmission.

(A) Diagram depicting the 4 steps involved in cell-cell adhesion measurements using atomic force microscopy (AFM), as well as its correspondence in the force-distance curves: (1) Attaching – cell attached to the tipless cantilever is lowered to make contact with another cell at the bottom; (2) Attached – cells establish cell-cell contact; (3) Detaching – the upper cell is pulled in order to break the cell-cell contact previously established; (4) Detached – cells are again fully separated. The grey area between the approach (red) and retraction

(blue) curves corresponds to the value of work (energy necessary to overcome the cell-cell adhesion). The total force necessary to separate the two cells can also be obtained from the yy axis.

(B) Quantification of the work necessary for cell-cell detachment in siControl with (n= 155 cell-cell interactions, from 5 independent experiments) or without EGTA (n= 395 cell-cell interactions, from 5 independent experiments), siWNT5a with (n= 205 cell-cell interactions, from 6 independent experiments) or without EGTA (n= 299 cell-cell interactions, from 6 independent experiments) and siCdh5 (n= 80 cell-cell interactions, from 1 experiment) transfected cells. Data are mean ± SEM, p-values from multiple comparisons in one-way ANOVA.

(C) Maximum detachment force histogram for siCdh5 transfected cells (n= 80 cell-cell interactions, from 1 experiment). Data obtained from 1 independent experiment.

(D) Maximum detachment force histogram for siControl transfected cells (n= 395 cell-cell interactions, from 5 independent experiments)

(E) Maximum detachment force histogram for siWNT5a transfected cells (n= 299 cell-cell interactions, from 6 independent experiments).

(F) The percentage (%) of cadherin-dependent interactions was calculated by dividing the number of events with detachment force above 150pN by the total number of events on each condition. The quantification of the percentage of the Cadherin-dependent interactions was based on the result obtained from the siCdh5-siCdh5 detachment force histogram (in panel C).

(G) Diagram showing the molecular structure and mechanism of action of the FRET VE-cadherin tension sensor (VE-Cad TS) or VE-cadherin tailess sensor (VE-Cad TL).

(H) HUVEC expressing VE-Cad TS undergoing FRET acceptor photobleaching at the adherens junction. Squares show the cell junction before (top) and after photobleaching (bottom). Scale bar= 10 μm.

(I) Quantification of FRET efficiency in siControl (n= 51 cell-cell junctions, from 6 independent experiments) and siWNT5a (n= 69 cell-cell junctions, from 6 independent experiments) transfected cells expressing either VE-Cad TS or the tailless biosensor lacking the β-catenin binding-domain, VE-Cad TL (n= 3 cell-cell junctions, from 1 experiment for both siControl and siWNT5a conditions). Mean ± SD, p-values from unpaired t-test.

Figure 4 - Wnt5a signaling promotes association of vinculin to the adherens junction complex

(A) Western blot for VE-cadherin, vinculin, α-catenin and β-catenin and α-tubulin in siControl and siWNT5a transfected cells.

(B) Quantification of VE-cadherin, vinculin, α-catenin and β-catenin relative protein normalized to α-tubulin. Data are mean ± SD, p-values from unpaired t-test (n= 5 independent experiments).
(C) Representative images of HUVECs close to the wound labeled for VE-cadherin and vinculin used for co-localization analysis in siControl (top left) and siWNT5a (bottom left) transfected cells and the corresponding segmentation image showing the co-localizing pixels between both stainings in black (top and bottom right). Green (top right), blue (middle right) and red (bottom right) squares show a higher magnification of a junction where VE-cadherin and vinculin co-localize. Scale bar, 40μm.
(D) Co-localization (%) between α-catenin/VE-cadherin (n= 8 images, from 3 independent experiments), β-catenin/VE-cadherin (n= 5 images, from 2 independent experiments), p120Catenin/VE-cadherin (n= 6 images, from 2 independent experiments), and vinculin/VE-cadherin (n= 39 images, from 6 independent experiments) in siControl and siWNT5a transfected cells. Data are mean ± SD, p-values from unpaired t-test.
(E) Representative images of HUVECs close to the wound labeled with VE-cadherin used for proximity ligation assay (PLA) between vinculin and VE-cadherin in siControl and siWNT5a transfected cells. Nucleus labeled with Dapi. Scale bar, 20 μm.
(F) Co-localization (%) between PLA signal and VE-cadherin in siControl (n= 12 images, 6 independent experiments) and siWNT5a (n= 12 images, 6 independent experiments) transfected cells. Data are mean ± SD, p-values from unpaired t test.
(G) VE-cadherin (n= 3) and vinculin (n= 4) co-immunoprecipitation in siControl and siWNT5a transfected cells. GAPDH co-immunoprecipitation was used as a control.
(H) Fold change quantification of vinculin-VE-cadherin (n= 3) and VE-cadherin-vinculin (n= 4) binding in siControl and siWNT5a transfected cells. Data are mean ± SD, p-values from unpaired t test.

Figure 5 - Wnt5a signaling stabilizes vinculin at adherens junctions.
(A) Representative images of HUVECs close to the wound stained for nuclei (Dapi), VE-cadherin (Cdh5), α18-catenin and vinculin for co-localization studies in siControl and siWNT5a transfected cells. Scale bar, 20 μm.
(B) Co-localization (%) between α18-catenin/VE-Cadherin and vinculin/α18 catenin in siControl (n= 12 images, 3 independent experiments) and siWNT5a (n= 12 images, 3 independent experiments) transfected cells. Data are mean ± SD, p-values from unpaired t-test.
(C) Co-localization (%) between vinculin/VE-cadherin as function of calcium incubation time (min) after the calcium switch in HUVECs monolayers of siControl and siWNT5a transfected cells. Data are mean ± SD, p-values from unpaired t-test (n= 9-15 images per time point

per condition, from 2-3 independent experiments).

Figure 6 – Vinculin is essential for sprouting angiogenesis and collective cell polarity.
(A) Angular histograms showing the distribution of polarization angles from siControl (n=10) and siVinculin (n=11) transfected cells.
(B) Polarity index box plots of leaders and followers from siControl (n= 8 images, from 4 independent experiments) and siVinculin (n= 6 images, from 3 independent experiments). p-values from unpaired t-test.
(C) Quantification of wound closure over the course of 16h migration in siControl and siWNT5a transfected cells. N= 4 independent experiments. Data are mean ± SEM, p-values from unpaired t-test.
(D) Representative images of overviews of mouse retinas from *Vinculin* WT and *Vinculin* EC-KO labeled for CD31. Scale bar, 250 µm.
(E) Box plots of vascular outgrowth, vessel density, number of branch points and EC density in *Vinculin* WT (n= 6 retinas) and *Vinculin* EC-KO (n= 6 retinas) mouse retinas. p-values from unpaired t-test.
(F) Box plot of vessel regression events in *Vinculin* WT (n= 4 retinas) and *Vinculin* EC-KO (n= 6 retinas) mouse retinas. p-values from unpaired t-test.
(G) Representative images of sprouting fronts from *Vinculin* WT and *Vinculin* EC-KO; mouse retinas labeled for EC nuclei (Erg, green), lumen (Icam2, blue) and Golgi (Golph4, red). Each insert shows corresponding image segmentation of the vascular plexus showing axial polarity vectors. Scale bar, 200 µm.
(H) Angular histograms showing the distribution of polarization angles of endothelial cells at the vascular sprouting front from *Vinculin* WT (n= 4 retinas) and *Vinculin* EC-KO (n= 4 retinas) mouse retinas.
(I) Polarity index box plots of endothelial cells at the vascular sprouting front from *Vinculin* WT (n= 4 retinas) and *Vinculin* EC KO (n= 4 retinas) mouse retinas. p-values from unpaired t-test.

Figure 7 - Active vinculin rescues Wnt5a deficiency.
(A) Angular histograms showing the distribution of polarization angles from siControl and siWNT5a transfected cells either non-infected (n= 21-23 images, from 6 independent experiments) or expressing Vinculin-Full-Length-GFP (n= 9-11 images, from 6 independent experiments) or Vinculin-T12-GFP (n= 9-11 images, from 6 independent experiments).
(B) Polarity index box plots of siControl and siWNT5a transfected cells either non-infected (n= 21-23 images, from 6 independent experiments) or Vinculin-Full-Length-GFP (n= 9-11 images, from 6 independent experiments) or Vinculin-T12-GFP (n= 9-11 images, from 6

independent experiments). p-values from unpaired t-test.

(C) siControl and siWNT5a transfected HUVECs expressing Vinculin-Full-Length-GFP and Vinculin-T12-GFP. Nucleus labelled with Dapi, Golgi apparatus with GM130 and adherens junctions with VE-Cadherin. Scale bar, 20 μm.

(D) Quantification of cell perimeter (%) composed of linear (blue), serrated (red) and reticular (green) in siControl and siWNT5a transfected cells expressing either Vinculin-Full-Length-GFP (n= 16 and 10 cells, respectively, from 3 independent experiments) or Vinculin-T12-GFP (n= 20 and 21 cells, respectively, from 3 independent experiments). Data are mean ± SD and p-values from unpaired t-test.

Figure 8 - **Forced vinculin binding to a-catenin rescues Wnt5a KD phenotype.**

(A) Diagram showing the molecular structure of the αCat-Vinc construct. αCat-Vinc-HA is a fusion protein containing the β-catenin-binding domain of α-catenin (brown) fused with the actin-binding domain of vinculin (gray) and the HA tag (blue).

(B) Example of HUVECs expressing αCat-Vinc-HA. Nucleus labelled with Dapi, adherens junctions with VE-Cadherin. Scale bar, 20μm. Blue square 1 (bottom left) shows a higher magnification of a reticular junction where HA does not co-localize with VE-Cadherin. Blue square 2 (bottom right) shows a higher magnification of a linear junction where HA and VE-cadherin co-localize.

(C) Angular histograms showing the distribution of polarization angles from siControl and siWNT5a cells either non-infected (n= 22-24 images, from 6 independent experiments) or expressing αCat-Vinc-HA (n= 11-12 images, from 6 independent experiments).

(D) Polarity index box plots of siControl and siWNT5a cells either non-infected (n= 22-24 images, from 6 independent experiments) or expressing αCat-Vinc-HA (n= 11-12 images, from 6 independent experiments). p-values from unpaired t-test.

(E) Quantification of cell velocity and straightness over the course of 16h migration in siControl and siWNT5a transfected cells either non-infected (n= 150 cells, from 3 independent experiments) or expressing αCat-Vinc-HA (n= 150 cells, from 3 independent experiments). Data are mean ± SEM, p-values from unpaired t test compare siControl and siWNT5a groups.

Figure 9 - Wnt5a stabilizes vinculin at adherens junctions through a ROR2/Cdc42 pathway.

(A) Angular histograms showing the distribution of polarization angles from siControl (n= 11 images, from 6 independent experiments) and siROR2 (n= 11 images, from 6 independent experiments) transfected cells.

(B) Polarity index box plots from siControl (n= 11 images, from 6 independent experiments),

and siROR2 (n= 11 images, from 6 independent experiments) cells. p-values from unpaired t-test.

(C) Co-localization (%) between Vinculin/VE-Cadherin in siControl and siROR2 transfected cells (n= 9 images, from 3 independent experiments). Data are mean ± SD, p-values from unpaired t-test.

(D) Angular histograms showing the distribution of polarization angles of followers from wild type cells treated with either DMSO, iJNK (SP600125), iRac (NSC27632) or iCdc42 (ML141). n= 4 images, from 2 independent experiments.

(E) Angular histograms showing the distribution of polarization angles from siControl (n= 14 images, from 5 independent experiments) and siCdc42 (n= 11 images, from 5 independent experiments) transfected cells.

(F) Polarity index box plots from siControl (n= 14 images, from 5 independent experiments) and siCdc42 (n= 11 images, from 5 independent experiments) transfected cells. p-values from unpaired t-test.

(G) Co-localization (%) between vinculin-VE-cadherin (n= 8 images, from 3 independent experiments) in siControl and siCdc42 transfected cells. Data are mean ± SD, p-values from unpaired t-test.

(H) Detail of adherens junctions showing the association of actin stress fibers (phalloidin) to the adherens junctions (VE-Cadherin) of adjacent HUVECs in siCdc42
transfected cells. Nucleus labelled with Dapi. Scale bar, 20µm.

(I) Quantification of cell perimeter (%) composed of linear (blue), serrated (red) and reticular (green) in siControl and siCdc42 transfected cells (n= 78 and 75 cells, respectively, from 2 independent experiments). Data are mean ± SEM and p-values from unpaired t-test.

(J) Quantification of the number of actin stress fibers connected to VE-cadherin positive cell-cell junctions in siControl or siCdc42 treated cells. N= 7 images, from 3 independent experiments. Data are mean ± SD, and p-values from unpaired t-test.

(K) Pulldown of active GTP-bound Cdc42 in siControl and siROR2 transfected cells unstimulated or stimulated with recombinant human Wnt5a protein (rhWnt5a) (n=1).

(L) HUVEC expressing Cdc42-2G at adherens junction. Scale bar= 20µm.

(M) Box plots showing the number of Cdc42 FRET peaks per junction in siControl (n= 11 cell-cell interfaces, from 2 independent experiments) and siWNT5a (n=9 cell-cell interfaces, from 2 independent experiments) transfected cells. p-values from unpaired t-test.

(N) Box plots showing the number of Cdc42 FRET peaks per leading edge in siControl (n= 5 leading edges, from 2 independent experiments) and siWNT5a (n= 6 leading edges, from 2 independent experiments) transfected cells. p-values from unpaired t-test.

(O) Left: example of a mouse retina sprouting front treated with PBS and MI141 labeled for EC nuclei (Erg, green), lumen (Icam2, blue) and Golgi (Golph4, red). Right: higher

magnification of the sprouting front showing high cell polarity coordination in PBS treated retinas and poor cell polarity coordination in MI141 treated retinas. Scale bar, 200µm.
(P) Angular histograms showing the distribution of polarization angles of endothelial cells at the vascular sprouting front from mouse retinas treated with PBS (n= 4 retinas) or MI141 (n= 5 retinas).
(Q) Polarity index box plots of endothelial cells from mouse retinas treated with PBS (n= 4 retinas) or MI141 (n= 5 retinas). p-values from unpaired t-test.

Figure 10 – Schematic of the function of Wnt5a signaling in mechanocoupling at adherens junctions.
Working model for the role of non-canonical Wnt ligand WNT5a in mechanotransduction. Wnt5a, through ROR2, activates Cdc42 at adherens junctions, which is necessary for stable binding of vinculin to α-catenin, and efficient mechanocoupling between endothelial cells. Low non-canonical Wnt signaling weakens adherens junctions, impairs force propagation, and disrupts collective cell migration of endothelial cells.

Figure 11 – Validation of specificity of siRNAs used in this study.
(A) Quantification of mRNA expression levels by qPCR showing the knockdown efficiencies of siRNAs against CDC42, CDH5, CTNNA1, FZD4, FZD6, FZD7, FZD8, ROR1, ROR2, RYK, VCL, WNT5a and WNT11. Data are mean ± SD, gene expression levels were normalized to GAPDH.
(B) Western blot showing siRNA knockdown efficiency for α-Catenin (n= 2), VE-cadherin (n= 2), vinculin (n= 1) and Cdc42 (n= 1).

SUPLLEMENTAL FIGURE LEGENDS

Figure 1 - Figure Supplement 1 – WNT5a, not WNT11, regulates collective behavior in vitro.

(A) Angular histograms showing the distribution of polarization angles of leaders (light blue) and followers (dark blue) from siControl, siWNT5a, siWNT11 and siWNT5a+siWNT11 transfected cells. n= 2 independent experiments for all conditions.

(B) Angular histograms showing the distribution of polarization angles of leaders (light blue) and followers (dark blue) from siControl (n= 6 images, from 3 independent experiments) and siα-catenin (n= 4 images, from 2 independent experiments) transfected cells. p-values from unpaired t-test.

(C) Polarity index box plots of leaders (top) and followers (bottom) from siControl (n= 6 images, from 3 independent experiments) and siα-catenin (n= 4 images, from 2 independent experiments). p-values from unpaired t-test.

(D) Example of Lifeact-mCherry^{+} HUVEC extending cryptic lamellipodia under an adjacent cell labeled for nuclei (Dapi), tight junctions (ZO1) and actin (Lifeact-mCherry) (top) and the corresponding image segmentation with the cryptic lamellipodia in green, the cell body in blue and the axial polarity vector in black (bottom). Scale bar, 20μm.

(E) Cryptic lamellipodia polarity axis at the wound edge of migrating HUVECs was determined by calculating the angle of polarization (α) between the scratch edge and the polarity axis defined by a vector drawn from the center of the cell nucleus to the center of the cryptic lamellipodia (top). Angular histograms showing the polarity distributions of cryptic lamellipodia of Lifeact-mCherry^{+} cells from siControl (n= 44 cells, from 4 independent experiments) and siWNT5a (n= 37 cells, from 4 independent experiments) transfected cells.

Figure 7 - Figure Supplement 1 – Overexpression of exogenous vinculin isoforms rescues polarity defects of vinculin siRNA depleted cells.

(A) Angular histograms showing the distribution of polarization angles from siVinculin transfected cells expressing Vinculin-Full-Length-GFP (n= 4 images, 2 independent experiments) or Vinculin-T12-GFP (n= 4 images, 2 independent experiments).

(B) Polarity index box plots of siVinculin transfected cells non-infected (n= 4 images, 2 independent experiments) or infected with Vinculin-Full-Length-GFP (n= 4 images, 2 independent experiments) or Vinculin-T12-GFP (n= 4 images, 2 independent experiments). p-values from unpaired t-test.

Figure 7 - Figure Supplement 2 – Expression levels of exogenous vinculin isoforms in siControl and siWNT5a cells.

(A) Western blot for anti-GFP and α-tubulin in siControl and siWNT5a transfected cells, transduced or not transduced with corresponding lentiviral particles.

Figure 8 - Figure Supplement 1 – Overexpression of a-catenin-vinculin fusion protein rescues polarity defects of Wnt5a siRNA depleted cells.

(D) Western blot for anti-HA and α-tubulin in siControl and siWNT5a transfected cells, transduced or not transduced with corresponding lentiviral particles.

Figure 9 - Figure Supplement 1 – Polarity Indexes of endothelial cells depleted on specific receptors related to non-canonical Wnt signaling.

(A) Angular histograms showing the distribution of polarization angles of leaders (light blue) and followers (dark blue) from siControl (n= 5 independent experiments), siROR1 (n= 3 independent experiments), siFZD4 (n= 4 independent experiments), siFZD6 (n= 4 independent experiments), siFZD7 (n= 3 independent experiments), siFZD8 (n= 2 independent experiments) and siRYK (n= 4 independent experiments) transfected cells.

Video 1 – Localization of Cdc42-FRET sensor in wounded monolayers.

ECFP fluorescent signal from Cdc42-2G FRET sensor at the leading edge of siControl cells. Photobleaching effects were corrected using a FIJI plugin. Images were acquired for 5min with 1s time interval.

Video 2 – Highlight of Supplemental Video 1.

Crop from Supplemental Video 1, showing the ECFP fluorescent signal from the Cdc42-2G FRET sensor in an interface between leader and follower siControl cells. Photobleaching effects were corrected using a FIJI plugin. Images were acquired for 5min with 1s time interval.

Video 3 – Ratiometric FRET signal in Cdc42-2G sensor in siControl cells.

Ratiometric FRET signal from Cdc42-2G (blue scale) from Video 1, superimposed to the acceptor signal (grey scale) in siControl cells. Photobleaching effects were not corrected. Images were acquired for 5min with 1s time interval.

Video 4 – Ratiometric FRET signal in Cdc42-2G sensor in siWNT5a cells.

Ratiometric FRET signal from Cdc42-2G (blue scale) superimposed to the acceptor signal (grey scale) in siWNT5a cells. Photobleaching effects were not corrected. Images were acquired for 5min with 1s time interval.

MATERIALS AND METHODS

Key Resources Table

Reagent type (species) or resource	Designation	Source or reference	Identifiers	Additional information
strain, strain background (*Escherichia coli*)	Stbl3	Life Technologies	Cat#: C7373-03	Chemically Competent
genetic reagent (*Mus musculus*)	*Vcl* fl/fl::*Pdgfb*-iCreERT2	This paper		Generated from *Vcl* floxed crossed with *Pdgfb*-iCreERT2
genetic reagent (*Mus musculus*)	*Vcl* fl/fl	Zemljic-Harpf et al., 2007		Generated from *Vcl* floxed crossed with *Pdgfb*-iCreERT2
genetic reagent (*Mus musculus*)	*Pdgfb*-iCreERT2	(Claxton et al., 2008)		
genetic reagent (*Mus musculus*)	*Wnt5a* fl/fl	(Miyoshi et al., 2012)		
genetic reagent (*Mus musculus*)	*Wnt11* null	(Majumdar et al., 2003)		
genetic reagent (*Mus musculus*)	*Wnt5a* fl/fl::Wnt11 null::*Pdgfb*-iCreERT2	Franco et al. eLIFE 2016		
cell line (*Homo sapiens*)	HEK293T	ATCC	ATCC:CRL-3216; RRID:CVCL_0063	
cell line (*Homo sapiens*)	Human umbilical vein endothelial cells (HUVECs)	Lonza	Cat#: C2519A	Primary cell line
antibody	AffiniPureF(ab')2 fragments Donkey anti-rabbit IgG	Jackson ImmunoResearch	Cat#: 711-006-152; RRID:AB_2340586	IF(1:400)
antibody	Mouse anti-CD102	BD Biosciences	Cat#: 553326; RRID:AB_394784	IF(1:200)
antibody	Rabbit anti-CDC42	Cell Signaling	Cat#: 2466; RRID:AB_2078082	WB(1:1000)
antibody	Rabbit anti-Erg	Abcam	Cat#: ab92513; RRID:AB_2630401	IF(1:200)
antibody	Chicken anti-GFP	Aves Labs	Cat#: GFP-1010; RRID:AB_2307313	WB(1:2000)
antibody	Rabbit anti-GOLPH4	Abcam	Cat#: ab28049; RRID:AB_732692	IF(1:400)
antibody	Mouse anti-HA tag	BioLegend	Cat#: 901513; RRID:AB_2565335	IF(1:100), WB(1:500)
antibody	Rabbit anti-p120-Catenin	Merck Millipore	Cat#: 05-1567; RRID:AB_11213674	IF(1:100)
antibody	Goat anti-VE-Cadherin	Santa Cruz Biotechnologies	Cat#: sc-6458; RRID:AB_2077955	IF(1:100), WB(1:1000)
antibody	Mouse anti-VE-Cadherin	Santa Cruz Biotechnologies	Cat#: sc-9989; RRID:AB_2077957	IF(1:100)

antibody	Goat anti-VE-Cadherin	R&D Systems	Cat#: AF938; RRID:AB_355726	IF(1:100), WB(1:400)
antibody	Mouse anti-Vinculin	Sigma-Aldrich	Cat#: V9264; RRID:AB_10603627	IF(1:400), WB(1:400)
antibody	Rabbit anti-Vinculin	Sigma-Aldrich	Cat#: V4139; RRID:AB_262053	IF(1:100), WB(1:400)
antibody	Rabbit anti-ZO1	Invitrogen	Cat#: 402300; RRID:AB_2533457	IF(1:100)
antibody	Rat anti-α18	Prof. Dr. Masatoshi Takeichi (RIKEN, Kobe) shared resource		IF(1:20000)
antibody	Rabbit anti-α-Catenin	Sigma-Aldrich	Cat#: C2081; RRID:AB_476830	IF(1:200), WB(1:1000)
antibody	Mouse anti-α-Tubulin	Sigma-Aldrich	Cat#: T6199; RRID:AB_477583	IF(1:200), WB(1:2000)
antibody	Rabbit anti-β-Catenin	Sigma-Aldrich	Cat#: C2206; RRID:AB_476831	IF(1:100), WB(1:1000)
antibody	Mouse anti-γ-Tubulin	Sigma-Aldrich	Cat#: T6557; RRID:AB_477584	WB(1:2000)
antibody	Donkey anti-Chicken HRP	Jackson ImmunoResearch	Cat#: 703-035-155; RRID:AB_10015283	WB(1:5000)
antibody	Donkey anti-Goat Alexa 647	Thermo Fisher Scientific	Cat#: A21447; RRID:AB_2535864	IF(1:400)
antibody	Donkey anti-Goat HRP	Bethyl	Cat#: A50-201P ; RRID:AB_66756	WB(1:5000)
antibody	Donkey anti-Mouse Alexa 488	Thermo Fisher Scientific	Cat#: A21202; RRID:AB_141607	IF(1:400)
antibody	Donkey anti-Rabbit Alexa 568	Thermo Fisher Scientific	Cat#: A10042; RRID:AB_2534017	IF(1:400)
antibody	Donkey anti-Rabbit Alexa 488	Thermo Fisher Scientific	Cat#: A21206; RRID:AB_2535792	IF(1:400)
antibody	Donkey anti-Rabbit Alexa 647	Thermo Fisher Scientific	Cat#: A21447; RRID:AB_2535864	IF(1:400)
antibody	Goat anti-Rabbit HRP	Life Technologies	Cat#: G-21234	WB(1:5000)
antibody	Goat anti-Rat Alexa 555	Thermo Fisher Scientific	Cat#: A21434; RRID:AB_2535855	IF(1:400)
antibody	Phalloidin 488	Thermo Fisher Scientific	Cat#: A12379	IF(1:400)
antibody	Phalloidin 568	Thermo Fisher Scientific	Cat#: A12380	IF(1:200)
antibody	Sheep anti-Mouse HRP	GE Healthcare	Cat#: NA931V	WB(1:5000)
recombinant DNA reagent	pLenti-Cdc42-2G	Prof. Dr. Olivier Pertz (Institute of Cell Biology) shared resource	Addgene plasmid #68813; RRID:Addgene_68813	Lentiviral vector expressing a FRET sensor of active Cdc42

recombinant DNA reagent	Lifeact-mCherry	Prof. Dr. Edgar Gomes (Instituto de Medicina Molecular) shared resource		
recombinant DNA reagent	VE-Cad-TL	Prof. Martin Schwartz (Yale University) shared resource	Addgene plasmid #45849 pLPCX-VEcadTL; RRID:Addgene_45849	Lentiviral vector expressing a FRET VE-cadherin tailess tension sensor
recombinant DNA reagent	VE-Cad-TS	Prof. Martin Schwartz (Yale University) shared resource	Addgene plasmid #45848 pLPCX-VEcadTS; RRID:Addgene_45848	Lentiviral vector expressing a FRET VE-cadherin tension sensor
recombinant DNA reagent	Vinculin-Full Length-GFP	This paper	Addgene plasmid #46265 pEGFPC1/GgVcl 1-1066	Lentiviral vector expressing vinculin full-length tagged with GFP
recombinant DNA reagent	Vinculin-T12 mutant-GFP	This paper	Addgene plasmid #46266 pEGFPC1/GgVcl 1-1066 T12 mutant; RRID:Addgene_46266	Lentiviral vector expressing vinculin T12 mutant tagged with GFP
recombinant DNA reagent	αCat-Vinc-HA	This paper	Cloned in pUC57, General Biosytems	Lentiviral vector expressing a fusion protein containing the β-catenin binding domain of α-catenin and the actin-binding domain of vinculin tagged with HA
recombinant DNA reagent	Wnt5a-V5	This paper		Lentiviral vector expressing Wnt5a tagged with V5
recombinant DNA reagent	pLX303	Addgene	Cat#: 25897; RRID:Addgene_25897	Lentiviral backbone
sequence-based reagent	RT-qPCR primers	This paper		See Supplementary file 1
sequence-based reagent	ON-TARGET human siRNAs	Dharmacon		See Supplementary file 1
peptide, recombinant protein	Recombinant human Wnt5a protein	R&D Systems	Cat#: 645-WN	
commercial assay or kit	BCA protein assay kit	VWR	Cat#: 786-0000	
commercial assay or kit	Cdc42 Pull-down Activation Assay Biochem Kit	Cytoskeleton	Cat#: BK034	
commercial assay or kit	Duolink® In Situ Red Mouse/Rabbit Starter Kit	Sigma-Aldrich	Cat#: DUO92101	

commercial assay or kit	ECL™ Western Blotting Detection Reagent	GE Healthcare	Cat#: RPN2232	
commercial assay or kit	GeneJet RNA Purification Kit	Thermo Fisher Scientific	Cat#: K0731	
commercial assay or kit	RNeasy Mini Kit	Qiagen	Cat#: 74104	
commercial assay or kit	Superscript IV First-Strand Synthesis System	Invitrogen	Cat#: 18091050	
chemical compound, drug	Dabco (1,4-Diazabicyclo[2.2.2]octane)	Sigma-Aldrich	Cat#: D27802	
chemical compound, drug	DharmaFECT 1 reagent	Dharmacon	Cat#: T-2001-02	
chemical compound, drug	DNase I	NZYTech	Cat#: MB19901	
chemical compound, drug	DSP (dithiobis(succinimidyl propionate))	Alfagene	Cat#: 22585	
chemical compound, drug	Fibronectin	Sigma-Aldrich	Cat#: F1141	
chemical compound, drug	Full Range Rainbow Recombinant protein Molecular weight marker	GE Healthcare	Cat#: RPN800E	
chemical compound, drug	Gelatin	Sigma-Aldrich	Cat#: G1393	
chemical compound, drug	ML-141	Sigma-Aldrich	Cat#: SML0407	10 µM
chemical compound, drug	Mowiol	Sigma-Aldrich	Cat#: 81381	
chemical compound, drug	NSC 23766	Tocris	Cat#: 2161	100 µM
chemical compound, drug	Phosphatase and proteinase inhibitors cocktail	Thermo Fisher Scientific	Cat#: 1861281	
chemical compound, drug	Pierce G-protein agarose beads	Thermo Fisher Scientific	Cat#: 22851	
chemical compound, drug	Ponceau Red	NZYTech	Cat#: MB19201	
chemical compound, drug	Power SYBR Green PCR Master Mix	Thermo Fisher Scientific	Cat#: 4368706	
chemical compound, drug	SP600125	Tocris	Cat#: 1496	10 µM
chemical compound, drug	Tamoxifen	Sigma-Aldrich	Cat#: H7904	
chemical compound, drug	4x Laemmli Sample Buffer	Bio-Rad	Cat#:161-0747	

software, algorithm	Adobe photoshop	Adobe Photoshop (https://www.adobe.com/products/photoshop.html)	RRID:SCR_014199	Version CS4
software, algorithm	Biosensor Processing	(Hodgson et al., 2010)		Version 2.1
software, algorithm	Cell image velocimetry (CIV)	(Milde et al., 2012)		
software, algorithm	Chemotaxis and Migration Tool	Chemotaxis and Migration Tool (https://ibidi.com/chemotaxis-analysis/171-chemotaxis-and-migration-tool.html)		Version 2.0
software, algorithm	GraphPad Prism	GraphPad Prism (https://graphpad.com)	RRID:SCR_015807	Version 7
software, algorithm	ImageJ	ImageJ (http://imagej.nih.gov/ij/)	RRID:SCR_003070	
software, algorithm	Image Lab	Image Lab (http://www.bio-rad.com/en-us/sku/1709690-image-lab-software)	RRID:SCR_014210	Version 6.0.1
software, algorithm	Matlab script used for immunostaining co-localization analysis	This paper		
software, algorithm	Matlab script used for automated polarity analysis	This paper		Modified version of polarity analysis script from Dr. Anne-Clémence Vion and Dr. Holger Gerhardt (Max-Delbruck Center)
software, algorithm	Matlab script used for FRET analysis	This paper		
software, algorithm	Matlab script used for statistical analysis	Matlab (http://www.mathworks.com/products/matlab/)	RRID:SCR_001622	
software, algorithm	MetaMorph	MetaMorph (http://www.moleculardevices.com/Products/Software/Meta-Imaging-Series/MetaMorph.html)	RRID:SCR_002368	
software, algorithm	Velocity spatial correlation	(Petitjean et al., 2010)		

software, algorithm	Zen	Zen (http://www.zeiss.com/microscopy/en_us/products/microscope-software/zen.html#introduction)	RRID:SCR_013672	
other	DAPI stain	Sigma-Aldrich	Cat#: D9542	

Mice and treatments

For the Cdc42 inhibition experiment, C57BL/6J mice were maintained at the Instituto de Medicina Molecular (iMM) under standard husbandry conditions and under national regulations. ML-141 (SML0407, Sigma, Germany) was injected twice (morning and evening) intraperitoneally (IP) (20 ml/g of 1 mg/mL solution) at postnatal day 5 (P5) before eyes were collected at P6.

Vinculin floxed mouse (Zemljic-Harpf et al., 2007) was obtained from Robert S. Ross *Pdgfb*-iCreERT2 (Claxton et al., 2008) to generate a new *Vinculin* fl/fl::Pdgfb-iCreERT2 mouse line. Mice were maintained at the Instituto de Medicina Molecular (iMM) under standard husbandry conditions and under national regulations. Animal procedures were performed under the DGAV project license 0421/000/000/2016. Tamoxifen (Sigma, Germany) was injected intraperitoneally (IP) (20 ml/g of 1 mg/mL solution) at postnatal day 1 (P1) and P3 before eyes were collected at P6.

For Figure1, we re-used mouse retinas previously collected (Franco et al., 2016). For clarity, we transcribe the specificities of the breedings and experimental conditions. The following mouse strains were previously used: *Pdgfb*-iCreERT2 (Claxton et al., 2008); *Wnt5a* floxed (Miyoshi et al., 2012); *Wnt11* null (Majumdar et al., 2003). Mice were maintained at the London Research Institute under standard husbandry conditions. Tamoxifen (Sigma, Germany) was injected intraperitoneally (IP) (20 ml/g of 1 mg/mL solution) at postnatal day 2 (P2) before eyes were collected at P5 onwards. Animal procedures were performed in accordance with the Home Office Animal Act 1986 under the authority of project license PPL 80/2391.

Immunofluorescence on mouse retinas

Eyes were collected at P6 and fixed with 2% PFA in PBS for 5 hr at 4˚C, thereafter retinas were dissected in PBS. Blocking/permeabilisation was performed using Claudio's Blocking Buffer (CBB) (Franco et al., 2013), consisting of 1% FBS (Thermo Fisher Scientific), 3% BSA (Nzytech), 0.5% triton X100 (Sigma), 0.01% Na deoxycholate (Sigma), 0,02% Na Azide (Sigma) in PBS pH = 7.4 for 2 hr in a rocking platform. Primary antibodies (Anti-CD102 and Anti-Erg) were incubated at the desired concentration (see Key Resources Table) in 1:1 CBB:PBS at 4˚C overnight in a rocking platform and afterwards washed 3 x 60min in PBS-T. Then, retinas were incubated in 1:1 CBB:PBS solution containing the secondary fluorophore conjugated antibodies at 4ºC overnight in the dark. Next, and due to the fact that we are using same species primary antibodies, retinas were incubated with AffiniPureF(ab')$_2$ fragments Donkey anti-rabbit IgG (see Key Resources Table) for 2 hrs at RT, followed by 3 washes of 30min in PBS-T. Retinas were fixed with 4%PFA in PBS at RT and blocked using CBB and primary antibody (Anti-GOLPH4) was incubated (see Key

Resources Table) in 1:1 CBB:PBS at 4˚C overnight in a rocking platform. Secondary antibody was done as previously described. Retinas were mounted on slides using Vectashield mounting medium (Vector Labs, H-1000, Burlingame, California, USA). For polarity quantification, a tile-scan spanning the sprouting front was acquired on a Zeiss Cell Observer Spinning Disk microscope, equipped with the Zen software with a Plan-Apochromat 40x/1.4 Oil DIC M27 objective.

Culture of HUVECs

Human umbilical vein endothelial cells (HUVECs) were routinely cultured following the manufacturer's guidelines, in filter-cap T75 flasks Nunclon ∆ surface treatment (VWR international, LLC) and cultured at 37ºC and 5% CO_2 to ensure a stable environment for optimal cell growth. HUVECs (C2519A, Lonza) were cultured with complete medium EGM-2 Bulletkit (CC-3162, Lonza) supplemented with 1% penicillin/streptomycin (#15140122, Gibco). When passaging cells for experiments, cells were washed twice in sterile PBS (137mM NaCl, 2.7mM KCl, 4.3mM Na_2HPO_4, 1.47mM KH_2PO_4, pH7.4). Then, cells were incubated for 3-5min in trypsin/EDTA (#15400054, Gibco) or in TrypLE™ Express (#12605-028, Gibco) at 37ºC, 5% CO_2. When 95% of the cells detached, complete medium was added to each flask to inhibit the activity of the trypsin/EDTA or TrypLE™ Express and the cell suspension was transferred to a falcon tube. To maximize the amount of cells collected, all flasks were washed again with complete medium, which was added to the cell suspension gathered previously. HUVECs were then centrifuged at 115g for 5min at room temperature. The pellet was re-suspended in fresh complete medium. The cell concentration present in the suspension was determined using a Neubauer Chamber Cell Counting (Hirschmann EM Techcolor). All cells were then seeded on the desired culture vessels at 200.000–300.000 cells/mL and placed in the incubator. All experiments with HUVECs were performed between passages 3 and 6.

siRNA transfection

In order to silence the expression of genes of interest, a set of ON-TARGET human siRNAs were purchased from Dharmacon (see Table 1). Briefly, HUVECs were seeded the day before the transfection to reach 60-70% confluence and were then transfected with 25nM of siRNA using the DharmaFECT 1 reagent (Dharmacon, GE Healthcare) following the Dharmacon siRNA Transfection Protocol. 24h after transfection the culture medium was replaced by fresh complete medium and cells were kept under culture conditions up until 72h post-transfection and then processed for further experiments. siRNA efficiencies were measure by qPCR and by WB when antibodies were available (Figure 11).

RNA extraction and quantitative Real-Time PCR

RNA extraction was performed from HUVECs seeded on 12-well plates using the RNeasy Mini Kit (Qiagen) and the GeneJet RNA Purification Kit (Thermo Scientific) as described by the manufacturer's protocol. RNA concentration was quantified using NanoDrop 1000 (Thermo Scientific) and adjusted equally, followed by DNase I digestion (Thermo Scientific) and cDNA synthesis (Superscript IV First-Strand Synthesis System, Invitrogen). cDNA samples were then diluted in RNAse/DNAse-free water for the subsequent quantitative real-time PCR (RT-qPCR) reactions. RT-qPCR was performed using a 7500 Fast Real-Time PCR System (Applied Biosystems) with Power SYBR Green PCR Master Mix (Applied Biosystems) following the standard program of the system previously mentioned. For each reaction, 5μL of cDNA was combined with 10μL of Power SYBR Green PCR Master Mix, 4.5μL of RNAse/DNAse free water and 0.5μL of 4μM primers pool (Forward+Reverse) (see Table 1) in a MicroAmp Fast Optical 96-well Reaction Plate (Applied Biosystems). The expression levels of each sample duplicate were then normalized to GAPDH and the $2^{-\Delta\Delta T}$ method was used to calculate relative alterations in gene expression (Fig.11).

Protein extraction and Western Blotting

Protein extraction was performed from HUVECs seeded on 6-well plates which were lysed in 120μL of RIPA buffer (50mM Tris/HCl pH7.5, 1% NP-40, 150mM NaCl, 0.5% sodium deoxycholate, 0.1% SDS in H_2O) supplemented with phosphatase and proteinase inhibitors cocktail (1:100, #10085973 Fischer Scientific). Adherent cells were then detached from the plate with a cell scrapper and the cell lysates were gathered and transferred into an ice cold eppendorf tube. The cell lysates were then centrifuged at maximum speed for 10min at 4ºC and the supernatants collected into a new eppendorf tube. Protein concentration was quantified using the BCA protein assay kit (Pierce) following the guidelines recommended by the manufacturer. The Multimode microplate reader, Infinite M200 (Tecan), was used for spectrophotometric measurement of protein with the i-control™ software. For Western Blotting protein samples were normalized up to 25μL and combined with a mixture of 2x Laemmli Sample Buffer (#161-0747, Bio-rad Laboratories) with 450mM DTT (D0632, Sigma-Aldrich) and incubated at 70ºC in a Dry Block Thermostat (Grant Instruments, Ltd) for 10min (or 95ºC for 5min). Protein samples were loaded and separated on a 4-15% Mini-PROTEAN® TGX™ Gel (#456-1084, BioRad) along with 5μL of protein ladder (Full-Range RPN800E, GE Healthcare Rainbow Molecular Weight Markers), first at 50V for 5min and then at 100-130V for

1-2h in SDS-PAGE running buffer (10x SDS-PAGE: 250mM Tris, 1.92M Glycine, 1% SDS, pH8.3).

Gels were then transferred either onto a nitrocellulose membrane (iBlot Transfer Stack Regular/Mini size, #IB3010-01/-02, Invitrogen) with iBlot Dry Blotting System (Invitrogen) for 4–7min; or onto a Polyvinylidene Difluoride (PVDF) membrane (#IPVH00010, Merck Milipore) with Mini Trans-Blot® Electrophoretic Transfer Cell (Biorad) following the manufacturer's guidelines. After transfer, blotted membranes were incubated in Ponceau Red to assess transfer quality, and then washed in TBS-T (50mM Tris/HCl, 150mM NaCl, 0.1% Tween-20, pH7.5). Then, membranes were incubated in blocking buffer containing 3% BSA (Bovine Serum Albumin, MB04602, Nzytech) in TBS-T for 1h at RT, followed by an overnight incubation at 4ºC with the primary antibodies diluted in the same blocking buffer (see Key Resources Table).

On the following day membranes were washed 3 times in TBS-T and incubated in blocking buffer containing the secondary horseradish peroxidase (HRP) conjugated antibodies for 1h at RT (see Key Resources Table).

Before revelation membranes were washed again 3 times in TBS-T for 5min and then incubated in ECL™ Western Blotting Detection Reagent (RPN2209, GE Healthcare) following the manufacturer's protocol.

Protein bands were visualized in Chemidoc XRS+ and relative protein quantities were measured using the Image Lab software, both from Bio-Rad Laboratories. All results were normalized to tubulin levels.

Pulldown of active GTP-bound Cdc42

Active Cdc42 pulldown was performed from HUVECs cultured in 10cm plates non-stimulated or stimulated with recombinant human Wnt5a protein (645-WN, R&D Systems, 200ng/mL) for 15min using the Cdc42 Pull-down Activation Assay Biochem Kit (Cytoskeleton) as described by the manufacturer's protocol. Briefly, after stimulation, cells were washed with ice cold PBS, scrapped and lysed in lysis buffer containing protease and phosphatase inhibitors. After lysate clarification, inputs from all the samples were gathered and the remaining lysate was used for the pulldown reaction. 10µg of PAK-PBD beads were added to equivalent protein amounts of cell lysates (300 µg) for each condition. The mixture was then incubated for 1h at 4ºC with gentle rotation. After the pulldown reaction, beads were washed 3 times in washing buffer and the bound protein complexes were eluted in sample buffer with DTT by placing the beads for 5min at 95ºC. Samples were then blotted on SDS-PAGE following standard protocols.

Immunoprecipitation

VE-cadherin and vinculin immunoprecipitation was performed from HUVECs cultured in 10cm plates. After the scratch-wound assay, cells were incubated with PBS supplemented with 1mM $CaCl_2$ and 0.5mM DSP (#22585, Thermo Scientific) for 20min at RT. Afterwards they were washed twice with ice cold PBS and then four times with ice cold quenching buffer (10mM Tris/HCl, pH 7.5, in PBS). Then, cells were scrapped and lysed in lysis buffer (25mM Tris/HCl, pH 7.5, 1% NP-40, 1% deoxycholic acid, 150mM NaCl) containing protease and phosphatase inhibitors. Cell lysates were centrifuged at 16,100g for 10min at 4ºC and the pellet digested in SDS IP buffer (15mM Tris/HCl, pH 7.5, 5mM EDTA, 2.5mM EGTA, 1% SDS). Samples were then incubated for 10min at 100ºC and diluted in lysis buffer. At this point, inputs from all the samples were gathered and the remaining lysate was used for immunoprecipitation. Pre-washed Pierce® G-protein agarose beads (#22851, Thermo Scientific) were added to equivalent protein amounts of cell lysates (100-200µg) for each condition, containing either 2µg of anti-vinculin (V9264, Sigma-Aldrich) or anti-VE-cadherin (sc-9989, Santa Cruz Biotechnologies) antibody. The mixture was then incubated overnight at 4ºC with gentle rotation. After immunoprecipitation, beads were washed 4 times in ice cold lysis buffer and the bound protein complexes were eluted in sample buffer with DTT by placing the beads for 10min at 100ºC. Samples were then blotted on SDS-PAGE following standard protocols.

Immunofluorescence

For immunofluorescence of *in vitro* cultured HUVECs, cells were seeded on 24-well plates with glass coverslips, or in 8-well Ibidi slides (80826, Ibidi) previously coated with 0.2% Gelatin in sterile water (G1393, Sigma-Aldrich) or with Fibronectin in PBS (F1141, Sigma-Aldrich), respectively. After the scratch-wound assay (described above), HUVECs were fixed in 1% Paraformaldehyde (PFA) supplemented with 1M $MgCl_2$ and 1M $CaCl_2$ (1µL/2mL) in PBS for 30min at RT. Cells were then washed with PBS to remove the remaining PFA and the immunostaining protocol initiated. When the PBS was removed, HUVECs were blocked and permeabilized with blocking solution containing 3% BSA in PBS-T (PBS with 0.1% Triton X-100) for 30min at RT. Then cells were incubated for 2h at RT with the primary antibodies diluted in the blocking solution (see Key Resources Table) and washed 3 x 15min washes in PBS-T. Afterwards, cells were incubated in blocking solution containing the secondary fluorophore conjugated antibodies for 1h at RT in the dark, followed again by 3 washes of 15min in PBS-T. Finally, HUVECs were incubated with 1x DAPI (D1306, Molecular Probes by Life Technologies) diluted in PBS-T for 5min in the dark. Coverslips were then mounted on microscopy glass slides using Mowiol DABCO

(Sigma-Aldrich), while for the 8-well Ibidi slides 50µL of Mowiol DABCO was added to each well. To quantify co-localization of junctional molecules, high-resolution Z-stack images at multiple positions on the scratch front were acquired on a confocal Laser Point-Scanning Microscope 880 (Zeiss) equipped with the Zen black software with a Plan Apochromat 63x NA 1.40 oil DIC M27 objective. For polarity quantification, a tile-scan spanning the entire region of the scratch was acquired on a motorized inverted widefield fluorescence microscope, Zeiss Axiovert 200M (Carl Zeiss) equipped with the Metamorph software with an EC Plan-NeoFluar 40x NA 0.75 dry objective.

Immunostaining co-localization analysis

For co-localization analysis, high-resolution Z-stack confocal images of HUVECs stained for junctional proteins (VE-Cadherin, Vinculin, α-catenin, β-catenin and p120-catenin) were imported and analyzed in MATLAB using a custom written code (source code file 1). An object-based co-localization approach was used. Briefly, each channel was segmented and a binary mask was generating. The masks were combined and the fraction of pixels with overlapping signals was quantified.

Calcium switch assay

Confluent HUVECs seeded on 24-well plates were subjected to the scratch-wound assay and then incubated for 15min in Ca2+ free HBSS, followed by DMEM (#41966-029, Gibco) supplemented with 1% penicillin/streptomycin (#15140122, Gibco), 10% fetal bovine serum (FBS) (#10500-064, Gibco) and 2mM Ca^{2+} from 1 up to 30min at 37ºC, 5% CO_2. Afterwards, cells were immediately fixed in 1% Paraformaldehyde (PFA) supplemented with 1M $MgCl_2$ and 1M $CaCl_2$ (1µL/2mL) and processed for immunostaining.

Proximity ligation assay (PLA)

Confluent HUVECs seeded on 24-well plates were subjected to the scratch-wound assay and then processed for PLA using the Duolink® In Situ Red Mouse/Rabbit Starter Kit (DUO92101-1KT, Sigma-Aldrich) as described by the manufacturer's protocol. To probe interactions between vinculin and VE-cadherin, cells were incubated with an anti-vinculin antibody raised in rabbit (V4139, Sigma-Aldrich) and an anti-VE-cadherin antibody raised in mouse (sc-9989, Santa Cruz Biotechnologies). In parallel, cells were also incubated with an anti-VE-cadherin antibody raised in goat (AF938, R&D Systems) and subsequently with an anti-Goat fluorescent-conjugated secondary antibody (A21447, Thermo Fisher Scientific) to label adherens junctions. To quantify co-localization of PLA signal at adherens junctions, high-resolution Z-stack images at multiple positions on the wound edge were

acquired on a confocal Laser Point-Scanning Microscope 880 (Zeiss) equipped with the Zen black software with a Plan Apochromat 63x NA 1.40 oil DIC M27 objective. Briefly, PLA dots were quantified only at adherens junctions, using a similar approach to the co-localization studies described in the section “Immunostaining co-localization analysis”, using the VE-cadherin immunofluorescence staining to detect overlapping pixels between junctions and PLA signals.

Viral production and transduction

Replication-incompetent lentiviruses were produced by transient transfection of HEK293T of pLX303 lentiviral expression vector co-transfected with the viral packaging vector Δ8.9 and the viral envelope vector VSVG. Medium was replaced with fresh culture medium 6-8h post transfection. 48h after medium replacement, lentiviral particles were concentrated from supernatant by ultracentrifugation at 90000g for 1h30 and re-suspended in 0.1% BSA PBS. Seeded HUVECs were transduced 24h post-transfection with varying concentrations of lentiviral plasmids containing VE-Cad-TS, VE-Cad-TL, Cdc42-2G, Vinculin-Full-Length-GFP, Vinculin-T12-mutant-GFP and αCat-Vinc-HA fusion protein sequences (see Key Resources Table). 24h after viral transduction the culture medium was replaced by fresh complete medium and cells were kept under culture conditions up until 48h post-transduction and then processed for immunofluorescence or imaging. In the analysis, we used a mix population containing transduced and non-transduced cells, selecting areas where high transduction efficiencies were observed.

Scratch-wound assay and drug treatments

To assess functional collective cell behaviour properties (*i.e.*, polarity and migration), as well as morphological features of *in vitro* cultured HUVECs, we used the scratch-wound assay. The wound was created by scratching the surface of a well-plate or a microscopy glass slide containing a monolayer of adherent HUVECs with a 200µL pipette tip. The culture medium was then replaced by fresh complete medium and HUVECs were allowed to migrate under optimal physiological conditions. When appropriate, drugs of interest were added to the medium. (see Key Resources Table). Cells migrated for 5 hours after the wound, were fixed and then stained for immunofluorescence experiments. For live imaging experiments HUVECs migration was followed up to 16h. Imaging was performed using a Zeiss Cell Observer SD (Carl Zeiss) equipped with an EC Plan-Neofluar 10x NA 0.3 PH1. To track individual cells within the monolayer more efficiently using the cell nuclei as reference, HUVECs were incubated in 1x Hoechst for 15min at 37ºC before the onset of the time lapse. Images of the scratch front were acquired at multiple positions every 10min.

Analysis of migration, including wound closure, cell speed and straightness was performed using FIJI TrackMate plug in and the Chemotaxis and Migration Tool (free software from Ibidi).

Particle image velocimetry (PIV) analysis

The velocity field of the moving cell sheet was calculated in Matlab using cell image velocimetry (CIV) (Milde et al., 2012) software. Interrogation windows were set to 64x64 pxls with a 50% overlap. Velocity spatial correlation was calculated in Matlab using the x-component of the velocity as in (Petitjean et al., 2010). Correlation length was determined from exponential fitting of correlation curves.

Atomic force microscopy (AFM)

HUVECs were re-plated onto 35mm Petri dishes (TPP) 48h post-transfection from 6-well plates (on a ratio of 1 6-well plate to 2 35mm Petri dishes per condition) to attain a confluence of 60-70%. On the following day, 1h before starting the cell-cell adhesion measurements, the culture medium was replaced by PBS in one of the 35mm Petri dish replicates, to ensure cell detachment. 5min before the experiment, the culture medium of the other 35mm Petri dish replicate was replaced with serum free culture medium. An atomic force microscope NanoWizard II (JPK Instruments, Berlin, Germany) mounted on the top of an Axiovert 200 inverted microscope (Carl Zeiss, Jena, Germany) was used for the cell-cell adhesion measurements. For these experiments, tipless arrow TL1 cantilevers (Nanoworld, Neuchatel, Switzerland) were used, with a nominal spring constant of 0.03N m^{-1}, as described previously (Ribeiro et al., 2016). Cantilevers were cleaned for 15 min with UV light and coated with poly-D-lysine (50 µg ml^{-1}) for at least 30 min. Cantilevers were stored in poly-D-lysine solution until use.

After that, a set of adherent cells from the other Petri dish were selected to perform the cell-cell adhesion measurements, composed of 5 force-distance curves performed on each cell, with a cell-cell contact time of 5s and a 5s pause between them. Cell–cell contact was established with an applied force of 300 pN, at a constant height and in closed-loop mode. The AFM tip resonant frequency was maintained at 2 Hz, with a z-range displacement of 50 µm. For the internal negative controls, we used 4mM EGTA, a Ca^{2+} chelating agent that is able to sequestrate calcium ions from cadherins and render them inactive and unresponsive to force transmission. EGTA was added to the serum free culture medium of the Petri dish containing the adherent cells at the time of the recordings.

Analysis of Tension sensors FRET measurements

FRET images were obtained using a confocal Laser Point-Scanning Microscope 880 (Zeiss) equipped with a Plan-Apochromat 63x, NA 1.40, oil immersion, DIC M27 objective and an argon laser featuring 405, 458 and 514nm laser lines. For FRET experiments, it was used a MBS 458/514 beam splitter in combination with the following filters: mTFP1 GaAsP, band-pass 461–520; Venus/FRET, band-pass 525–575. Acceptor photobleaching experiments were analyzed using a custom written Matlab script (source code file 2). A Gaussian filter with standard deviation of 0.75 was applied to the images before analysis. The intensity in the region of interest was measured before and after bleaching. FRET efficiency was calculated as $EF = \frac{I_{post} - I_{pre}}{I_{post}}$ where I_{post} and I_{pre} are the intensity of the donor channel after and before bleaching respectively.

Analysis of CDC42 biosensor data

The CDC42-2G FRET biosensor activity was obtained using a widefield fluorescence microscope Axio Observer (Zeiss) equipped with a Plan-Apochromat 63x, NA 1.40, oil immersion, DIC M27 objective. For ratiometric FRET experiments we used the following excitations and emission filters: ET436/20 and ET480/40 for ECFP; ET500/20 and ET535/30 for EYFP (Chroma Technology Corp) and the images for each condition were acquired during 5min with 1s time interval. FRET experiments were performed as described by Louis Hodgson. Analysis of ratiometric FRET biosensor was performed in Matlab and the preprocessing was performed using the Biosensor Processing 2.1 software package from the Danuser lab (Hodgson et al., 2010).

The resulting images showing the localized activation of CDC42 were further processed to retrieve quantitative information from such maps. Briefly, junctional or free-edges regions were selected from each time lapse-image and the differential of the intensity vs time traces was calculated. For each image a region where no activation was detected was also selected to determine the level of background signal. The local maxima for each curve above background level were determined. Maxima found within three frames from each other were assumed to correspond to the same activation event.

Polarity index calculation

To quantify cell polarity, tile-scan images of HUVECs stained with Golgi (Golph4) and nuclear (DAPI) markers were processed on Adobe Photoshop to separate leader cells, identified as the first row of cell directly in contact with the scratch, from follower cells, comprising the second to fourth rows of cells away from the scratch. Afterwards, each set of images was imported and analyzed in MATLAB using a modified version of a polarity analysis script kindly provided by Anne-Clémence Vion and Holger Gerhardt. Briefly, after

segmenting each channel corresponding to the Golgi and nuclear staining, the centroid of each organelle was determined and a vector connecting the center of the nucleus to the center of its corresponding Golgi apparatus was drawn. The Golgi-nucleus assignment was done automatically minimizing the distance between all the possible couples. The polarity of each cell was defined as the angle between the vector and the scratch line. An angular histogram showing the angle distribution was then generated. Circular statistic was performed using the Circular Statistic Toolbox.

To test for circular uniformity, we applied the polarity index (PI), calculated as the length of mean resultant vector for a given angular distribution (Fig. 1D).

$$PI = \sqrt{\left(\frac{1}{N}\sum_{1}^{N}\cos\alpha\right)^2 + \left(\frac{1}{N}\sum_{1}^{N}\sin\alpha\right)^2}$$

PI corresponds to length of the mean resultant vector, previously described in Berens et al. (Berens, 2009). The PI varies between 0 and 1. The closer to 1 the more the data are concentrated around the mean direction, while values close to 0 corresponds to random distribution. PI indicates the collective orientation strength of the cell monolayer. Box plots were generated by using every single PI calculated for images of each biological replica, which show the biological variability of the system. This data is used to calculate the significance of differences between experimental conditions.

To obtain a global description of a given experimental condition, we pooled together all the different biological replica in one single file and calculate a global PI and mean angle (angular histograms and values below in the main text). This representation provides information on the general distribution of polarities in all experiments, and provides a mean angle of polarity, which is important

To calculate the PI as a function of distance, each image was divided starting from the wound edge in slices 50μm apart. The cell polarity within each slice was extracted and represented as angular histogram and the corresponding PI was calculated. For Fig.1E, a global polarity index was calculated merging together the results from different images from the same experimental conditions. N= 9 for siControl, N= 10 for siWNT5a and N= 4 for siCtnna1.

Statistical analysis

All statistical analysis was performed using GraphPad Prism 7 and Matlab (Mathworks). Statistical details of experiments are reported in the figures and figure legends. Sample size is reported in the figure legends and no statistical test was

used to determine sample size. The biological replicate is defined as the number of cells, images, animals, as stated in the figure legends. No inclusion/exclusion or randomization criteria were used and all analysed samples are included. Comparisons between two experimental groups were analyzed with unpaired parametric t test, while multiple comparisons between more than two experimental groups were assessed with one-way ANOVA. We considered a result significant when $p < 0.05$. Box plots for polarity indexes represent min to max, central line represents mean.

REFERENCES

Alatortsev, V.E., Kramerova, I.A., Frolov, M.V., Lavrov, S.A., and Westphal, E.D. (1997). Vinculin gene is non-essential in Drosophila melanogaster. FEBS Lett *413*, 197-201.

Barry, D.M., Xu, K., Meadows, S.M., Zheng, Y., Norden, P.R., Davis, G.E., and Cleaver, O. (2015). Cdc42 is required for cytoskeletal support of endothelial cell adhesion during blood vessel formation in mice. Development *142*, 3058-3070.

Bazellieres, E., Conte, V., Elosegui-Artola, A., Serra-Picamal, X., Bintanel-Morcillo, M., Roca-Cusachs, P., Munoz, J.J., Sales-Pardo, M., Guimera, R., and Trepat, X. (2015). Control of cell-cell forces and collective cell dynamics by the intercellular adhesome. Nat Cell Biol *17*, 409-420.

Berens, P. (2009). CircStat: A MATLAB Toolbox for Circular Statistics. Journal of Statistical Software *Vol 31*

Broman, M.T., Kouklis, P., Gao, X., Ramchandran, R., Neamu, R.F., Minshall, R.D., and Malik, A.B. (2006). Cdc42 regulates adherens junction stability and endothelial permeability by inducing alpha-catenin interaction with the vascular endothelial cadherin complex. Circ Res *98*, 73-80.

Buckley, C.D., Tan, J., Anderson, K.L., Hanein, D., Volkmann, N., Weis, W.I., Nelson, W.J., and Dunn, A.R. (2014). Cell adhesion. The minimal cadherin-catenin complex binds to actin filaments under force. Science *346*, 1254211.

Claxton, S., Kostourou, V., Jadeja, S., Chambon, P., Hodivala-Dilke, K., and Fruttiger, M. (2008). Efficient, inducible Cre-recombinase activation in vascular endothelium. Genesis *46*, 74-80.

Cohen, D.M., Chen, H., Johnson, R.P., Choudhury, B., and Craig, S.W. (2005). Two distinct head-tail interfaces cooperate to suppress activation of vinculin by talin. J Biol Chem *280*, 17109-17117.

Conway, D.E., Breckenridge, M.T., Hinde, E., Gratton, E., Chen, C.S., and Schwartz, M.A. (2013). Fluid shear stress on endothelial cells modulates mechanical tension across VE-cadherin and PECAM-1. Curr Biol *23*, 1024-1030.

Das, T., Safferling, K., Rausch, S., Grabe, N., Boehm, H., and Spatz, J.P. (2015). A molecular mechanotransduction pathway regulates collective migration of epithelial cells. Nat Cell Biol *17*, 276-287.

Dubrac, A., Genet, G., Ola, R., Zhang, F., Pibouin-Fragner, L., Han, J., Zhang, J., Thomas, J.L., Chedotal, A., Schwartz, M.A.*, et al.* (2016). Targeting NCK-Mediated Endothelial Cell Front-Rear Polarity Inhibits Neovascularization. Circulation *133*, 409-421.

Etienne-Manneville, S., and Hall, A. (2001). Integrin-mediated activation of Cdc42 controls cell polarity in migrating astrocytes through PKCzeta. Cell *106*, 489-498.

Etienne-Manneville, S., and Hall, A. (2003). Cdc42 regulates GSK-3beta and adenomatous polyposis coli to control cell polarity. Nature *421*, 753-756.

Fantin, A., Lampropoulou, A., Gestri, G., Raimondi, C., Senatore, V., Zachary, I., and Ruhrberg, C. (2015). NRP1 Regulates CDC42 Activation to Promote Filopodia Formation in Endothelial Tip Cells. Cell Rep *11*, 1577-1590.

Franco, C.A., Blanc, J., Parlakian, A., Blanco, R., Aspalter, I.M., Kazakova, N., Diguet, N., Mylonas, E., Gao-Li, J., Vaahtokari, A.*, et al.* (2013). SRF selectively controls tip cell invasive behavior in angiogenesis. Development *140*, 2321-2333.

Franco, C.A., Jones, M.L., Bernabeu, M.O., Geudens, I., Mathivet, T., Rosa, A., Lopes, F.M., Lima, A.P., Ragab, A., Collins, R.T.*, et al.* (2015). Dynamic endothelial cell rearrangements drive developmental vessel regression. PLoS Biol *13*, e1002163.

Franco, C.A., Jones, M.L., Bernabeu, M.O., Vion, A.C., Barbacena, P., Fan, J., Mathivet, T., Fonseca, C.G., Ragab, A., Yamaguchi, T.P.*, et al.* (2016). Non-canonical Wnt signalling modulates the endothelial shear stress flow sensor in vascular remodelling. Elife *5*, e07727.
Friedl, P., and Gilmour, D. (2009). Collective cell migration in morphogenesis, regeneration and cancer. Nat Rev Mol Cell Biol *10*, 445-457.
Friedl, P., and Mayor, R. (2017). Tuning Collective Cell Migration by Cell-Cell Junction Regulation. Cold Spring Harb Perspect Biol *9*.
Gray, R.S., Roszko, I., and Solnica-Krezel, L. (2011). Planar cell polarity: coordinating morphogenetic cell behaviors with embryonic polarity. Dev Cell *21*, 120-133.
Green, J., Nusse, R., and van Amerongen, R. (2014). The role of Ryk and Ror receptor tyrosine kinases in Wnt signal transduction. Cold Spring Harb Perspect Biol *6*.
Gumbiner, B.M. (2005). Regulation of cadherin-mediated adhesion in morphogenesis. Nat Rev Mol Cell Biol *6*, 622-634.
Han, M.K.L., van der Krogt, G.N.M., and de Rooij, J. (2017). Zygotic vinculin is not essential for embryonic development in zebrafish. PLoS One *12*, e0182278.
Heasman, S.J., and Ridley, A.J. (2008). Mammalian Rho GTPases: new insights into their functions from in vivo studies. Nat Rev Mol Cell Biol *9*, 690-701.
Hodgson, L., Shen, F., and Hahn, K. (2010). Biosensors for characterizing the dynamics of rho family GTPases in living cells. Curr Protoc Cell Biol *Chapter 14*, Unit 14 11 11-26.
Humphries, A.C., and Mlodzik, M. (2018). From instruction to output: Wnt/PCP signaling in development and cancer. Curr Opin Cell Biol *51*, 110-116.
Huveneers, S., Oldenburg, J., Spanjaard, E., van der Krogt, G., Grigoriev, I., Akhmanova, A., Rehmann, H., and de Rooij, J. (2012). Vinculin associates with endothelial VE-cadherin junctions to control force-dependent remodeling. J Cell Biol *196*, 641-652.
Jaalouk, D.E., and Lammerding, J. (2009). Mechanotransduction gone awry. Nat Rev Mol Cell Biol *10*, 63-73.
Korn, C., Scholz, B., Hu, J., Srivastava, K., Wojtarowicz, J., Arnsperger, T., Adams, R.H., Boutros, M., Augustin, H.G., and Augustin, I. (2014). Endothelial cell-derived non-canonical Wnt ligands control vascular pruning in angiogenesis. Development *141*, 1757-1766.
Kwon, H.B., Wang, S., Helker, C.S., Rasouli, S.J., Maischein, H.M., Offermanns, S., Herzog, W., and Stainier, D.Y. (2016). In vivo modulation of endothelial polarization by Apelin receptor signalling. Nat Commun *7*, 11805.
Lavina, B., Castro, M., Niaudet, C., Cruys, B., Alvarez-Aznar, A., Carmeliet, P., Bentley, K., Brakebusch, C., Betsholtz, C., and Gaengel, K. (2018). Defective endothelial cell migration in the absence of Cdc42 leads to capillary-venous malformations. Development *145*.
le Duc, Q., Shi, Q., Blonk, I., Sonnenberg, A., Wang, N., Leckband, D., and de Rooij, J. (2010). Vinculin potentiates E-cadherin mechanosensing and is recruited to actin-anchored sites within adherens junctions in a myosin II-dependent manner. J Cell Biol *189*, 1107-1115.
Lecuit, T., and Yap, A.S. (2015). E-cadherin junctions as active mechanical integrators in tissue dynamics. Nat Cell Biol *17*, 533-539.

Lee, J.G., and Heur, M. (2014). Interleukin-1beta-induced Wnt5a enhances human corneal endothelial cell migration through regulation of Cdc42 and RhoA. Mol Cell Biol *34*, 3535-3545.
Maddugoda, M.P., Crampton, M.S., Shewan, A.M., and Yap, A.S. (2007). Myosin VI and vinculin cooperate during the morphogenesis of cadherin cell cell contacts in mammalian epithelial cells. J Cell Biol *178*, 529-540.
Majumdar, A., Vainio, S., Kispert, A., McMahon, J., and McMahon, A.P. (2003). Wnt11 and Ret/Gdnf pathways cooperate in regulating ureteric branching during metanephric kidney development. Development *130*, 3175-3185.
Martin, K., Reimann, A., Fritz, R.D., Ryu, H., Jeon, N.L., and Pertz, O. (2016). Spatio-temporal co-ordination of RhoA, Rac1 and Cdc42 activation during prototypical edge protrusion and retraction dynamics. Sci Rep *6*, 21901.
Milde, F., Franco, D., Ferrari, A., Kurtcuoglu, V., Poulikakos, D., and Koumoutsakos, P. (2012). Cell Image Velocimetry (CIV): boosting the automated quantification of cell migration in wound healing assays. Integr Biol (Camb) *4*, 1437-1447.
Miller, P.W., Pokutta, S., Ghosh, A., Almo, S.C., Weis, W.I., Nelson, W.J., and Kwiatkowski, A.V. (2013). Danio rerio alphaE-catenin is a monomeric F-actin binding protein with distinct properties from Mus musculus alphaE-catenin. J Biol Chem *288*, 22324-22332.
Miyoshi, H., Ajima, R., Luo, C.T., Yamaguchi, T.P., and Stappenbeck, T.S. (2012). Wnt5a potentiates TGF-beta signaling to promote colonic crypt regeneration after tissue injury. Science *338*, 108-113.
Ng, M.R., Besser, A., Danuser, G., and Brugge, J.S. (2012). Substrate stiffness regulates cadherin-dependent collective migration through myosin-II contractility. J Cell Biol *199*, 545-563.
Petitjean, L., Reffay, M., Grasland-Mongrain, E., Poujade, M., Ladoux, B., Buguin, A., and Silberzan, P. (2010). Velocity fields in a collectively migrating epithelium. Biophys J *98*, 1790-1800.
Potente, M., Gerhardt, H., and Carmeliet, P. (2011). Basic and therapeutic aspects of angiogenesis. Cell *146*, 873-887.
Potente, M., and Makinen, T. (2017). Vascular heterogeneity and specialization in development and disease. Nat Rev Mol Cell Biol *18*, 477-494.
Ribeiro, A.S., Carvalho, F.A., Figueiredo, J., Carvalho, R., Mestre, T., Monteiro, J., Guedes, A.F., Fonseca, M., Sanches, J., Seruca, R.*, et al.* (2016). Atomic force microscopy and graph analysis to study the P-cadherin/SFK mechanotransduction signalling in breast cancer cells. Nanoscale *8*, 19390-19401.
Schambony, A., and Wedlich, D. (2007). Wnt-5A/Ror2 regulate expression of XPAPC through an alternative noncanonical signaling pathway. Dev Cell *12*, 779-792.
Schlessinger, K., McManus, E.J., and Hall, A. (2007). Cdc42 and noncanonical Wnt signal transduction pathways cooperate to promote cell polarity. J Cell Biol *178*, 355-361.
Seddiki, R., Narayana, G., Strale, P.O., Balcioglu, H.E., Peyret, G., Yao, M., Le, A.P., Teck Lim, C., Yan, J., Ladoux, B.*, et al.* (2018). Force-dependent binding of vinculin to alpha-catenin regulates cell-cell contact stability and collective cell behavior. Mol Biol Cell *29*, 380-388.
Stricker, S., Rauschenberger, V., and Schambony, A. (2017). ROR-Family Receptor Tyrosine Kinases. Curr Top Dev Biol *123*, 105-142.

Tambe, D.T., Hardin, C.C., Angelini, T.E., Rajendran, K., Park, C.Y., Serra-Picamal, X., Zhou, E.H., Zaman, M.H., Butler, J.P., Weitz, D.A*., et al.* (2011). Collective cell guidance by cooperative intercellular forces. Nat Mater *10*, 469-475.
Vitorino, P., and Meyer, T. (2008). Modular control of endothelial sheet migration. Genes Dev *22*, 3268-3281.
Wakayama, Y., Fukuhara, S., Ando, K., Matsuda, M., and Mochizuki, N. (2015). Cdc42 mediates Bmp-induced sprouting angiogenesis through Fmnl3-driven assembly of endothelial filopodia in zebrafish. Dev Cell *32*, 109-122.
Wu, X., Li, S., Chrostek-Grashoff, A., Czuchra, A., Meyer, H., Yurchenco, P.D., and Brakebusch, C. (2007). Cdc42 is crucial for the establishment of epithelial polarity during early mammalian development. Dev Dyn *236*, 2767-2778.
Xu, W., Baribault, H., and Adamson, E.D. (1998). Vinculin knockout results in heart and brain defects during embryonic development. Development *125*, 327-337.
Yang, Y., and Mlodzik, M. (2015). Wnt-Frizzled/planar cell polarity signaling: cellular orientation by facing the wind (Wnt). Annu Rev Cell Dev Biol *31*, 623-646.
Yao, M., Qiu, W., Liu, R., Efremov, A.K., Cong, P., Seddiki, R., Payre, M., Lim, C.T., Ladoux, B., Mege, R.M*., et al.* (2014). Force-dependent conformational switch of alpha-catenin controls vinculin binding. Nat Commun *5*, 4525.
Yap, A.S., Duszyc, K., and Viasnoff, V. (2017). Mechanosensing and Mechanotransduction at Cell-Cell Junctions. Cold Spring Harb Perspect Biol.
Yonemura, S., Wada, Y., Watanabe, T., Nagafuchi, A., and Shibata, M. (2010). alpha-Catenin as a tension transducer that induces adherens junction development. Nat Cell Biol *12*, 533-542.
Zemljic-Harpf, A.E., Miller, J.C., Henderson, S.A., Wright, A.T., Manso, A.M., Elsherif, L., Dalton, N.D., Thor, A.K., Perkins, G.A., McCulloch, A.D*., et al.* (2007). Cardiac-myocyte-specific excision of the vinculin gene disrupts cellular junctions, causing sudden death or dilated cardiomyopathy. Mol Cell Biol *27*, 7522-7537.

Table 1: List of siRNAs.

Control siRNA	Dharmacon	D-001810-01-05	UGGUUUACAUGUCGACUAA
siCTNNA1	Dharmacon	J-010505-06	GAUGGUAUCUUGAAGUUGA
siCDC42	Dharmacon	J-005057-07	GAUGACCCCUCUACUAUUG
siCDH5	Dharmacon	J-003641-07	GAGCCCAGGUCAUUAUCAA
siFZD4	Dharmacon	J-005503-06	GAUCGAUUCUUCUAGGUUU
siFZD6	Dharmacon	J-005505-07	GAAGGAAGGAUUAGUCCAA
siFZD7	Dharmacon	J-003671-11	UGAUGUACUUUAAGGAGGA
siFZD8	Dharmacon	J-003962-08	UCACCGUGCCGCUGUGUAA
siROR1	Dharmacon	J-003171-09	UGACUUGUGUCGCGAUGAA
siROR2	Dharmacon	D-003172-06	GCAGGUGCCUCCUCAGAUG
siRYK	Dharmacon	J-003174-11	GGUUUGUUGUGCAGUAAUA
siVCL	Dharmacon	J-009288-05	UGAGAUAAUUCGUGUGUGUUA
siWNT11	Dharmacon	L-009474-00-0005	SMARTpool
siWNT5a	Dharmacon	L-003939-00-0005	SMARTpool

Table 2: List of qPCR primers

CDC42	TGACAGATTACGACCGCTGAGTT	GGAGTCTTTGGACAGTGGTGAG
CDH5	TCTCCGCAATAGACAAGGACA	TGGTATGCTCCCGGTCAAAC
CTNNA1	GGACCTGCTTTCGGAGTACATG	CTGAAACGTGGTCCATGACAGC
FZD4	TTCACACCGCTCATCCAGTACG	ACGGGTTCACAGCGTCTCTTGA
FZD6	GGCAGTGTATCTGAAAGTGCGC	GATGTGGAACCTTTGAGGCTGC
FZD7	GTCTTCAGCGTGCTCTACACAG	ACGGCATAGCTCTTGCACGTCT
FZD8	GCTCTACAACCGCGTCAAGACA	AAGGTGGACACGAAGCAGAGCA
GAPDH	GTCAAGGCTGAGAACGGGAA	TGGACTCCACGACGTACTCA
ROR1	GAGGCAACCAAAACACGTCAGAG	GGCACACTCACCCAATTCTTCC
ROR2	ACGTACCCTCGTGTAGTCC	CGATGACCAGTGGAATTGCG
RYK	CAGCAAGACCTGGTACACATGG	CAAGTCTCTGGAGAGGGCATTG
VCL	TGAGCAAGCACAGCGGTGGATT	TCGGTCACACTTGGCGAGAAGA
WNT5A	TACGAGAGTGCTCGCATCCTCA	TGTCTTCAGGCTACATGAGCCG
WNT11	CAGTGTTGCGTCTGGTTCAGT	TGCTATGGCATCAAGTGGCT

Carvalho et al. Figure 1

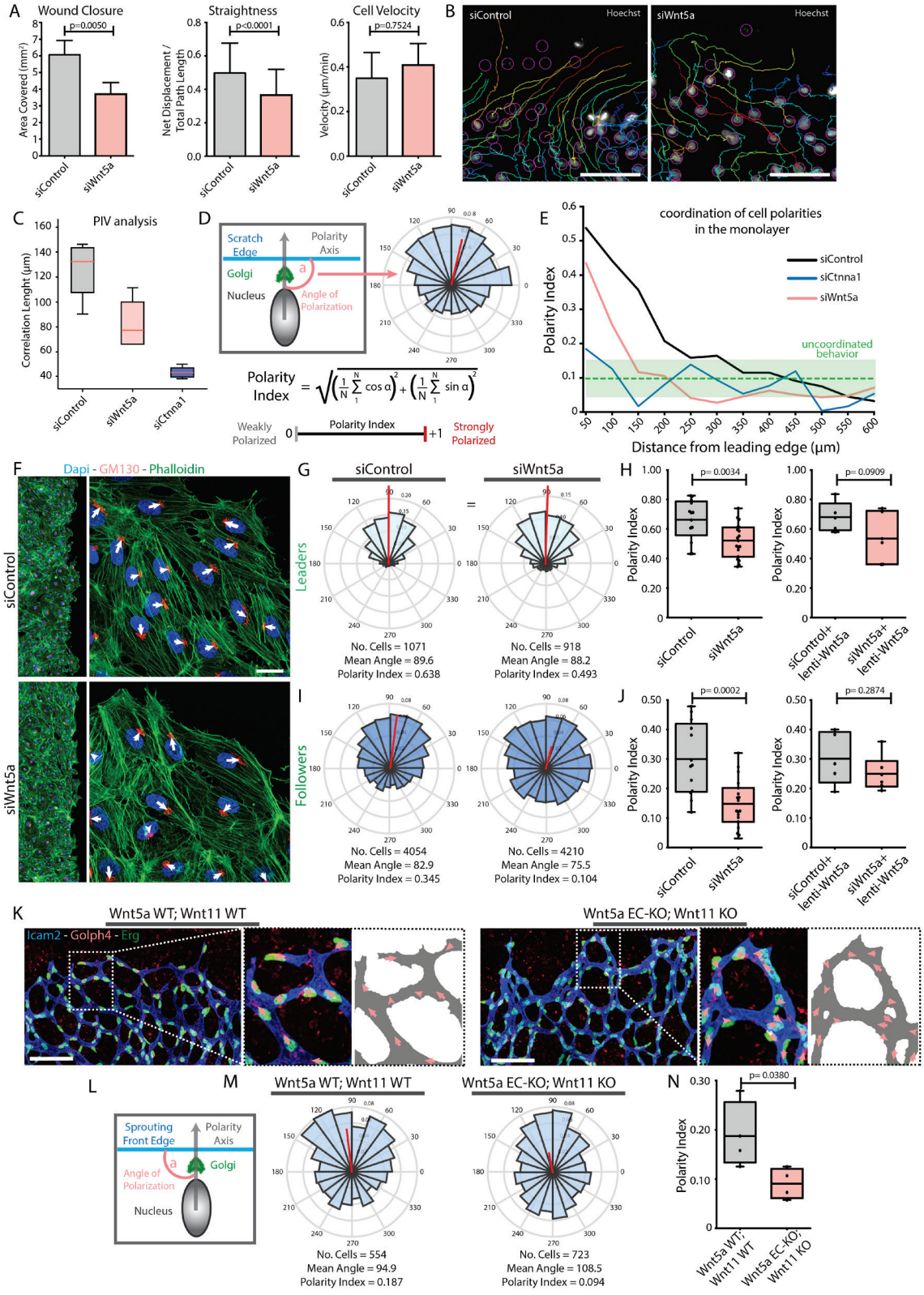

Carvalho et al. Figure 2

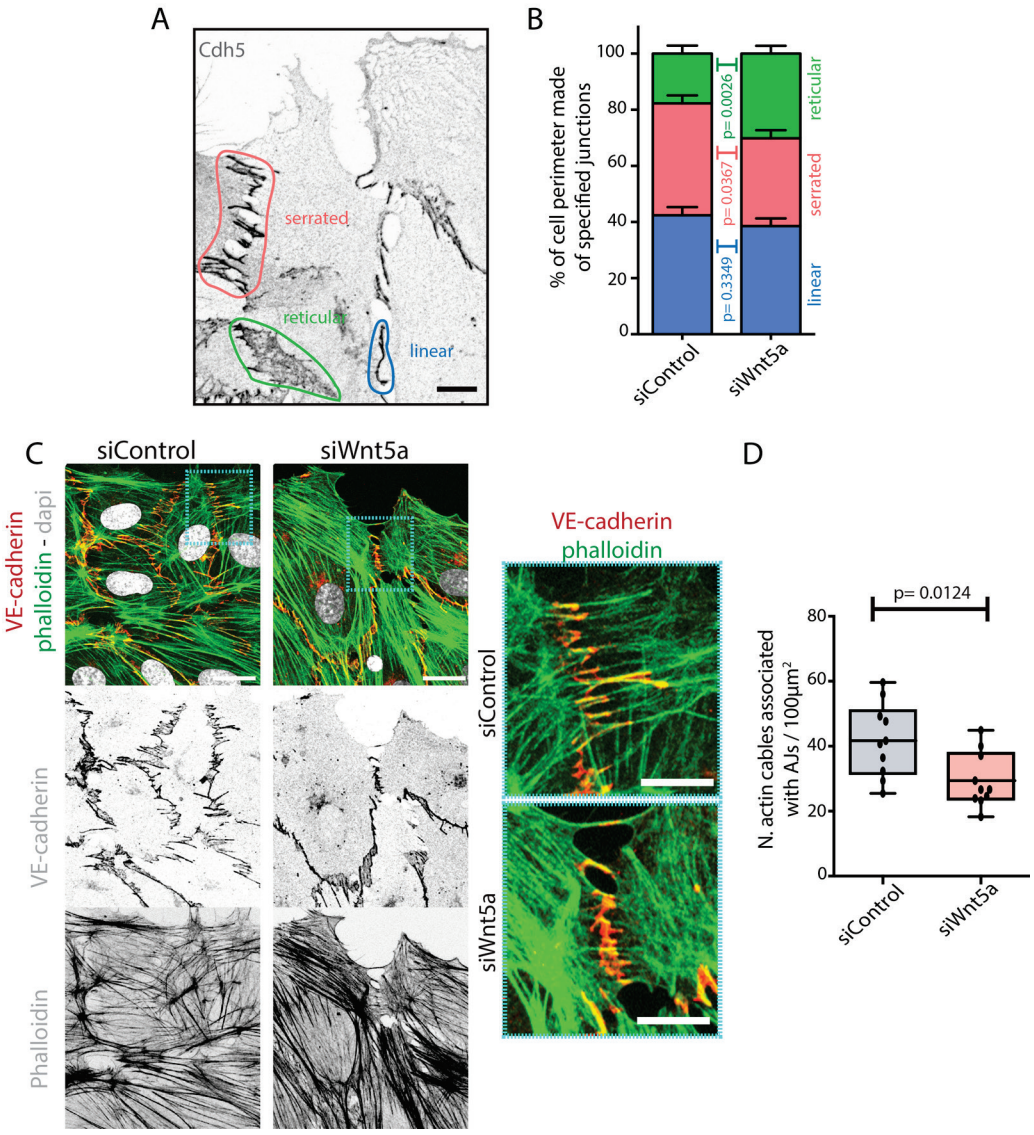

Carvalho et al. Figure 3

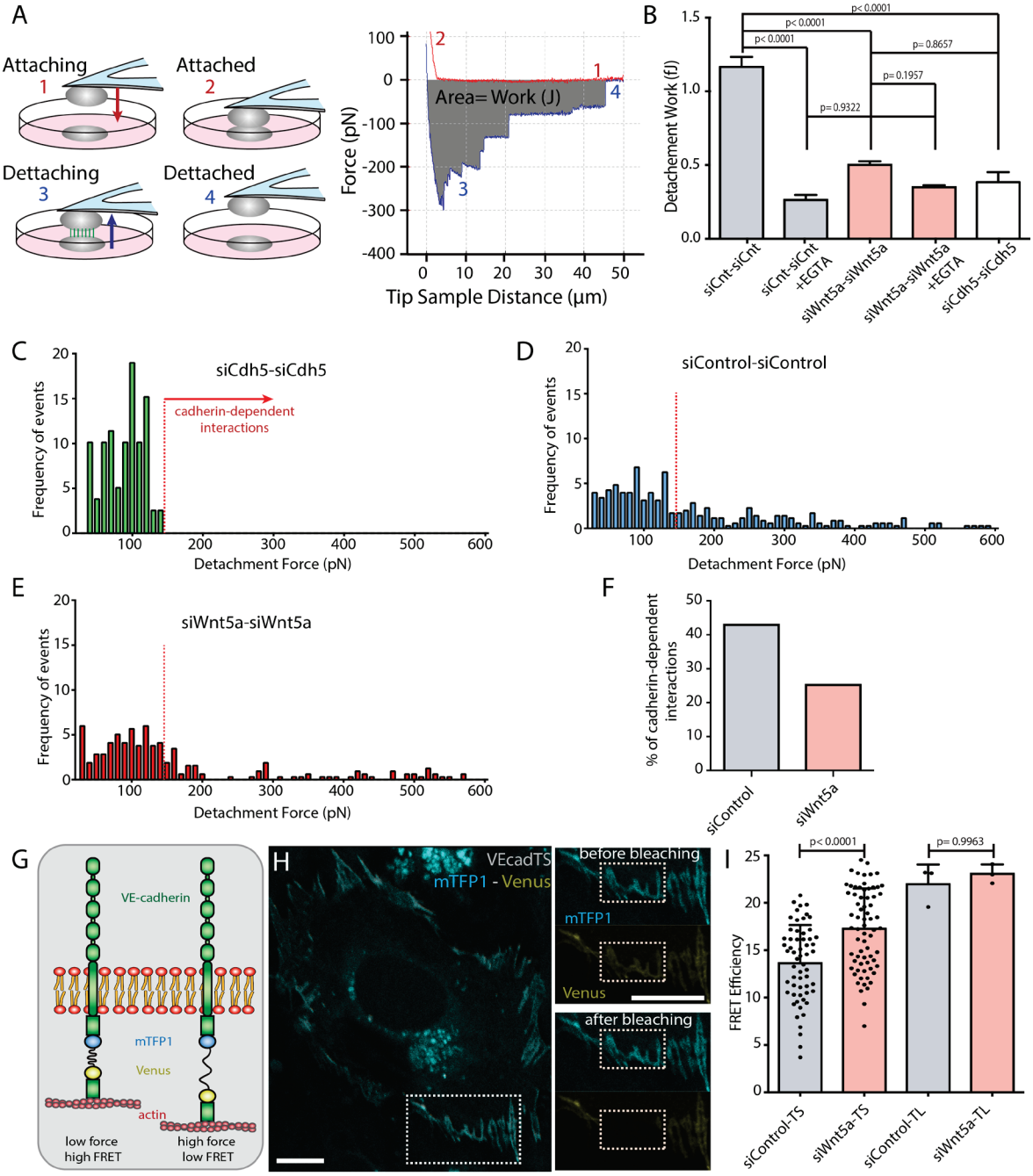

Carvalho et al. Figure 4

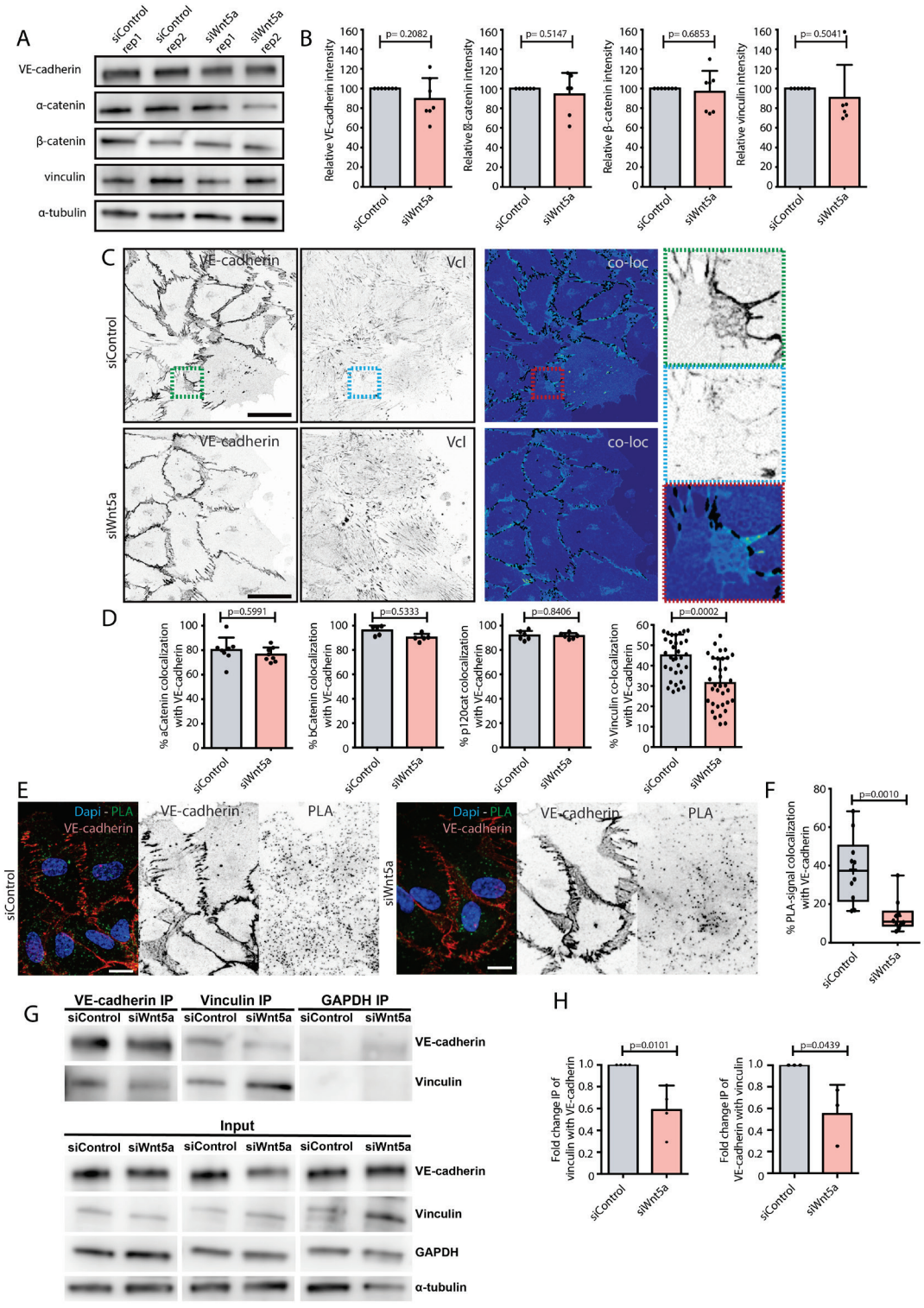

Carvalho et al. Figure 5

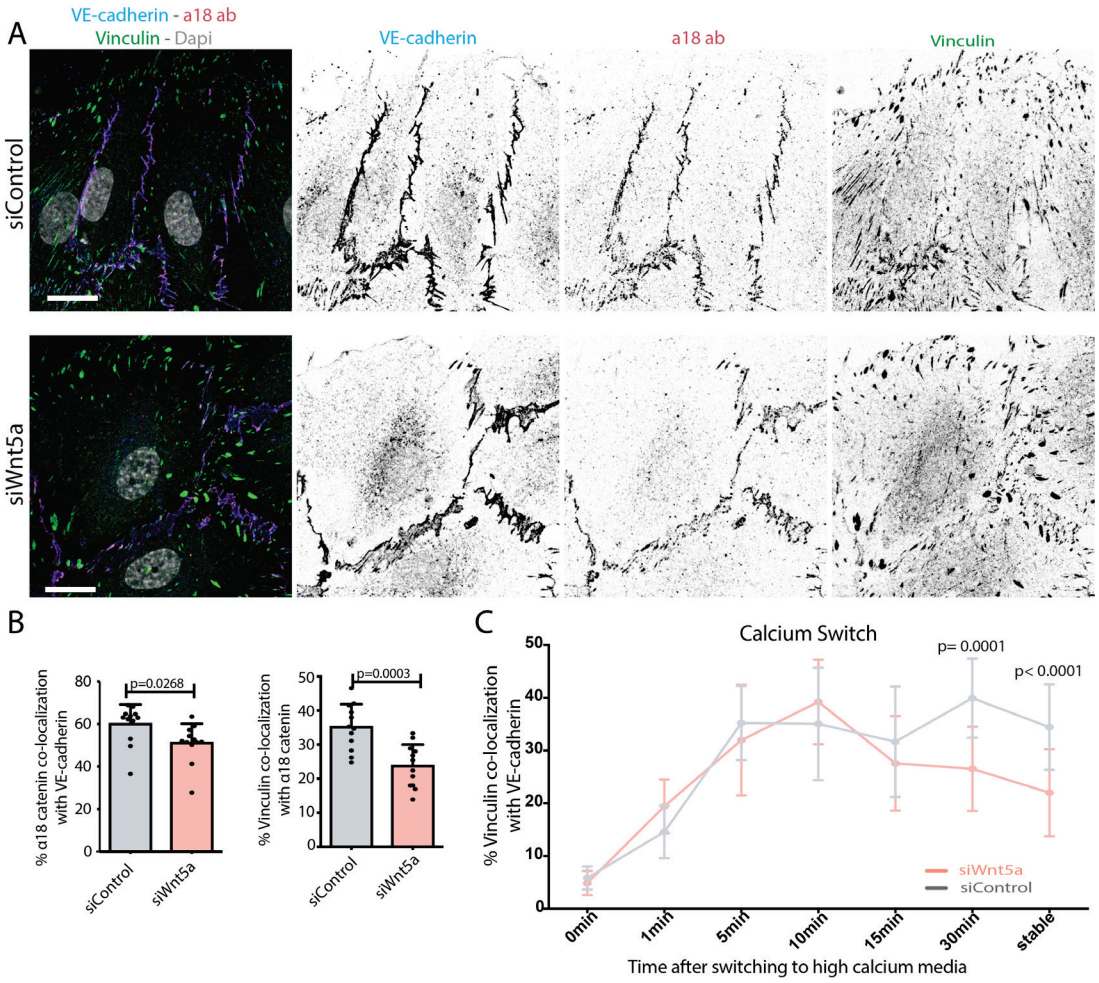

Carvalho et al. Figure 6

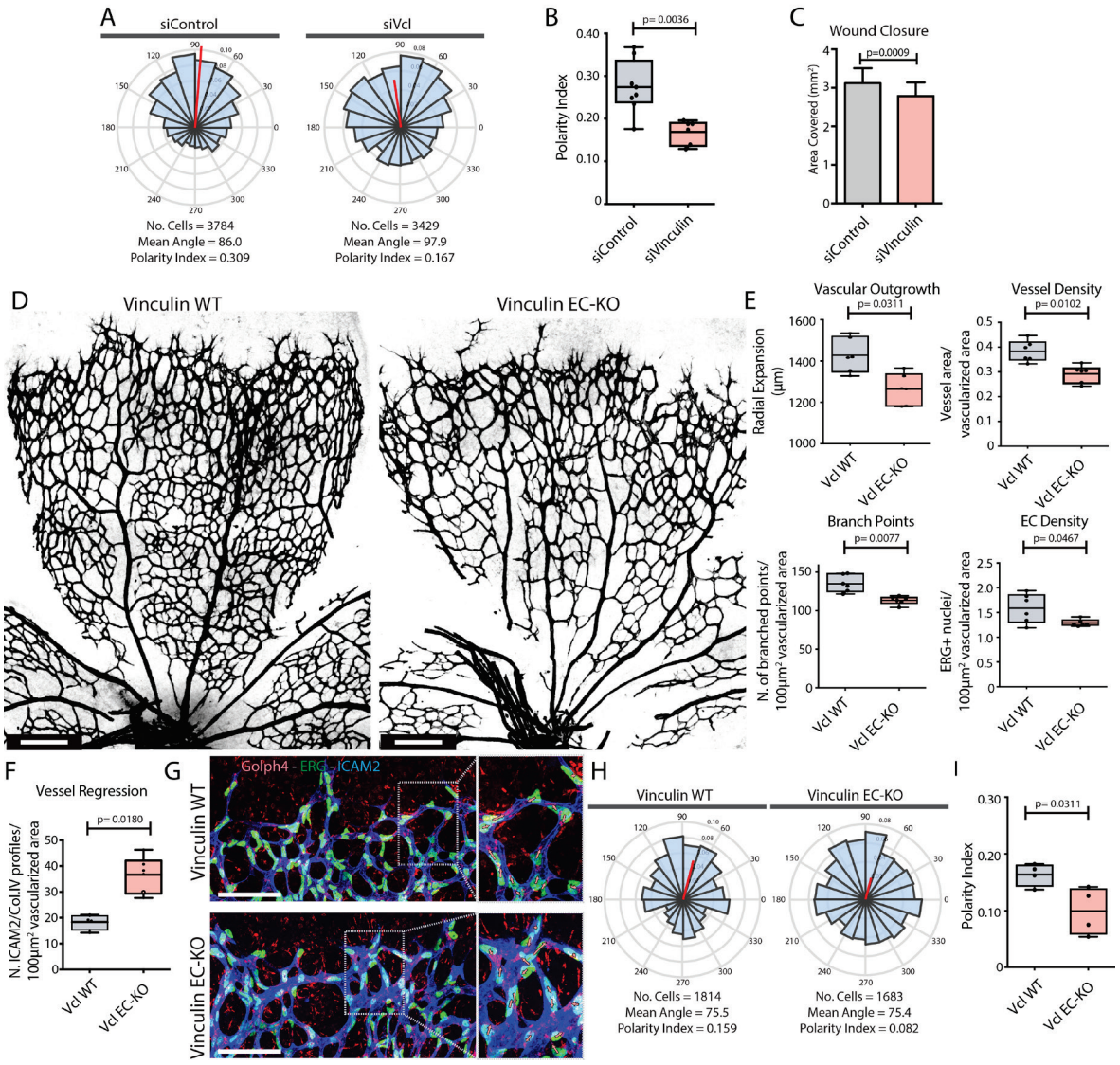

Carvalho et al. Figure 7

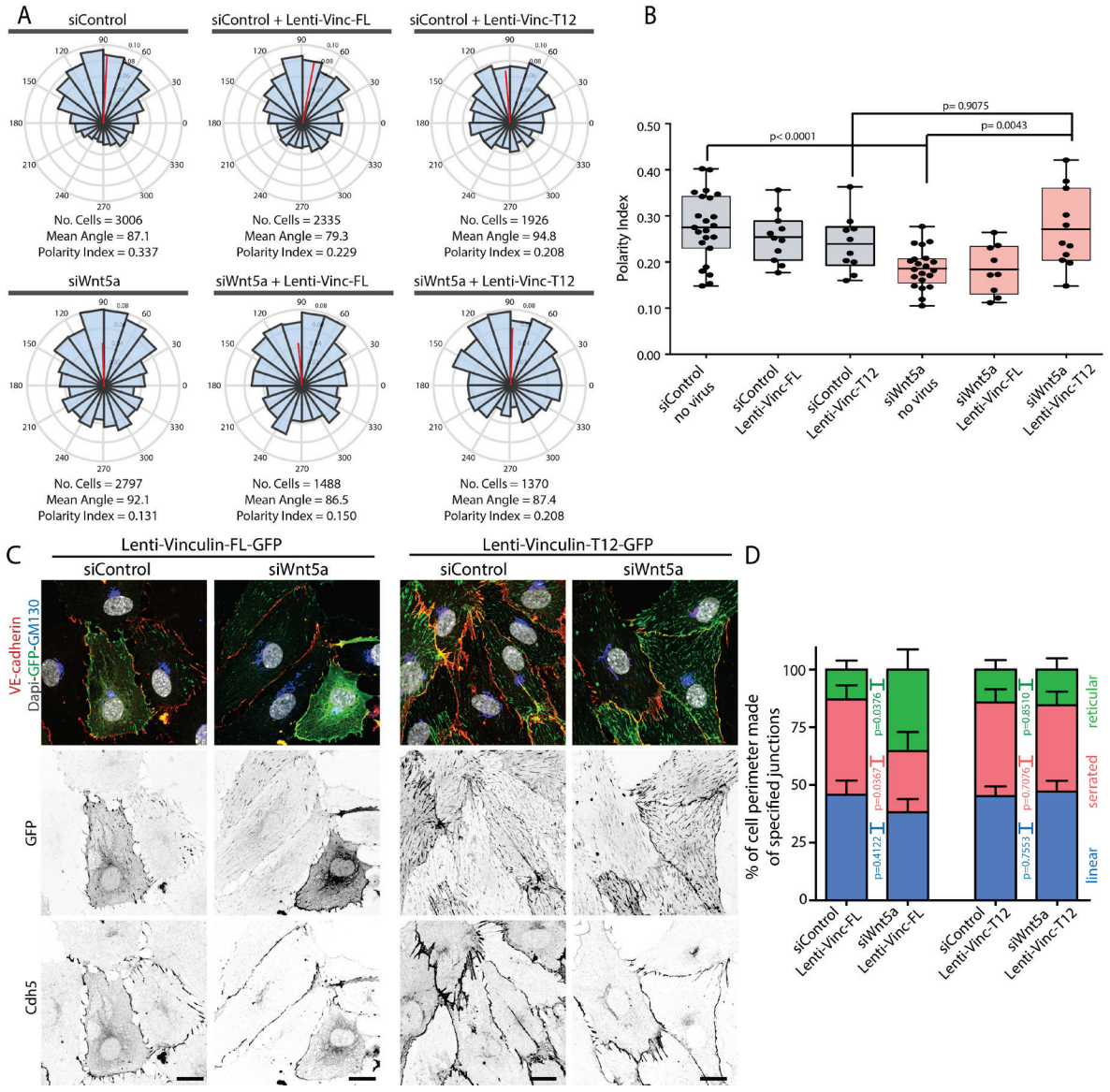

Carvalho et al. Figure 8

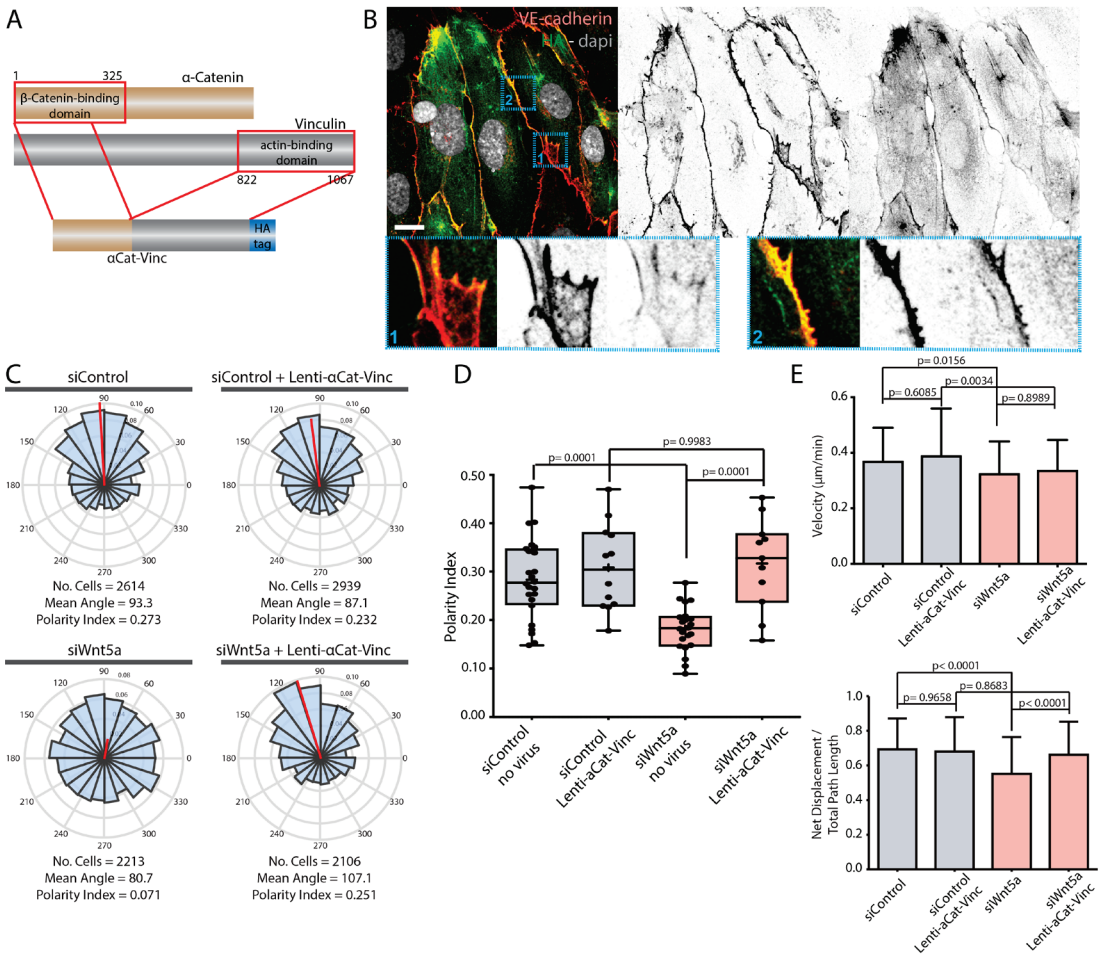

Carvalho et al. Figure 9

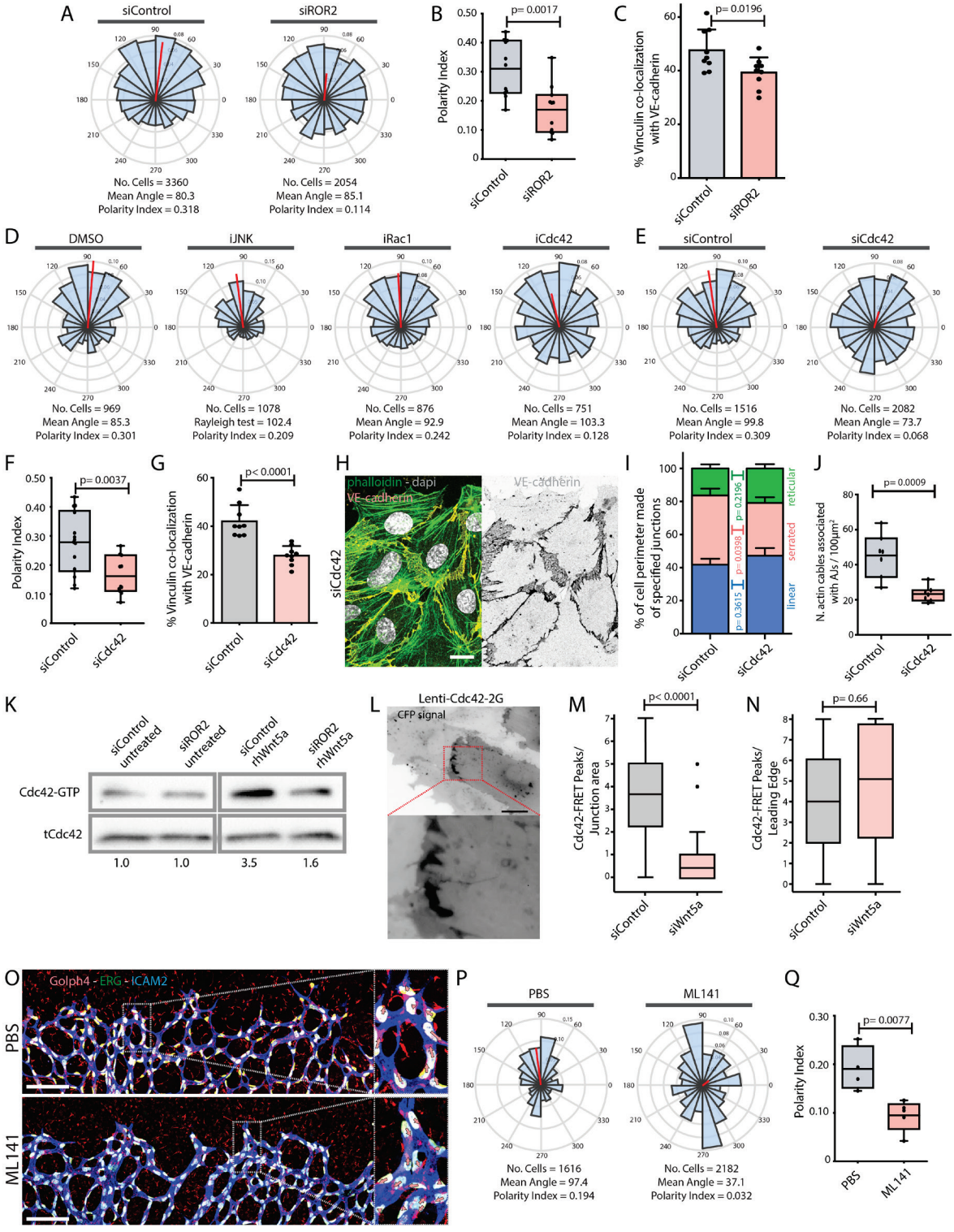

Carvalho et al. Figure 10

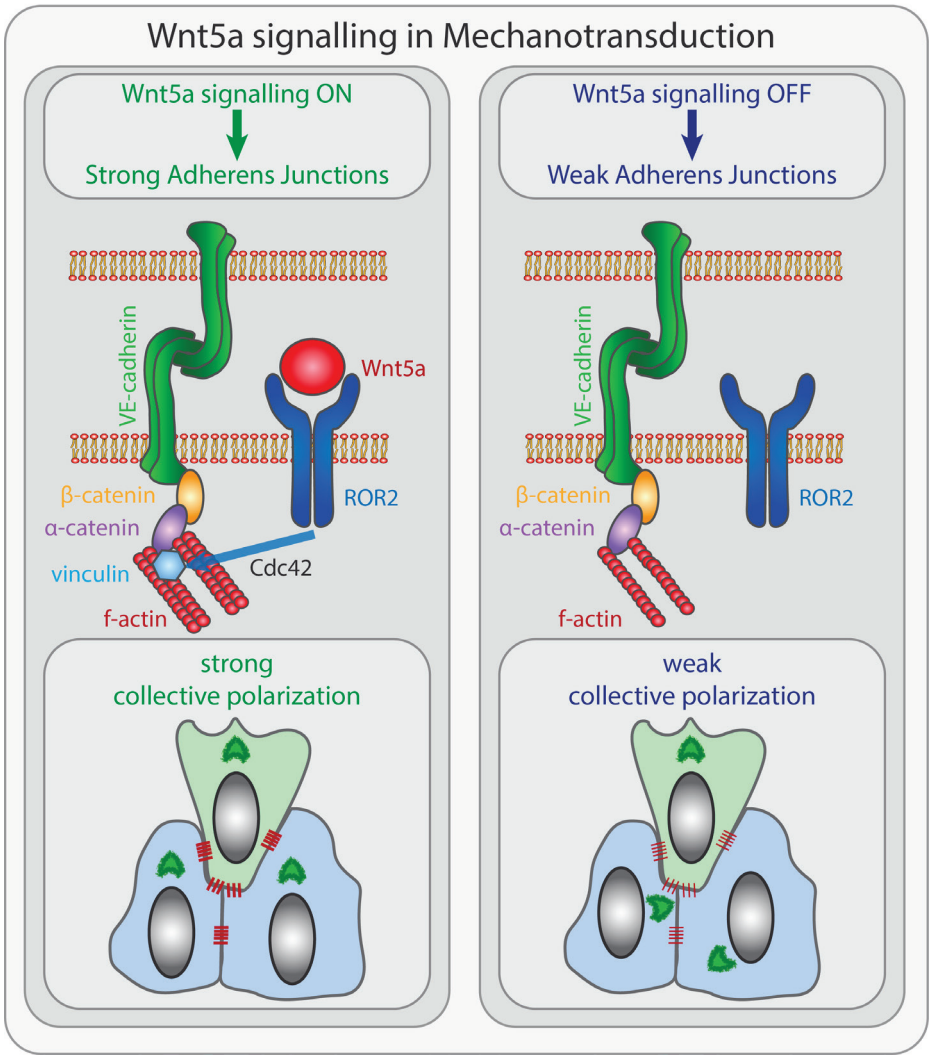

Carvalho et al. Figure 11

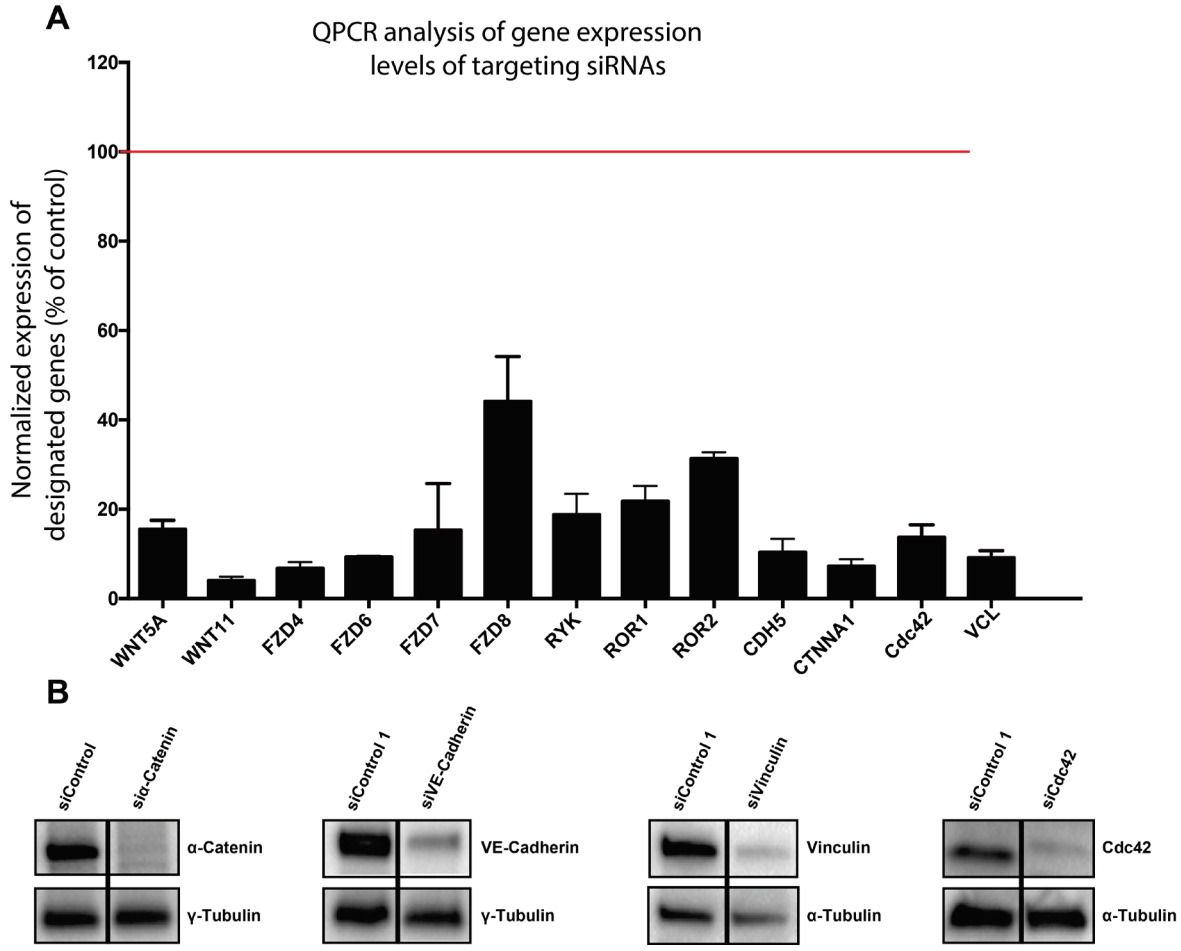

Carvalho et al. Figure 1 - Figure Supplement 1

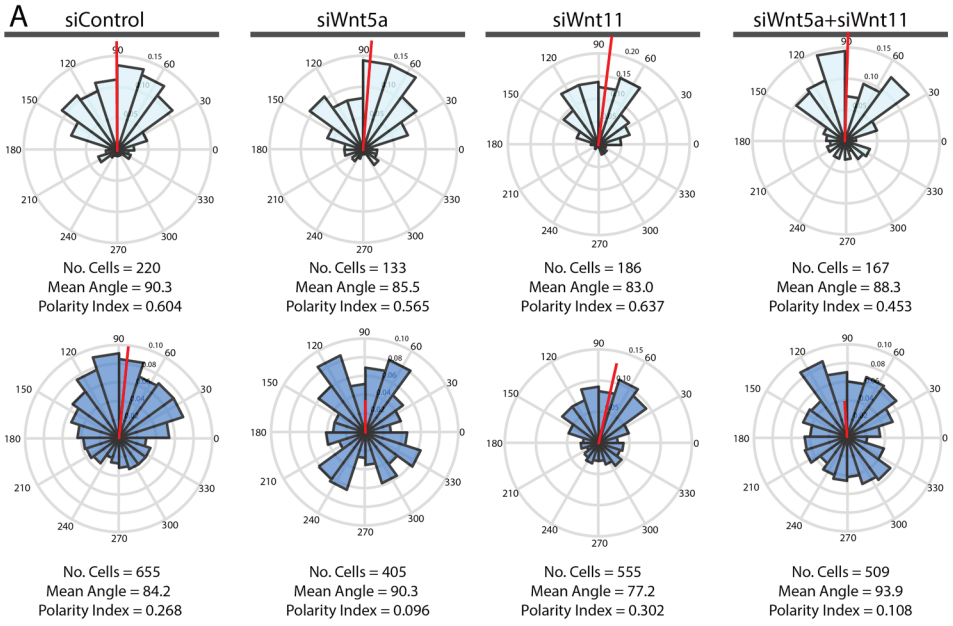

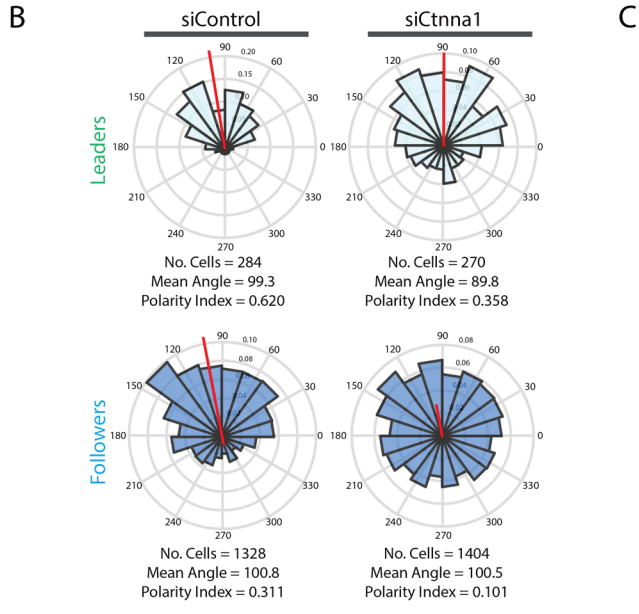

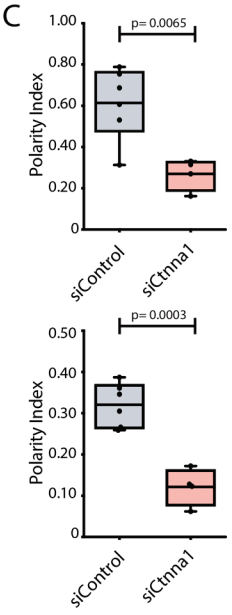

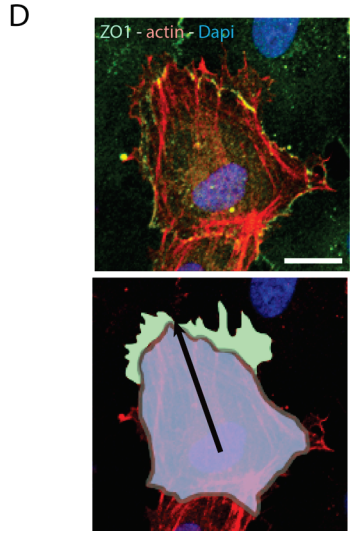

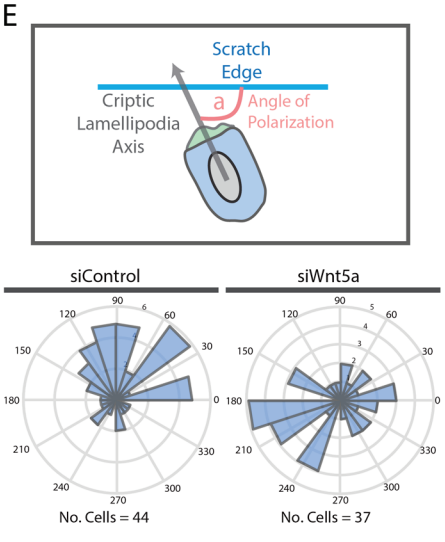

Carvalho et al. Figure 7 - Figure Supplement 1

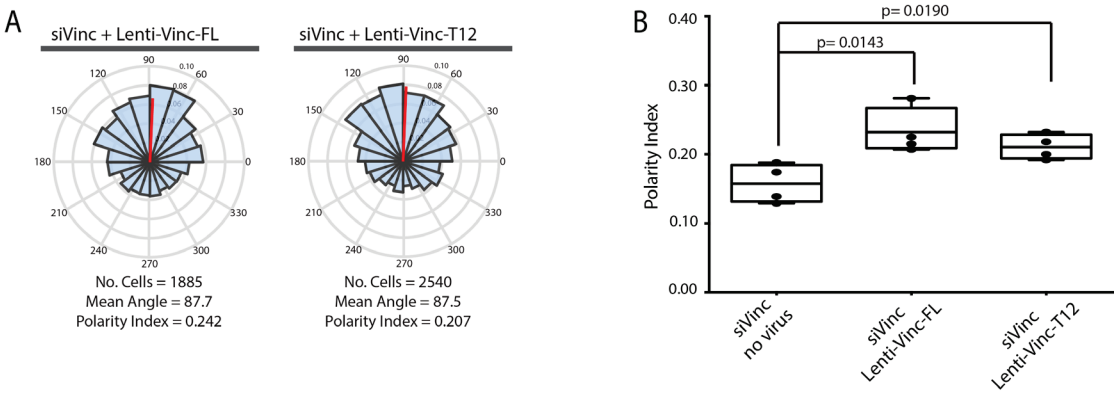

Carvalho et al. Figure 7 - Figure Supplement 2

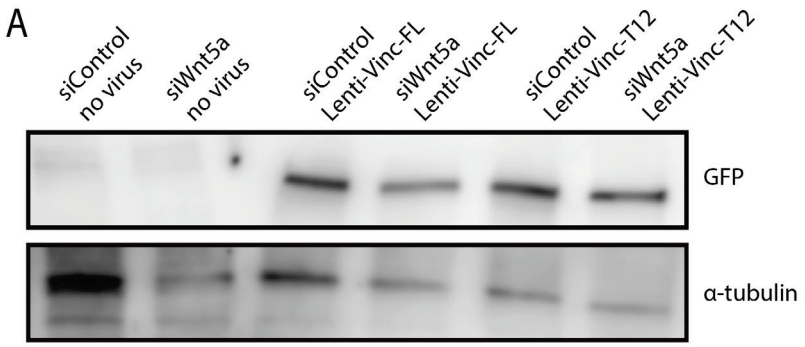

Carvalho et al. Figure 8 - Figure Supplement 1

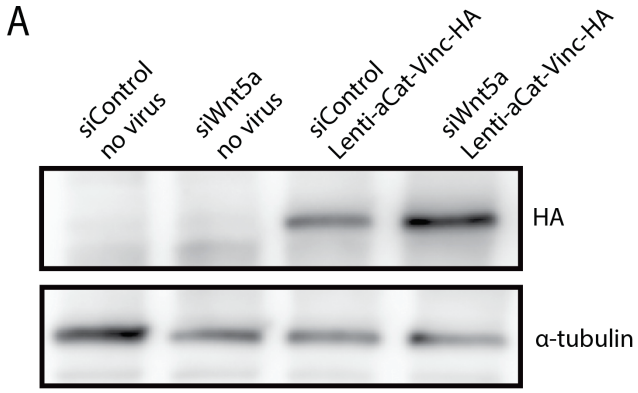

Carvalho et al. Figure 9 - Figure Supplement 1

A